

RICE UNIVERSITY

**SWNT and Graphene Colloidal Dispersions:  
Phase behavior, Material Fabrication and  
Characterization**

by

**Budhadipta Dan**

A THESIS SUBMITTED  
IN PARTIAL FULFILLMENT OF THE  
REQUIREMENTS FOR THE DEGREE

**Doctor of Philosophy**

APPROVED, THESIS COMMITTEE:



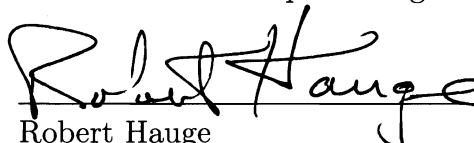
---

Matteo Pasquali, Chair  
Professor in Chemical and Biomolecular  
Engineering and Chemistry



---

Junichiro Kono  
Professor of Physics and Astronomy, and  
Electrical and Computer Engineering



---

Robert Hauge  
Distinguished Faculty Fellow, Dept. of  
Chemistry

Houston, Texas

April, 2011

## Abstract

This dissertation explores the microstructural properties, flow, and phase behavior of aqueous suspensions of single-walled carbon nanotube (SWNT) and graphene. Liquid phase processing with scalable and industrially viable methods is used for fabrication of basic engineering materials like thin films, coatings and 1-D fibrillar structures. The electro-optical transport properties of these novel materials are characterized.

A recipe for formulation of an aqueous colloidal suspension with high SWNT concentration is presented. A combination of two surfactants provides optimal rheological behavior for “rod coating” uniform transparent conductive SWNT thin films, with minimal dewetting, rupture and defects. “Doping” with acids and metallic nanoparticles yield SWNT films with electrical sheet resistance of 100 and 300  $\Omega/sq$  for respective optical transparency of 70% and 90%.

SWNT thin films with local nematic ordering and alignment are fabricated using a “slow vacuum filtration” process. The technique is successfully demonstrated on several aqueous SWNT suspensions, employing different ionic and non-ionic surfactants, as well as on dispersions enriched in metallic SWNTs, produced by density gradient ultracentrifugation. Scanning electron microscopy and image analysis revealed a local nematic order parameter of  $S \sim 0.7-0.8$  for the SWNT films. Aligned SWNT films and fibers are employed as templates, in a simple drop drying process, for large scale ordered ( $S \sim 0.7-0.9$ ) assembly of plasmonic nanoparticles, like gold nanorods, micro-triangles and platelets.

Colloidal self-assembly of surfactant stabilized SWNTs and AC dielectrophoresis (DEP) are combined in a novel two-step technique for fabrication of 1-D SWNT fibrils. The self-assembled SWNT-surfactant colloidal structures are  $10^3 - 10^4$  fold more responsive to external AC electrical fields. The DEP SWNT fibrils show significant Raman alignment ratio ( $\sim 3-5$ ) and good electrical conductivity.

A detailed study on the phase behavior of giant graphene oxide flakes (aspect ratio  $> 10^4$ ) suspended in water is presented. The lyotropic suspensions transition from an isotropic to a biphasic system and to a discotic nematic liquid crystal with increasing flake concentration. Polarizing optical microscopy and colloidal particle inclusions reveal the alignment and orientation flakes in the nematic phase, the nematic order parameter ( $S \sim 0.43$ ), low optical birefringence ( $\Delta n = -0.0018$ ), and an average Frank elastic constant ( $K \sim 100$  pN) which is about 100 fold higher than previously studied discotic liquid crystals.

## Acknowledgments

First of all, I thank my advisor Matteo Pasquali for taking me under his supervision and allowing me to work in his laboratory. I especially thank him for his constant guidance, support, encouragement, advices and constructive criticism, over the years. His demand for excellence has helped me become a better researcher and improve significantly in numerous aspects, including, scientific writing and research aptitude.

I thank Prof. Ivan Smalyukh (University of Colorado at Boulder) for inviting me and allowing me to work in his research laboratory for a period of six months; it was a period of tremendous learning experience. In addition to learning about liquid crystals, I also tried to assimilate his qualities of scientific vision and tireless hardwork.

I thank Prof. Junichiro Kono, Dr. Robert Hauge, and Prof. Douglas Natelson, for agreeing to be on my MS and PhD Thesis defense committees, their feedback, and their help and advice on various research projects. I also thank R.E. Smalley Institute for Nanoscale Science and Technology, Prof. Kono, Prof. Tour and Prof. Ajayan for allowing me to use the equipments in their laboratories. I thank Dr. Howard Schmidt, Prof. Clarence Miller, Prof. George Hirasaki, Glen Irvin, Aurélie Mayeux, Ken Smith and T.J. Wainerdi for their participation and helpful discussions in various projects.

I thank all members of the Pasquali group; they contributed significantly to my growth and development as a researcher and made these six years a fun-filled and fruitful experience; Oscar Coronado, Nicholas Parra-Vasquez, Nikta Fakhri, Natnael Behabtu, Dmitri Tsentelovich, Colin Young, Francesca Mirri, Chloe Liu, Micah Green, Mainak Majumder, Anson Ma, Jaewook Nam, Alex Lee, Shannon Eichmann, Guido Pagani, Marco Banzola, Mariella Mariotti, Marco Notarianni, Flavia Vitale, and Federico Matteini.

I thank all members of the Smalyukh group; my six months at University of Colorado at Boulder were fun, memorable, and productive largely due to them; Clayton Lapointe, Taewoo Lee, Bohdan Senyuk, Rahul Trivedi, Julian Evans, Dennis Gardner, Zhiyuan Qi, Angel Martinez, Núria Petit-Garrido, Chris Twombly, Heather Loden, Tyler Wingfield, Paul Ackerman and Sabrina Thompson.

I thank all the support staff in the Applied Physics program, Physics & Astronomy department, Chemical and Biomolecular Engineering department and R.E. Smalley Institute for Nanoscale Science and Technology for their invaluable help when dealing with administrative matters.

I thank my entire extended family in India for their love, support, and belief in me. I thank my sister Meenakshi Dan Hardi and her family, and Anni Siitonen for being with me during good times and helping me get through tough times.

I dedicate this Thesis to my parents, Dr. Tapan Kumar Dan and Smt. Namita Dan, for their unquestioned love, support, and understanding, and always expecting the best from me.

# Contents

Abstract	iii
Acknowledgments	v
List of Illustrations	xi
List of Tables	xvi
<b>1 Introduction</b>	<b>1</b>
1.1 SWNT Synthesis . . . . .	3
1.2 SWNT Optical Properties . . . . .	3
1.3 SWNT Electrical Properties . . . . .	5
1.4 Current SWNT Research . . . . .	7
1.5 Thesis Outline . . . . .	8
<b>2 Transparent Conductive SWNT Films</b>	<b>11</b>
2.1 Introduction . . . . .	11
2.2 Fabrication Method: Rod Coating . . . . .	12
2.3 Figure of Merit . . . . .	17
2.4 Coating Ink Formulation . . . . .	20
2.5 Film Performance Characterization . . . . .	29
2.6 SWNT Film Post-processing . . . . .	30
2.6.1 Doping with Gold ions . . . . .	34
2.6.2 Treatment with Strong Acids . . . . .	35
2.7 Doped SWNT Film Performance Durability . . . . .	38

2.8	Results . . . . .	40
2.9	Conclusions . . . . .	43
2.10	Appendix . . . . .	45
2.10.1	High Concentration SWNT Dispersions . . . . .	45
2.10.2	Preparation of SWNT Coating Fluid . . . . .	47
2.10.3	Rod Coating Procedure . . . . .	48
2.10.4	Acid Treatment Procedure . . . . .	49

### **3 Nematic-like Alignment in SWNT Thin Films from Aqueous Colloidal Suspensions** **52**

3.1	Introduction . . . . .	52
3.2	Slow Filtration Technique . . . . .	55
3.2.1	Exploring the Role of Surfactants . . . . .	55
3.3	Analysis of Alignment in SWNT Films . . . . .	59
3.4	Electro-optical Characterization . . . . .	62
3.5	SWNT Nematic Ordering Mechanism . . . . .	62
3.6	Conclusions . . . . .	65
3.7	Appendix . . . . .	65
3.7.1	Density Gradient Ultracentrifugation . . . . .	65
3.7.2	Preparation of SWNT Dispersions . . . . .	66
3.7.3	Slow Vacuum Filtration . . . . .	70
3.7.4	Analysis of SWNT Alignment in Nematic Films . . . . .	71

### **4 Aligned SWNT Ribbons and Flakes from Superacid Solutions** **73**

4.1	Introduction . . . . .	73
-----	------------------------	----

4.1.1	SWNT-Superacid Phase Behavior . . . . .	74
4.1.2	Novel Fabrication Method for 2-D Aligned SWNT Macrostructures . . . . .	77
4.2	Experimental Methods . . . . .	78
4.2.1	SWNT-Superacid Solution Preparation . . . . .	78
4.2.2	SWNT Macrostructure Fabrication Procedure . . . . .	78
4.3	Results & Discussion . . . . .	80
4.3.1	Optical Microscopy . . . . .	80
4.3.2	Raman Spectroscopy . . . . .	81
4.4	Conclusions . . . . .	81
4.5	Appendix . . . . .	86
4.5.1	Fabrication of Aligned Macrostructures from Metallic-type Enriched SWNTs . . . . .	86

## **5 Spontaneous Templating of Anisotropic Gold Nanoparticles on Ordered SWNT Macrostructures** **88**

5.1	Introduction . . . . .	88
5.2	Materials and Methods . . . . .	91
5.2.1	Fabrication of Gold Nanorods and Microparticles . . . . .	91
5.2.2	Fabrication of Aligned SWNT Macrostructures . . . . .	92
5.2.3	Gold Nanorod Deposition Procedure . . . . .	93
5.3	Results . . . . .	93
5.3.1	Orientation Distribution Function for Gold Nanorods . . . . .	96
5.3.2	Scalar Order Parameter for Gold Nanorod Arrays . . . . .	98
5.4	Discussion . . . . .	99
5.5	Conclusions . . . . .	104



<b>6 Self-assembly and Dielectrophoresis: 1-D Fibrils from Aqueous SWNT Suspensions</b>	<b>105</b>
6.1 Introduction . . . . .	105
6.2 Experimental Methods . . . . .	109
6.2.1 Colloidal Self-Assembly: Mini-Fibrils . . . . .	109
6.2.2 AC Dielectrophoresis . . . . .	112
6.3 Results and Discussions . . . . .	112
6.3.1 Mini-Fibrils . . . . .	112
6.3.2 DEP SWNT Fibrils . . . . .	117
6.3.3 Theoretical Analysis . . . . .	122
6.4 Conclusions . . . . .	128
6.5 Appendix . . . . .	129
6.5.1 Rotational Motion of Colloidal Particles under DEP . . . . .	129
6.5.2 Changes in Length Distribution of Mini-Fibrils in Suspension Over Time . . . . .	131
6.5.3 Dielectric Permittivity of Sodium Deoxycholate . . . . .	131
6.5.4 Thermo-gravimetric Analysis of Pure DOC . . . . .	132
<b>7 Liquid Crystalline Gel of Aqueous, Giant Graphene Oxide Flakes</b>	<b>135</b>
7.1 Introduction . . . . .	135
7.2 Phase Behavior of Giant Graphene Oxide Aqueous Suspensions . . . . .	138
7.3 Optical Birefringence and Order Parameter . . . . .	144
7.4 Anisotropic Particle Inclusions and LC Defects . . . . .	146
7.5 Colloidal Inclusions and Elastic Distortions . . . . .	150
7.6 Conclusions . . . . .	156

## Illustrations

1.1	Molecular structure of a single-walled carbon nanotube. . . . .	2
1.2	Electronic density of states for SWNTs and various spectroscopic characterization tools. . . . .	6
2.1	Mayer wire-wound rod coating apparatus and SWNT thin film coating process. . . . .	14
2.2	Viscosity vs. shear rate, and optical micrographs for SWNT-SDBS dispersion and SWNT-SDBS-Triton X100 dispersion, showing up to 3 orders of magnitude increase in low-shear viscosity upon addition of Triton X-100. . . . .	26
2.3	SEM and AFM image of a rod coated SWNT thin film fabricated from SWNT-SDBS-TritonX100 dispersion. . . . .	29
2.4	Surfactant removal from SWNT films as a function of amount of time in water-ethanol bath, and its effect on film electrical properties. . . .	31
2.5	Schematic representation of energy levels and Schottky barrier at the junction between metallic and semiconducting SWNTs in a SWNT network. . . . .	33
2.6	Effect of Au doping on the electrical sheet resistance of SWNT thin films. . . . .	36

2.7	Optical transmission spectra and sheet resistance vs. transmittance curves for a series of rod coated SWNT films, before and after oleum treatment. . . . .	39
2.8	Effect of acid treatment and durability tests (in 80°C hot water and 400°C N <sub>2</sub> environment) on the electrical properties of SWNT films . .	41
2.9	Comparison of the electro-optical performance of our acid treated rod coated SWNT films with other transparent conductive SWNT thin films published in the literature. . . . .	42
2.10	FOM plots of our acid treated rod coated SWNT films and other TC SWNT films published in literature shown in two different formats . .	44
2.11	R.D.Specialties wire-wound rod sizes and expected film thicknesses. .	50
3.1	Schematic of “slow vacuum filtration” technique, SWNT conc. profile and the resulting nematic aligned SWNT film. . . . .	56
3.2	SEM of nematic ordered SWNT films fabricated from SDBS, F87 and CTAB suspensions using slow filtration. . . . .	57
3.3	Nematic ordered SWNT film from metallic enriched DGU suspension.	58
3.4	Domain structure in nematic ordered SWNT films, analysis of SWNT alignment using “OrientationJ” and calculation of 2-D nematic order parameter. . . . .	61
3.5	Optical absorption spectra of SWNT surfactant suspension and metallic enriched SWNT suspension obtained through DGU. . . . .	67
3.6	Raman scattering spectra of films fabricated from starting SWNT suspension and metallic enriched DGU material. . . . .	68

4.1	Schematic diagram of acid anion intercalation in SWNT bundles and cryo-TEM image of SWNTs in ClSO <sub>3</sub> H . . . . .	75
4.2	Phase diagram of HiPco SWNTs in superacids and cross-polarized light micrographs showing SWNT microstructure at different SWNT concentrations. . . . .	76
4.3	Experimental setup used for fabrication of highly aligned SWNT macrostructures. . . . .	79
4.4	Optical micrographs of aligned SWNT macrostructures obtained by slow quenching of 200 ppm SWNT-ClSO <sub>3</sub> H solution with water. . . .	82
4.5	Optical micrographs of aligned SWNT macrostructures obtained by slow quenching of 1000 ppm SWNT-ClSO <sub>3</sub> H solution with water. . . .	83
4.6	Optical micrographs of aligned SWNT macrostructures obtained by slow quenching of 4000 ppm SWNT-ClSO <sub>3</sub> H solution with water. . . .	84
4.7	Investigation of SWNT alignment in a ribbon-like macrostructure using polarized Raman spectroscopy. . . . .	85
5.1	SEM images showing ordered assemblies of gold nanorods (GNRs), of various aspect ratios, on aligned SWNT films. . . . .	94
5.2	SEM image showing spontaneous alignment of short GNRs with SWNTs in a fiber. . . . .	95
5.3	Orientational distribution function for short GNRs on aligned SWNT macrostructures. . . . .	97
5.4	Optical images showing the spontaneous alignment of 2D gold triangles and platelets to underlying SWNTs in aligned SWNT films. . . . .	100
5.5	The various forces contributing to assembly and alignment of gold nanorods on SWNT substrates. . . . .	103

6.1	Schematic diagram of the two-step SWNT fibril fabrication process. .	110
6.2	Cartoon of experimental setup used for DEP experiments, and the expected electric field between electrodes, simulated using COMSOL.	111
6.3	Optical micrograph of a mini-fibril. Polarized Raman spectroscopy of a mini-fibril, demonstrating presence of SWNTs and lack of significant SWNT alignment. . . . .	115
6.4	Long working distance camera image of Tungsten tip inside SWNT-DOC-NaCl suspension with preformed mini-fibrils, and a DEP fibril attached to tip. . . . .	117
6.5	SEM images of a DEP fibril, fabricated from a SWNT-DOC-NaCl suspension. . . . .	118
6.6	Polarized Raman spectrum of a DEP fibril showing an alignment ratio of 5. . . . .	120
6.7	SEM of gold electrodes deposited on an annealed DEP fibril, and the electrical transport properties. . . . .	121
6.8	Development of length distribution of mini-fibrils in suspension over time. . . . .	130
6.9	Chemical structure of DOC, and structurally similar molecules: cholesterol and testosterone. . . . .	131
6.10	Dielectric permittivity values for typical polymers over a wide range of frequencies. . . . .	133
6.11	Thermo-gravimetric analysis (TGA) of pure and dry surfactant DOC.	134
7.1	Size distribution, polydispersity and SEM images of giant graphene oxide (GGO) flakes prepared using improved Hummers method. . . .	139

7.2	Optical micrographs showing various mesophases of GGO aqueous suspension, large-area uniform nematic domains and schematic diagram depicting orientation of GGO flakes in nematic phase. . . . .	140
7.3	Anisotropic colloidal particles (gold microtriangles and glass micro-rods) and their spontaneous alignment in GGO nematic LC. . .	147
7.4	A half-integer $s = -1/2$ disclination in GGO LC director field obtained by solvent evaporation under the confinement of a glass slide and cover slip. . . . .	149
7.5	Quadrupolar distortions in nematic director field around spherical particle inclusions, demonstrating “homeotropic” surface anchoring of director, <i>ansatz</i> of LC director around the particles and computer simulation of polarizing optical micrographs. . . . .	152

## Tables

2.1	Relative electro-optical performance of “test” films made from coating fluids containing different surfactants. . . . .	22
2.2	List of physical properties, coating related numbers and time-scales for the SWNT-SDBS dispersion and modified values after addition of Triton X100. . . . .	28
3.1	Order parameters and domain sizes for nematic ordered SWNT films prepared from various surfactant suspensions, and a random network SWNT film prepared by fast filtration. . . . .	60
5.1	2D scalar order parameter values for GNR arrays deposited on aligned SWNT films and fibers. . . . .	99
6.1	Various microstructures formed by addition of varying amounts of NaCl in an aqueous SWNT-DOC suspension. . . . .	113
6.2	Dimensionless quantities $T_{\text{DEP-B}}$ and $R_{\text{DEP-B}}$ quantifying the relative strengths of translational and rotational DEP and Brownian forces on individual SWNTs and mini-fibrils in liquid suspension. . . . .	127

# Chapter 1

## Introduction

Single-walled carbon nanotubes (SWNTs) are cylindrical shaped allotropes of carbon, around one nanometer in diameter and an aspect ratio of  $\sim 1000$  or more. They can be visualized as a single sheet of graphene rolled up along a chiral vector  $C_h=na_1+ma_2$ , (Fig. 1.1), where  $n, m$  are integers and  $a_1, a_2$  are unit vectors of graphite. The  $(n, m)$  indices uniquely specify the geometric structure, diameter ( $d = |C_h|/\pi = a\sqrt{n^2 + nm + m^2}/\pi$ , where  $a=1.42 \times \sqrt{3} \text{ \AA}$  is the lattice constant), chirality and electronic behavior of an individual SWNT. SWNTs can be direct band-gap semiconductors, small band-gap semi-metal or zero band-gap true metal [Bachilo *et al.* 2002, O'Connell *et al.* 2002]. They possess extraordinary mechanical strength, unique electrical properties, high current carrying capacity and thermal conductivity due to the network of strong  $sp^2$  bonds and conjugated benzene rings with delocalized electrons.

Carbon nanotubes (CNTs) in general, and SWNTs in particular, have been the subject of intense research over the last two decades. Early research (1990s and early 2000s) on SWNTs was primarily focused on the issues of synthesis, investigation of



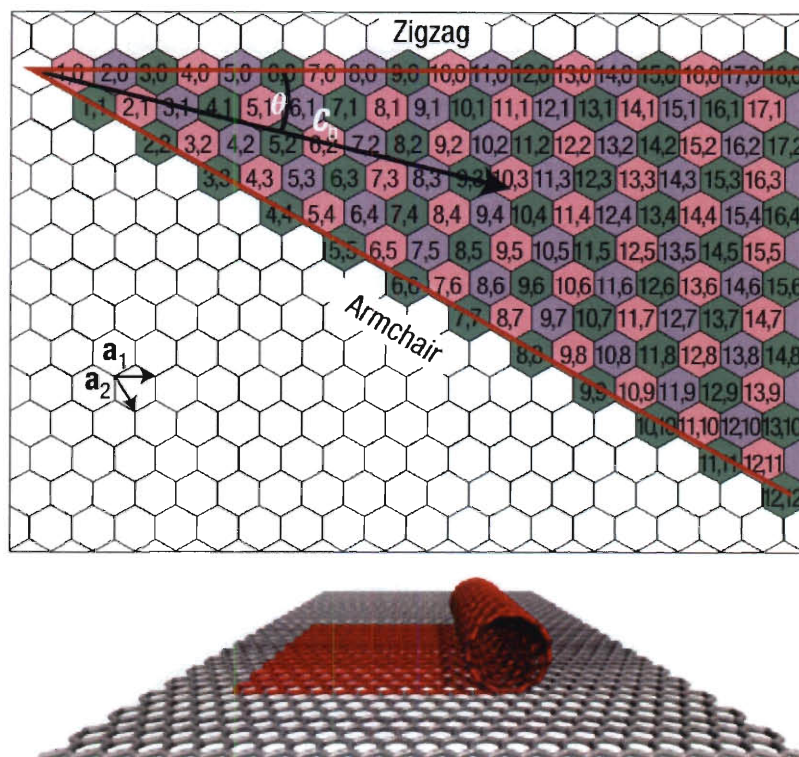


Figure 1.1 : A SWNT can be conceptualized as a graphene sheet rolled up along the “chiral vector” to form a cylinder. The chiral vector forms the circumference of SWNT and determines its diameter as  $C_h = na_1 + ma_2$ , where  $(n,m)$  are integers known as the chiral indices and  $a_1$  and  $a_2$  are unit vectors of the graphene lattice. (part of the image reproduced from ref. [Hersan 2008] , without permission).

fundamental properties and characterization.

## 1.1 SWNT Synthesis

Over the years, several techniques have been developed for scalable, reliable and efficient production of SWNTs. The techniques are progressively improving in their control over SWNT average diameter, length and polydispersity, the reactor product mix (SWNTs vs. multi-walled nanotubes), yield and defect density. Most common SWNT synthesis techniques include arc discharge [Bethune *et al.* 1993, Ebbesen and Ajayan 1992], laser ablation [Thess *et al.* 1996], high pressure carbon monoxide decomposition (HiPco) [Bronikowski *et al.* 2001], and chemical vapor deposition (CVD) [Kong *et al.* 1998]. Several variations have also developed within each of these techniques, offering different mix of quality, quantity and selectivity. In spite of notable progress in this field, a complete understanding of SWNT growth mechanism is still lacking. Consequently, current synthesis methods often suffer from hurdles like incomplete conversion of carbon feedstock, presence of impurities, and limited capability for large scale production.

## 1.2 SWNT Optical Properties

Much work has been done on investigation of fundamental optical properties of SWNTs. Theoretical models [Mintmire and White 1998, Saito *et al.* 2009] show

that the electronic energy states in SWNTs are distributed in sharp bands, known as Van Hove singularities (VHS) (Fig. 1.2(a)); transition of carriers between these states governs their optical absorption. Characteristic absorption peaks of SWNTs in the visible and NIR frequency regime are shown in Fig. 1.2(b). The semiconducting SWNTs possess a band-gap, which leads to carrier excitation and fluorescence emission. Bachilo et al. performed spectrofluorimetric measurements on surfactant stabilized individual SWNTs in aqueous suspensions where they observed the distinct electronic absorption and emission transitions of more than 30 different chiralities of semiconducting SWNTs, Fig. 1.2 [Bachilo *et al.* 2002]. The experimental information helped validate empirical relationships between the band-gap of semiconducting SWNTs and their diameter.

SWNTs also respond to Raman spectroscopy, which is a useful tool to probe their structural, electronic and phonon properties. The typical Raman spectrum of SWNTs, shown in Fig. 1.2(d), consists of: “radial breathing mode” (RBM, 100-250  $\text{cm}^{-1}$ ), where all carbon atoms move in-phase in the radial direction (breathe in and out motion), the “G-band” (1591  $\text{cm}^{-1}$ ) where neighboring atoms move in opposite directions along the surface of the tube, disorder induced “D-band” (1320  $\text{cm}^{-1}$ ) and its second-order related harmonic “G'-band”. The RBM is strongly sensitive to nanotube diameter ( $d_t$ ); the RBM Raman shift is related to the SWNT diameter as:  $\omega_{RBM} = \frac{A}{d_t} + B$ , where  $A$  and  $B$  are constants. Typically for SWNTs with  $d_t \sim 1.5$

nm,  $A=234 \text{ cm}^{-1}$  and  $B=10 \text{ cm}^{-1}$  [Dresselhaus *et al.* 2005].

UV-vis-NIR optical absorption, Raman spectroscopy and fluorescence mapping are all valuable tools for characterization of bulk SWNT samples.

### 1.3 SWNT Electrical Properties

Electrical transport measurements were performed on devices consisting of two crossed nanotubes, by Fuhrer *et al.* [2000]. The experiments revealed that a junction between two SWNTs of different electronic type suffers from mismatch in fermi levels, resulting in high resistance known as “junction resistance”. Junction resistance has profound effects on the performance of SWNT based macroscopic materials and devices. SWNT thin films, electrodes, fibers and other bulk materials are invariably composed of network of SWNTs and the junctions act as high resistance bottlenecks to carrier transport, limiting their electrical conductivity. This challenging and often paralyzing problem has given birth to new directions in current research. There is renewed interest in a better understanding of SWNT growth mechanism and developing novel methods to synthesize SWNTs of single chirality or electronic type [Harutyunyan *et al.* 2009]. Parallel efforts are being devoted on development scalable techniques for post-synthesis separation of semiconducting and metallic type SWNTs [Arnold *et al.* 2006, Krupke *et al.* 2003].

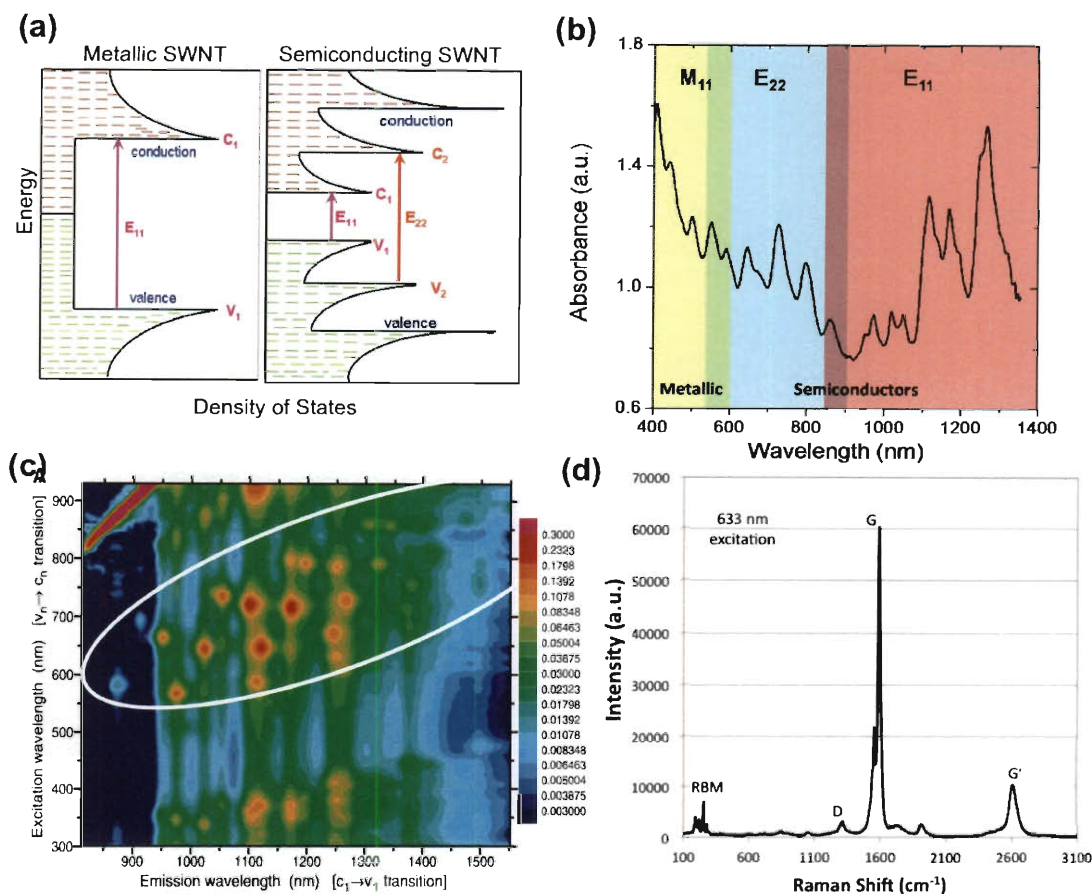


Figure 1.2 : Electronic structure and spectroscopic characterization tools for SWNTs. (a) The density of states of metallic and semiconducting SWNTs, showing the Van Hove singularities ( $C_i$ ,  $V_i$ ) and corresponding optical transitions ( $E_{ii}$ ). (b) UV-vis-NIR absorption spectrum of HiPco SWNTs, suspended in aqueous SDS suspension, and showing the characteristic absorption peaks of various SWNT chiralities and electronic types. (c) The fluorescence map of different chiralities of semiconducting HiPco SWNTs detected in a SDS aqueous ( $D_2O$ ) suspension. (d) The main features in the Raman spectrum of raw SWNTs. (parts of image reproduced from ref. [Bachilo *et al.* 2002], and Thesis of Dr. J.Duque (Rice Univ.), without permission).

## 1.4 Current SWNT Research

In recent years, SWNT research has trended towards engineering of advanced nanomaterials and devices for commercially viable applications. In 2004, Rinzler and co-workers [Wu *et al.* 2004] demonstrated optically transparent and electrically conductive SWNT thin films ( $\sim 20\text{-}400$  nm thick), with electro-optical properties comparable to Indium Tin Oxide (ITO). SWNT transparent conductive films are superior to ITO in terms of flexibility, durability, chemical inertness and thermal stability. Consequently, they are being pursued for next generation of touch screens, electronic displays, smart windows, electromagnetic shields, electrodes for organic light emitting diodes and photovoltaic cells [Hu *et al.* 2010]. Thicker and free standing SWNT films (also known as buckypaper), serve as excellent supports for catalyst nanoparticles in electrochemical electrodes, due to their porous network structure, high surface area ( $\sim 1300$  m<sup>2</sup>/g), high conductivity, and chemical and thermal stability.

Individual SWNT molecules are the strongest known polymers [Green *et al.* 2009]. Their small diameter, high aspect ratio, and a natural tendency to form bundles via van der Waals interactions make them ideal candidates for high strength, lightweight and conductive fibers; research and development in this area has already produced promising results [Davis *et al.* 2009, Koziol *et al.* 2007]. An ideal SWNT fiber can potentially be stronger than Kevlar, more thermally conductive than diamond, and more electrically conductive than copper while being 8 times lighter than the metal.

In spite of recent successes in lab scale development of SWNT materials and devices, scientific knowledge about processing SWNTs into macroscopic and useful products is still scarce and is a topic of extensive current research. Much as in polymer science and engineering, commercially viable applications can only be attained by developing appropriate scalable processes that translate the properties of the elemental molecules (SWNTs) into macroscopic materials. The research presented in this Thesis largely follows this goal.

## 1.5 Thesis Outline

The Thesis is organized as follows:

- In Chapter 2, a recipe for formulation of an aqueous colloidal suspension with high SWNT concentration is presented. A combination of two surfactants provides optimal rheological behavior for “rod coating” uniform transparent conductive SWNT thin films, with minimal dewetting, rupture and defects. “Doping” with acids and metallic nanoparticles yields SWNT films with electrical sheet resistance of 100 and 300  $\Omega/sq$  for respective optical transparency of 70% and 90%.
- In Chapter 3, fabrication of SWNT thin films with local nematic ordering and alignment using a “slow vacuum filtration” process is presented. The technique

is successfully demonstrated on several aqueous SWNT suspensions, employing different ionic and non-ionic surfactants, as well as on dispersions enriched in metallic SWNTs, produced by density gradient ultracentrifugation. Scanning electron microscopy and image analysis revealed a local nematic order parameter of  $S \sim 0.7-0.8$  for the SWNT films.

- In Chapter 4, a method for fabrication of aligned SWNT ribbons and flakes from SWNT-superacid solutions is presented. Pristine SWNTs are dissolved in chlorosulfonic acid at dilute and semi-dilute concentrations. Slow exposure to moisture leads a gradual reduction in acid strength (i.e., solvent quality) leading to phase transition of SWNTs to an ordered phase and precipitation of aligned SWNT structures.
- In Chapter 5, aligned SWNT macrostructures are employed as templates for large scale highly oriented assembly of plasmonic nanoparticles, like gold nanorods, micro-triangles and platelets.
- In Chapter 6, a novel two-step technique for fabrication of 1-D SWNT fibrils is presented. The technique employs a combination of colloidal self-assembly of surfactant stabilized SWNTs and AC dielectrophoresis (DEP). The self-assembled SWNT-surfactant colloidal structures are shown to be  $10^3 - 10^4$  fold more responsive to external AC electrical fields. The DEP SWNT fibrils are



characterized using optical microscopy, Raman spectroscopy and 4-point electrical probe.

- In Chapter 7, a detailed study on the phase behavior of giant graphene oxide flakes (aspect ratio  $> 10^4$ ) suspended in water is presented. The lyotropic suspensions transition from an isotropic to a biphasic system and to a discotic nematic liquid crystal with increasing flake concentration. Polarizing optical microscopy and colloidal particle inclusions reveal the alignment and orientation flakes in the nematic phase, the nematic order parameter ( $S \sim 0.43$ ), low optical birefringence ( $\Delta n = -0.0018$ ), and an average Frank elastic constant ( $K \sim 100$  pN) which is about 100 fold higher than previously studied discotic liquid crystals.

Each chapter is immediately followed by an appendix section where details of experimental procedure, analysis and characterization techniques are provided.

## Chapter 2

# Transparent Conductive SWNT Films

### 2.1 Introduction

Carbon nanotubes (CNTs) combine nanoscale size with high aspect ratio ( $\sim 1000$ ) and unique electrical, optical, mechanical and electrochemical properties [Liang *et al.* 2001, Maeda *et al.* 2005, Serp *et al.* 2003, Tans *et al.* 1997, Tatsuura *et al.* 2003, Yakobson and Avouris 2001], making them ideal candidate materials for high-impact applications in various fields [Baughman *et al.* 2002]. Yet, much as in polymer science and engineering, such applications can only be attained by developing appropriate scalable processes that translate the properties of the elemental molecules (SWNTs) or particles (CNTs) into macroscopic materials. Scientific knowledge about processing SWNTs into macroscopic and commercially useful products is still scarce and is a topic of extensive current research. An important recent success in this area has been the fabrication of optically transparent and electrically conducting thin films of pure SWNTs. Such transparent and conductive thin films or coatings may replace Indium Tin Oxide (ITO) in a wide range of applications, e.g., in touch screens, flat panel

---

Part of this chapter has been published in Dan *et al.*, ACS Nano 3 (4), pp 835-843 (2009).

displays, image recorders, optical communication devices, and solar cells [Chopra *et al.* 1983, Granqvist and Hultker 2002].

Nanotube films have been fabricated by vacuum filtration [Green and Hersam 2008, Parekh *et al.* 2007, Wu *et al.* 2004], transfer printing onto various substrates [Hu *et al.* 2004, Zhou *et al.* 2006], drawing from vertically oriented nanotube forests [Zhang *et al.* 2005], spin coating [Meitl *et al.* 2004], drop casting from SWNT dispersions [Sreekumar *et al.* 2003], quasi-Langmuir-Blodgett deposition [Armitage *et al.* 2004], dip-coating [Spotnitz *et al.* 2004], direct CVD growth [Ma *et al.* 2007], air-spraying [Geng *et al.* 2007, Kaempgen *et al.* 2005], and, after suitable functionalization, wire-wound rod coating [Yu *et al.* 2006; 2008], and slot coating [Rowley *et al.* 2006a]. However, most of these processes cannot be ported easily to large scale production-with exception of air-spraying, which has the drawback of forming sparse and relatively non-uniform networks [Geng *et al.* 2007], and rod and slot coating, which are scalable methods but have so far have required functionalized CNTs [Rowley *et al.* 2006a;b, Yu *et al.* 2006; 2008]. Here we report fabrication of SWNT films by “draw-down Mayer rod coating” (rod coating) process using pristine SWNTs.

## 2.2 Fabrication Method: Rod Coating

Draw-down rod coating is a well known coating technique widely used by laboratories in the coating industry for making liquid thin films in a continuous and controlled

manner [Mayer 1911]. Fluids that can be coated effectively by the Mayer rod method can then be readily adapted to more controllable, higher throughput methods such as slot, slide, and roll coating [Cohen and Guttoff 1992, Kistler and Schweizer 1997]. Figure 2.1(a) shows a schematic diagram of the rod coater with the wire-wound Mayer rod.

The coating apparatus (obtained from R. D. Specialties, Webster, NY) consists of a glass drawdown pad and a stainless steel rod wound tightly with stainless steel wire. The substrate is held down on the drawdown glass pad using heavy duty clips; the Mayer rod rolls over the substrate, “doctoring off” the coating fluid (Fig. 2.1(b)). Part of the liquid flows through the grooves in the wire-wound rod and forms the thin liquid film. The diameter of the wound wire determines the size of the grooves and, hence, it controls the final thickness of the coated liquid film [Cohen and Guttoff 1992]. This technique can be used to coat dispersions directly onto polyethylene terephthalate (PET), glass and other substrates at room temperature and in a scalable way.

A critical aspect in the rod coating process is preparation of the coating fluid, which should have specific rheological (flow) behavior and wetting properties, including:

- The coating fluid should carry sufficient solids to form a uniform and continuous layer upon drying of the coated film.

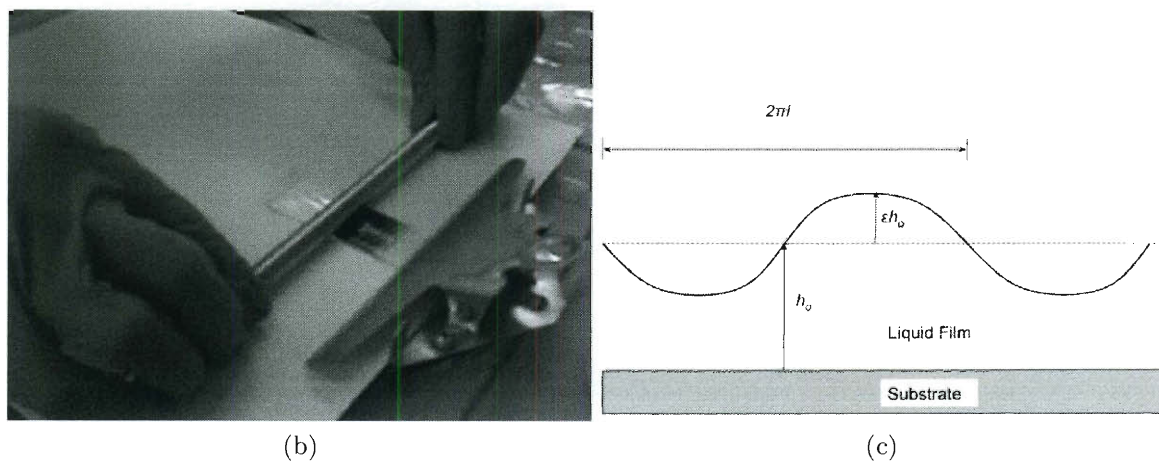
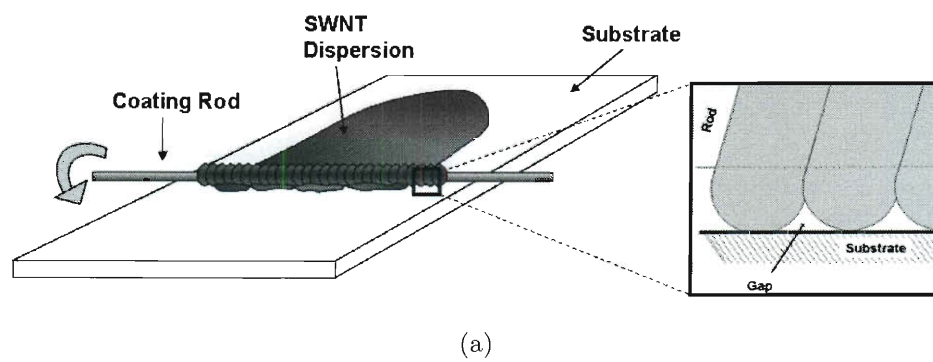


Figure 2.1 : (a) Schematic illustration of a drawdown rod coater with a wire-wound Mayer coating rod. (b) The laboratory scale draw down rod coating apparatus. (c) The free surface profile of a thin film immediately after Mayer rod coating.

- The surface tension of the coating fluid should be sufficiently low to facilitate its spreading on a wide range of substrates and avoid defects like contact line recession and dewetting.
- After deposition, the viscosity of the coating fluid should be sufficiently high to slow secondary flows induced by surface tension and dewetting forces, allowing the film to dry without flow.

The role of surface tension and viscosity in the context of coating flow can be understood by considering the capillary number  $C_a = \mu v / \sigma$  and Reynolds number  $Re = \rho v l / \mu$ , where  $\mu$  is the viscosity of the fluid,  $v$  is the characteristic velocity,  $\sigma$  is the surface tension,  $\rho$  is the fluid density and  $2\pi l$  is the wavelength of a sinusoidal disturbance.

In rod coating, the surface of the coated film is wavy (Fig.2.1(c)), and the waves must flatten before drying. Leveling process can be driven by two possible mechanisms: capillarity and gravity. For thin films (average film thickness  $h_o \ll$  capillary length  $\kappa^{-1} \sim \sqrt{\sigma/\rho g}$ ), gravitational effects are negligible compared to capillary effects. Capillary leveling is driven by hydrostatic pressure difference, caused by surface tension forces, between the convex and concave regions of the wavy liquid. Once the liquid is set in motion, inertial forces tend to maintain the motion causing overshoot from the desired flat equilibrium state (oscillations) whereas viscous forces tend to

slow down the leveling process by distributing the liquid momentum through the entire film thickness. A low Reynolds number ensures that viscous forces dominate inertial forces and any oscillations dampen out to give a flat film surface. A low capillary number ensures that capillary forces dominate the viscous forces and leveling occurs before the film can dry; equivalently, the leveling timescale  $t_{\text{level}} = 3\mu l^4 / (\sigma(h_0)^3)$  [Keunings and Bousfield 1987] is shorter than the film drying time  $t_{\text{dry}} = \Delta h / J_0$ , where  $J_0$  is solvent evaporation current (cm/s) and  $\Delta h$  is the thickness of liquid layer that must evaporate to cause gelation or solidification in the coated film.

During the drying process, i.e., time between leveling and solidification, the liquid thin film is exposed to various stresses including those due to de-wetting and non-uniform solvent evaporation; these stresses can induce secondary flows leading to contact line recession, film thinning and rupture. A high fluid viscosity is necessary to retard the secondary flows and ensure that the film is dry before these stresses can cause any significant damage. Further details of the de-wetting process are discussed in a later section. For a hand drawn rod coating process, like the one used in our case, optimal conditions require surface tension lower than 35-40 mN/m and viscosity in the range of 0.01-1 Pa·s - equivalently,  $C_a < 0.5$  and  $Re < 1$ , assuming typical coating speed of 2 cm/s and characteristic wavelength of 2 mm (diameter of wire on Mayer rod) [Cohen and Gutoff 1992].

Coating fluids are often non-Newtonian, i.e., their viscosity depends on shear

rate [Coyle *et al.* 1990, Kistler and Schweizer 1997, Pasquali and Scriven 2002]; this is certainly the case for carbon nanotube dispersions, which show shear-thinning even at dilute concentrations [Hobbie and Fry 2007, Parra-Vasquez *et al.* 2007, Rai *et al.* 2007]. Coating fluids experience widely different characteristic stresses (and therefore shear rates) in different regions of the flow. In the film formation region, the liquid flows at high shear rate (normally in the shear-thinning regime) through the grooves in the rod. In the coated film region, the liquid is subjected to much weaker de-wetting forces; therefore, it resists flow according to its zero-shear (or low-shear) viscosity. For our hand drawn rod coating process (shown in the inset of Fig.2.1), the characteristic shear rate in the film formation region is  $\sim 40 \text{ s}^{-1}$ . Therefore, the optimal coating fluid should have a viscosity in the range of 0.01-1 Pa-s at a shear rate  $\leq 40 \text{ s}^{-1}$ .

### 2.3 Figure of Merit

Before digging deeper in to formulation of carbon nanotube coating inks suitable for rod-coating and fabrication of transparent conductive SWNT thin films, it is important to establish an intuitive method for the purpose of evaluation and comparison of various transparent conductive thin films.

The performance of transparent conductive thin films is typically reported as sheet resistance  $R_s$  vs. transparency  $T$  plots. These plots show the trade off between the transparency and conductivity for thin films using a specific material. Another



intuitive way of comparing and evaluating the properties of various transparent conductive films is by using a *figure of merit* (FOM). The most commonly used FOMs for transparent conducting films were defined by Fraser et al. [1972] and Haacke et al. [1976] in the form of  $F_{tc} = T/R_s$  and  $\Phi_{tc} = T^x/R_s$  respectively, where  $T$  is the transmittance,  $R_s$  is the sheet resistance of the thin film and  $x$  is an arbitrary integer ( $\sim 10$ ) used for fixing the thickness at which maxima of  $\Phi_{tc}$  occurs. Both of these FOMs are functions of film thickness and are useful either for finding the optimum thickness of a transparent conductive film (for a given material) or for comparing different transparent conductive materials at a fixed film thickness.

For our analysis, we define a new FOM that is independent of thickness (for ideal films and for thickness smaller than wavelength of light) and allows immediate comparison between transparent conductors fabricated from different materials or by using different methods over the entire range of transparencies. A similar FOM was independently introduced in the recent patent literature [Spath *et al.* 2006]. According to the Beer-Lambert law, the transmission of light ( $T$ ) through a film of homogenous material can be modeled as  $T = I_1/I_0 = e^{-\alpha t}$ , where  $I_0$  and  $I_1$  are the intensity of incident and transmitted light,  $\alpha$  is the effective absorption coefficient, and  $t$  is the film thickness. The sheet resistance is defined as  $R_s = \rho/t$ , where  $\rho$  is the material

resistivity. Combining these two equations yields:

$$R_s = \frac{-\alpha\rho}{\ln T} \quad \text{or} \quad T = e^{\frac{-\alpha\rho}{R_s}} \quad (2.1)$$

We define  $\alpha\rho$  as the figure of merit ( $\text{FOM}_1$ ). The absorption coefficient ( $\alpha$ ) is not a fundamental material property, but it is very “commonly used because it can be easily measured and intuitively understood” [Dressel and Gruner 2002]. For a uniform and homogenous material,  $\alpha\rho$  is a constant parameter; therefore, sheet resistance depends linearly on  $(-1/\ln T)$  with  $\text{FOM}_1$  as the slope (Intuitively,  $\text{FOM}_1$  is also the sheet resistance of a film with a transparency of  $e^{-1} = 36.8\%$  ).  $\text{FOM}_1$  is useful for comparing transparent conductive films made from different materials or by using different methods— of course, films with lower FOM have better performance.

In the special case of a metallic thin film (film thickness much smaller than wavelength of light) in air, the electro-optical properties can be modeled as [Doherty *et al.* 2009, Dressel and Gruner 2002, Hu *et al.* 2004]:

$$T = \left(1 + \frac{2\pi}{c} \cdot \sigma_{ac} \cdot t\right)^{-2} = \left(1 + \frac{Z_0}{2 \cdot R_s} \cdot \frac{\sigma_{ac}}{\sigma_{dc}}\right)^{-2} \quad (2.2)$$

where  $\sigma_{dc}$  is the DC conductivity,  $\sigma_{ac}$  is the optical conductivity,  $c$  is the speed of light, and  $Z_0$  is the characteristic impedance of vacuum ( $\sim 376.73 \Omega$ ); both  $\sigma_{dc}$  and  $\sigma_{ac}$  are

fundamental properties of a material. A high value of  $\sigma_{dc}/\sigma_{ac}$  signifies a material with high conductivity and low optical absorption and hence a better candidate for transparent conductive thin films. Based on the above model, the ratio  $\sigma_{ac}/\sigma_{dc}$  can also be treated as a figure of merit (FOM<sub>2</sub>) [Doherty *et al.* 2009]. Performing a Taylor expansion of transparency vs. sheet resistance shows that Equations 2.1 and 2.2 coincide up to first order in sheet resistance by setting  $\alpha\rho = (Z_0/2)(\sigma_{ac}/\sigma_{dc})$  (they differ slightly at second order); they are also phenomenologically equivalent, as shown later on.

## 2.4 Coating Ink Formulation

Our coating fluids (or inks), to be used with the Mayer rod coating apparatus, consisted of aqueous dispersions of SWNTs stabilized by surfactants. Many surfactants disperse carbon nanotubes in water [Moore *et al.* 2003]; they differ in the stabilization mechanism (ionic vs. steric, micellization vs. polymeric wrapping), the maximum quantity of suspended SWNTs, the ratio of individual vs. bundled SWNTs present in the dispersion, the typical size of the bundles, and their propensity for forming lightly (or strongly) flocculated structures of SWNTs and SWNT bundles. All these factors can affect the coating process as well as the structure and performance of the final film. Four surfactants were chosen based on their proven effectiveness as SWNT dispersants in water [Moore *et al.* 2003]: F108 and F98 (Pluronics, polyethylene oxide

and polypropylene oxide based tri-block polymers - BASF), Sodium dodecyl sulfate (SDS - Aldrich) and Sodium dodecylbenzenesulfonate (SDBS - Aldrich).

To identify the optimal surfactant, coating fluids were prepared using the above surfactants. The coating fluids were prepared by mixing 0.3-0.4 wt% SWNT (HiPco Rice University; HPR 166.12) with 1 wt% of surfactant, using the technique developed by O'Connell et al. [2001]. The SWNT and surfactant concentrations were chosen based on the work by Vigolo et al. [2000]. These SWNT dispersions, as prepared, were unsuitable for coating uniform large area thin films. However, high SWNT loading (relatively higher viscosities) and thicker coated layers (20-50% transparency) allowed us to fabricate "test" films using rod coating. The test films were still partially defective (due to de-wetting and film rupture), but had large enough uniform regions ( $\sim 1 \text{ cm}^2$ ) to allow measurement of their electrical and optical properties. The coated films were air dried to allow the film to "set". Set films were then washed extensively to remove surfactant, by dipping them in a bath consisting of 1:1 (by volume) mixture of water and ethanol for about 1 hour and dried again overnight at  $80^\circ\text{C}$  under vacuum. Following this, all measurements were performed with the film exposed to ambient conditions. The electrical sheet resistance was measured using an Alessi four-point probe (probe spacing  $\sim 1 \text{ mm}$ ). The optical transparency was measured using a Shimadzu UV-VIS-NIR spectrophotometer.

Table 2.1 lists the FOM for our test films. Although all the films are essentially

Table 2.1 : Relative performance of “test” films made from coating fluids containing different surfactants. All coating fluids had 0.3-0.4 wt% SWNT and 1 wt% surfactant. The FOM reported in each case is an average over 5-6 films within the transparency range of 20-50%.

Coating fluid composition	FOM <sub>1</sub> of SWNT film ( $\Omega/sq$ )	FOM <sub>2</sub> of SWNT film
SWNT + F108	$472 \pm 98$	$2.56 \pm 0.78$
SWNT + F98	$472 \pm 108$	$3.35 \pm 2.12$
SWNT + SDS	$274 \pm 83$	$0.92 \pm 0.20$
SWNT + SDBS	$52 \pm 12$	$0.20 \pm 0.03$

composed by SWNTs alone (with minimal residual traces of surfactants), they show substantially different electro-optical properties. In particular, SDBS-based dispersions had five-fold performance advantage over films obtained from other dispersions.

These significant differences in properties can be understood based on the work by Hecht et al. [2006] on the conductivity  $\sigma_{dc}$  of SWNT films. These films have the morphology of disordered two-dimensional networks of SWNT bundles; their electrical conductivity is expected to depend on the average bundle length  $L_{av}$  and average diameter  $D_{av}$ :  $\sigma_{dc} \sim D_{av}^{-2}$ ,  $\sigma_{dc} \sim L_{av}^{1.46}$ . Compared to SDS and Triton X-100, SDBS is a better dispersing agent, yielding dispersions with higher concentration of individual SWNTs at the same overall SWNT concentration [Islam *et al.* 2003]. These differences in the SWNT microstructure (e.g., ratio of individual vs. bundles, average bundle diameter) in various dispersions are the likely cause of the different electro-optical properties of the final SWNT films.

Based on these observations, SDBS was selected as the surfactant of choice. Attaining higher transparency in films required coating fluids with lower concentration of SWNTs ( $\sim 0.1$  wt% for our rod coating setup), which had lower viscosity, required longer drying time, and therefore were more prone to forming defective films. The wetting and rheological properties of the SWNT dispersions were modified in order to eliminate film defects and non-uniformities due to de-wetting and film rupture. Redon et al. [1991] have studied the dynamics of de-wetting and breakage of thin liquid films by contact line recession and growth of dry regions. They showed that liquid films thinner than their characteristic equilibrium thickness  $h_e = 2\sqrt{\sigma/\rho g} \sin(\theta/2)$ , where  $\theta$  is the contact angle of the liquid with the substrate, ( $h_e \sim 400 \mu\text{m}$  for surfactant-water based systems), are metastable and always evolve towards equilibrium by either dewetting and shrinkage or by breaking up in to beads and patches. They also show that the dewetting velocity is  $V_{\text{dewet}} = (k\sigma/\mu) \cdot \theta^3$ , where  $k$  is a fluid property and can be taken as  $10^{-3}$  for primarily water based systems [Redon *et al.* 1991]. To avoid film rupture, the de-wetting velocity must be low so that the liquid film can dry before de-wetting causes any defects; equivalently, dewetting is avoided when the film drying time is much shorter than the de-wetting time  $t_{\text{dewet}} = L/V_{\text{dewet}}$ , where  $L$  is the characteristic length scale of the film. Therefore, dewetting can be avoided by lowering surface tension and contact angle, by raising viscosity, or by appropriately reducing the drying time of coated film.

In the case of SWNT-SDBS dispersions (0.1 wt% SWNT) the viscosity ranged from 6 mPa·s (at low shear rates) to 3 mPa·s (at high shear rates). The surface tension and contact angle with clean glass surface for the dispersion were measured using a goniometer and were found to be  $\sim 32$  mN/m and  $12^\circ$  respectively, which are typical for aqueous SDBS solutions above the critical micelle concentration (CMC of SDBS in water  $\sim 0.08$  wt%) [Mankowic 1965]. As the surfactant concentration of 1 wt% is safely above the CMC (even after accounting for surfactant adsorbed on SWNT surface,  $\sim 0.4$  wt% in case of SDBS with 0.1 wt% SWNT), the surface tension and contact angle are essentially independent of surfactant concentration. Therefore, we attempted to slow down de-wetting by enhancing the viscosity of the coating fluid, with the constraint that the fluid should still have sufficiently low viscosity to allow deposition using coating rod and leveling of the surface waves immediately after deposition.

The options for enhancing the viscosity and controlling the fluid rheology were limited because the stability of the SWNT-SDBS dispersion is very sensitive to additives; moreover, an electrically insulating additive can be used only if it is easily washable from the solid film to avoid losing conductivity; this discourages the use of high molecular weight polymers. Triton X-100, a non-ionic surfactant, was found to have a tremendous effect on the viscosity of SWNT-SDBS dispersion. Figure 2.2 shows the steady shear viscosity of our coating fluid before and after addition of Tri-

ton X-100; adding Triton X-100 to the SWNT-SDBS dispersion raised the zero-shear viscosity by about three orders of magnitude and the high-shear viscosity only by three to five-fold. The reason for the observed viscosity enhancement on addition of Triton X-100 is not entirely clear, as the exact nature of interaction between SDBS and Triton X-100 in the presence of SWNTs has not been studied before. Plausible explanations can be proposed based on similar prior observations in closely related systems. The addition of a neutral or oppositely charged surfactant or salt to another pure surfactant solution raises significantly the viscosity of some systems [Lin *et al.* 1994, Raghavan *et al.* 2002]. Adding a counter-ion or suitable co-surfactant results in dramatic changes in the surfactant micellar structure (e.g., from spherical to rod-like or worm-like), resulting in an equally dramatic increase in their shear viscosities. Previous studies [Vigolo *et al.* 2005, Wang *et al.* 2004] have shown that increasing the surfactant concentration in a SWNT-surfactant aqueous system leads to stickiness and depletion flocculation among SWNTs, which is also known to cause significant viscosity enhancements [Berli *et al.* 2002]. Both these effects, which are due to the formation of weakly associated network structures, change the rheological behavior of the system, especially at low shear rates. At high shear rates, the effect on the rheological properties is less pronounced because shear stresses break flocs and micelle networks; similar to the trend observed in our SWNT-mixed surfactant system. Figure 2.2 shows the optical micrographs of SWNT-SDBS and SWNT-SDBS-TritonX100



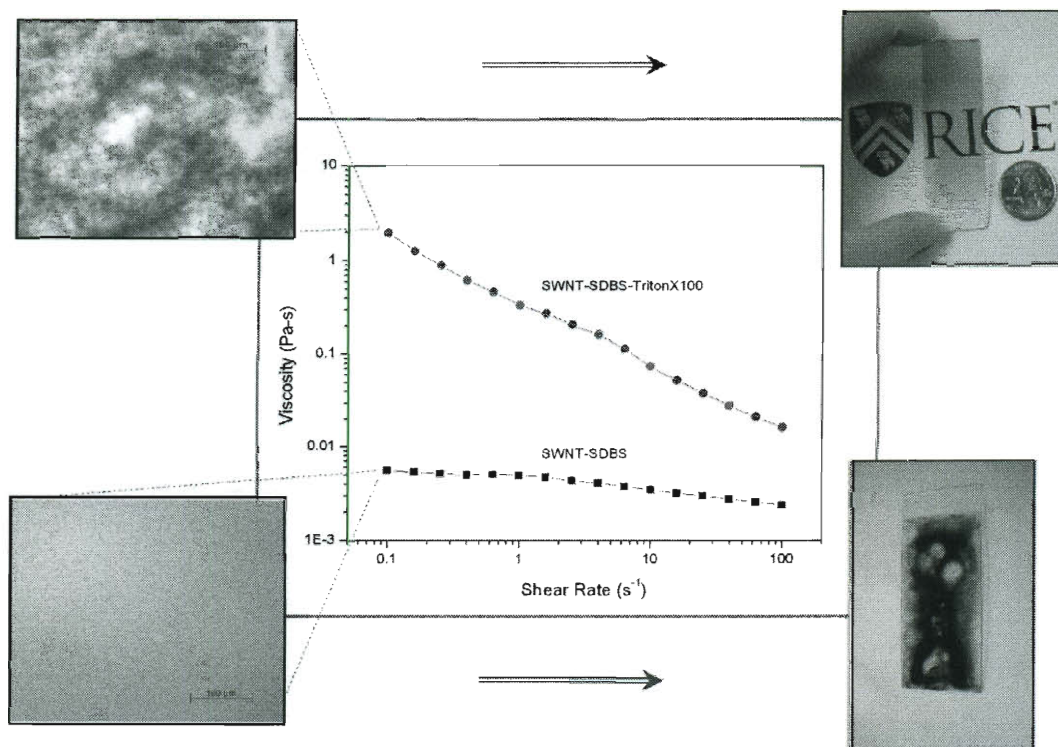


Figure 2.2 : Viscosity vs. shear rate for SWNT-SDBS dispersion and SWNT-SDBS-Triton X100 dispersion. The optical micrographs (left) show the different morphology of these two dispersions: in SDBS alone, the SWNTs are homogeneously dispersed as individuals and thin bundles; when Triton X100 is added, the SWNT and bundles form loose flocs. The formation of network of flocs raises the low-shear viscosity by  $\sim$  three orders of magnitude. Images of final dry films (right) showing that films formed from the SWNT-SDBS dispersion dewet and rupture, whereas films coated from the SWNT-SDBS-TX100 dry into a uniform thin structures. In all of the above cases, SWNT-SDBS dispersion had 0.1 wt% SWNT, 1 wt% SDBS. 3 wt% Triton X100 was added to it to obtain the SWNT-SDBS-TX100 dispersion.

dispersions, their viscosity as a function of shear rate and the corresponding SWNT films the dispersions produce.

Table 2.2 lists the capillary number, Reynolds number, de-wetting velocity ( $V_{\text{dewet}}$ ) and the timescales for leveling, drying, and de-wetting for both dispersions. The addition of Triton X-100 slowed down the dewetting process (by significantly increasing the low-shear viscosity), while also keeping the capillary number sufficiently low ( $< 1$ ). The leveling time  $t_{\text{level}}$  is calculated using the high-shear viscosity, as it represents the state of the fluid close to the coating rod. The dewetting time (derived from  $V_{\text{dewet}}$ ) is computed using the low-shear viscosity because the film is nearly stationary during drying. The time  $t_{\text{dry}}$  required to evaporate 80% of the solvent ( $t_{\text{dry}} = 0.8 \cdot h_0 / J_0$ ) was estimated by using solvent evaporation current  $J_0 = 1.5 \times 10^{-5}$  cm/s obtained from a drop drying experiment using SWNT-SDBS-TritonX100 dispersion (the same composition and ambient conditions used for rod coating); this evaporation current was then extrapolated to our 2.5 cm x 4 cm area and 100  $\mu\text{m}$  thick rod coated thin film to obtain the reported  $t_{\text{dry}}$ . Adding Triton X-100 increased the de-wetting time by two to three orders of magnitude while the leveling time, critical for film smoothness, grew only by a factor of  $\sim$  four and remained well below the drying time.

Table 2.2 : List of physical properties, coating related numbers and time-scales for the SWNT-SDBS dispersion and modified values after addition of Triton X100. The SWNT-SDBS dispersion had 0.1 wt% SWNT and 1 wt% SDBS. 3 wt% Triton X100 was added to get the modified SWNT-SDBS-Triton X100 dispersion.  $Ca$ ,  $Re$  and  $t_{\text{level}}$  were calculated using high shear viscosity,  $V_{\text{dewet}}$  and  $t_{\text{dewet}}$  were calculated using low shear viscosity. Length scale used for  $t_{\text{dewet}}$  and  $Re$  was  $2\pi l = 2 \text{ mm}$  (typical wavelength of irregularities left behind by coating rods) and a length scale ( $L$ ) of 1 mm ( $\sim 10\%$  of total width of the coated film) was used for estimating  $t_{\text{dewet}}$ . An average liquid film thickness of 100  $\mu\text{m}$  is assumed for all cases.

	Surface Tension (mN/m)	Low-shear Viscosity (at 0.1 s <sup>-1</sup> ) (mPa-s)	High-shear Viscosity (at 40 s <sup>-1</sup> ) (mPa-s)	$Ca$	$Re$	$t_{\text{level}}$ (s)	$t_{\text{dry}}$ (s)	$t_{\text{dewet}}$ (s)	$V_{\text{dewet}}$ ( $\mu$ /s)
SWNT-SDBS	31.8	6	3	$1.89 \times 10^{-3}$	2	$2.29 \times 10^{-3}$	530	21	47.63
SWNT-SDBS-Triton X100	31.4	2000	12	$7.6 \times 10^{-3}$	0.5	$9.28 \times 10^{-3}$	530	7092	0.14

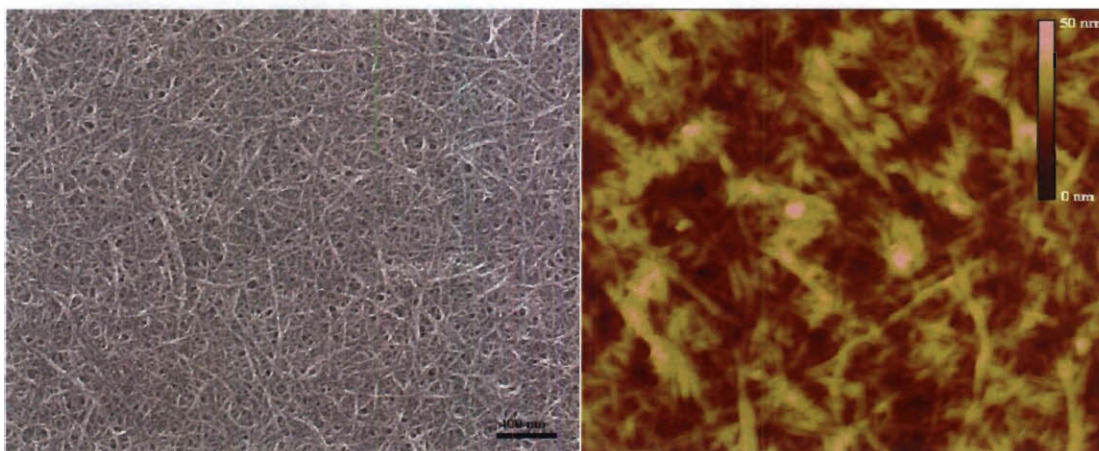


Figure 2.3 : SEM and AFM images of SWNT thin film on glass fabricated using the draw-down rod coating technique using SWNT-SDBS-TritonX100 dispersion (SWNT 0.1 wt%, SDBS 1 wt%, Triton X-100 3 wt%). Films coated with slightly different concentration of SWNT (0.1-0.3 wt%) and Triton X-100 (2-3%) yielded similar microstructure. The scale bar in the SEM scan is 400 nm and the AFM image is a  $2.5 \mu\text{m} \times 2.5 \mu\text{m}$  scan. The height scale bar in the AFM image is 50 nm.

## 2.5 Film Performance Characterization

Rod coating with the SWNT-SDBS-Triton X100 dispersion resulted in uniform, defect free thin film coatings. Figure 2.2 shows a highly-defective thin film coated on a microscope glass slide with the SWNT-SDBS dispersion and a uniform SWNT thin film coated with the SWNT-SDBS-Triton X-100 dispersion. Figure 2.3 shows the Scanning Electron Microscope (SEM) image and Atomic Force Microscope (AFM) image of the uniform film. Films as large as 20 cm x 20 cm were fabricated on glass surfaces as well as commercially available PET substrates using the rod coater.

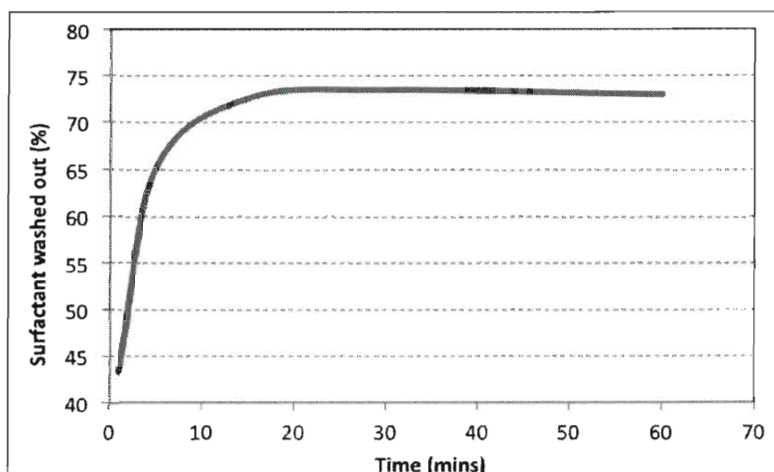
For all electro-optical measurements, SWNT films of area  $4 \times 2 \text{ cm}^2$  were coated on

glass slides using the above dispersion. The true bulk sheet resistance of the SWNT films were obtained by taking an average of 4 - 5 measurements performed at different locations on the film.

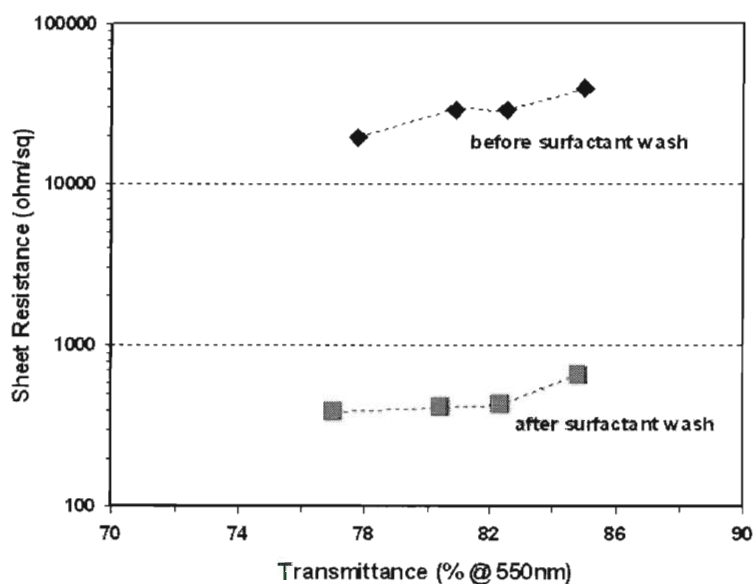
Our coating ink contains  $\sim 35$  times more surfactant than SWNTs, the electrically conductive material of interest, so effective removal of surfactant is of paramount importance for obtaining thin films with high optical transparency and low electrical resistance. Extensive washing by dipping in a 1:1 mixture of water and ethanol (polar organic solvent mixture in which both surfactants are highly soluble) was the main tool employed for removal of surfactant. The surfactant removal process was monitored by spectroscopically measuring the amount of surfactant in the wash bath as a function of time. Figure 2.4(a) shows a plot of surfactant in the wash bath (surfactant extracted from the film) as a function of time, normalized with total amount of surfactant expected to be present in the film. The removal of surfactant, followed by additional oven drying at 80 °C under vacuum, resulted in over 3 orders of magnitude improvement in thin film sheet resistance, as shown in Fig. 2.4(b).

## 2.6 SWNT Film Post-processing

The performance of rod coated and washed SWNT films, although promising, lagged behind the performance of ITO (the industry standard) and the requirement for certain high end transparent conductive coating applications; further improvements



(a)



(b)

Figure 2.4 : Effect of surfactant removal on the electrical sheet resistance of rod coated SWNT thin films (SWNT 0.1 wt%, SDBS 1 wt%, Triton X-100 3 wt%). (a) The amount of surfactant present in the wash bath (extracted from the film) as a function of time, normalized by total amount of surfactant expected to be present in the film (b) Electrical sheet resistance of SWNT films before and after surfactant removal.

in their electro-optical properties were sought for.

SWNTs networks and thin films are comprised of metallic as well as semiconductor type SWNTs; for example, the rod coated thin films made from HiPco SWNTs are expected to have  $\sim 1/3$  metallic and  $\sim 2/3$  semiconducting SWNTs. These two SWNT types differ in their work function, Fermi level and density of states, as shown in Fig. 2.5(a). Consequently, a junction between metallic and semiconducting SWNTs results in development of a Schottky barrier [Fuhrer *et al.* 2000].

A Schottky barrier is a potential barrier formed at metal-semiconductor junctions due to mismatch of Fermi levels, as shown in Fig. 2.5(b). Such a junction shows rectifying characteristics, similar to a diode, and severely restricts the charge carrier flow, effectively resulting in a high resistance, termed as “junction resistance” or “contact resistance”. The current through a Schottky barrier can be expressed as:

$$J = A^* T^2 e^{-\frac{qE_{sb}}{kT}} (e^{\frac{qV}{kT}} - 1) \quad (2.3)$$

where  $J$  is the current density,  $T$  is the absolute temperature,  $q$  is the charge,  $E_{sb}$  is the Schottky barrier height, and  $V$  is the applied voltage, and  $A^*$  is the effective Richardson constant.

---

$A^* = \lambda \cdot A_o$ , where  $\lambda$  is material specific correction factor  $\sim 0.5$  and  $A_o = \frac{4\pi m k^2 e}{h^3} = 1.20173 \times 10^6 \text{ Am}^{-2}\text{K}^{-2}$ ;  $m$  and  $-e$  are the mass and charge of an electron,  $h$  is Planck's constant,  $k$  is Boltzmann constant

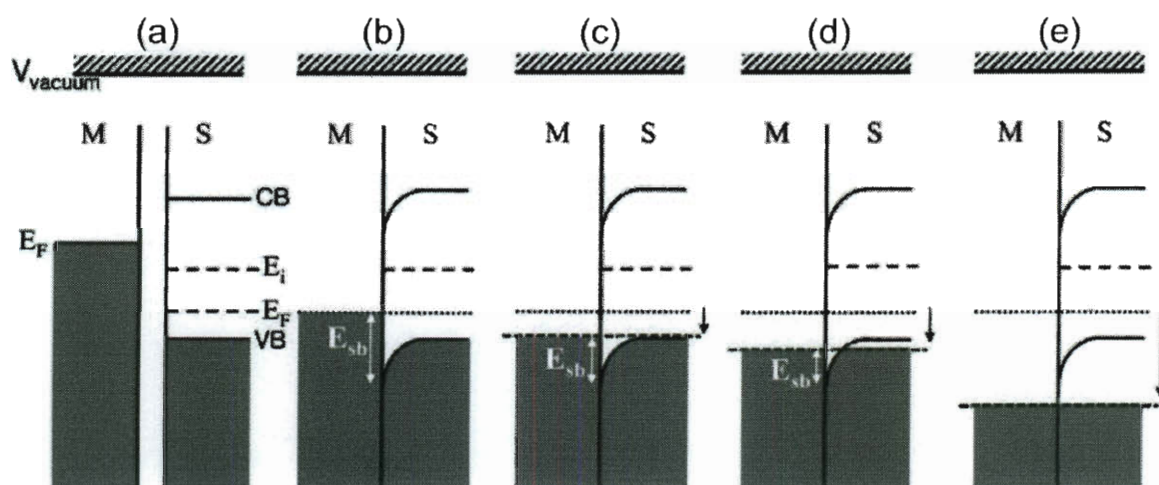


Figure 2.5 : A schematic representation of the junction between metallic and semiconducting SWNTs in a SWNT network. (a) a noncontact model, (b) the junction in the pristine sample, and (c-e) the junction with increasing amount of dopant ( $\text{AuCl}_3$ ). The Vacuum,  $E_i$ ,  $E_F$ ,  $CB$ ,  $VB$ , and  $E_{sb}$  indicate the vacuum level, the intrinsic Fermi level, the Fermi level after p-doping, the conduction band, the valence band, and the Schottky barrier, respectively. (Reproduced from [Kim *et al.* 2008] without permission)



In a SWNT thin film, these high resistance junctions act as bottlenecks for charge transport resulting in high thin film resistivity. An important observation from eq. 2.3 is that the current through a Schottky barrier is strongly controlled by the barrier height in the exponential. Therefore, one possible route for overcoming this issue is reduction and/or elimination of Schottky barrier via appropriate Fermi level engineering.

Two different approaches were investigated to improve the electrical conductivity of SWNT thin films via this route: doping with gold ions, and doping with strong acids.

### **2.6.1 Doping with Gold ions**

The effect of  $\text{AuCl}_3$  (chloroauric acid, source of  $\text{Au}^{3+}$  ions) doping on the electro-optical properties of SWNTs and SWNT networks was shown by Kim et al.[2008]. The reduction potential of an  $\text{Au}^{3+}$  ion is 1.52 V higher than that of SWNTs [Choi *et al.* 2002, Zhao *et al.* 2002]. So the charge transfer from SWNTs to Au ions occurs spontaneously, typically resulting in deposition of Au nanoparticles on SWNT surface [Choi *et al.* 2002] and a lowering of SWNT Fermi level, i.e., p-type doping. The effect of doping on SWNT Fermi level can be monitoring by measuring the van Hove electronic transitions, using UV-vis-NIR optical absorption spectroscopy. As reported by Kim et al. [2008], at low doping concentrations the van Hove singularity closest

to the Fermi level is modified first, resulting in quenching of semiconductor E11 optical transition. Increase in dopant concentration results in further lowering of Fermi level and quenching of semiconductor E22 and metallic E11 transitions, in that order. At high enough doping concentrations, the Schottky barrier is eliminated, resulting in easier carrier transport across SWNT junctions and lower resistivity of SWNT networks. The effect of doping on the Schottky barrier is shown in Fig. 2.5(c-e).

The Au ion doping experiment was performed on two film samples: film-1, 1630  $\Omega/\text{sq}$  at 90% transparency (@ 550 nm), and film-2, 370  $\Omega/\text{sq}$  at 80% transparency (@ 550 nm). Both films were prepared by rod coating, washed with water-ethanol mixture for surfactant removal and dried in vacuum oven, using the procedure mentioned before. Doping solvent was prepared with 80 mM  $\text{AuCl}_3$  in nitromethane. Few drops of the doping solvent was uniformly spread on the SWNT films. After 3 mins of residual time, the films were thoroughly washed with DI water and vacuum dried. The electrical sheet resistance before and after doping for both films, measured using 4-point probe, is shown in Fig. 2.6. Doping with Au ions resulted in 39% and 27% decrease in film sheet resistances, with negligible change in optical transmittance.

### **2.6.2 Treatment with Strong Acids**

Another route investigated for improvement in the electrical conductivity of SWNT film coatings was by treatment with various strong acids. Although significant and

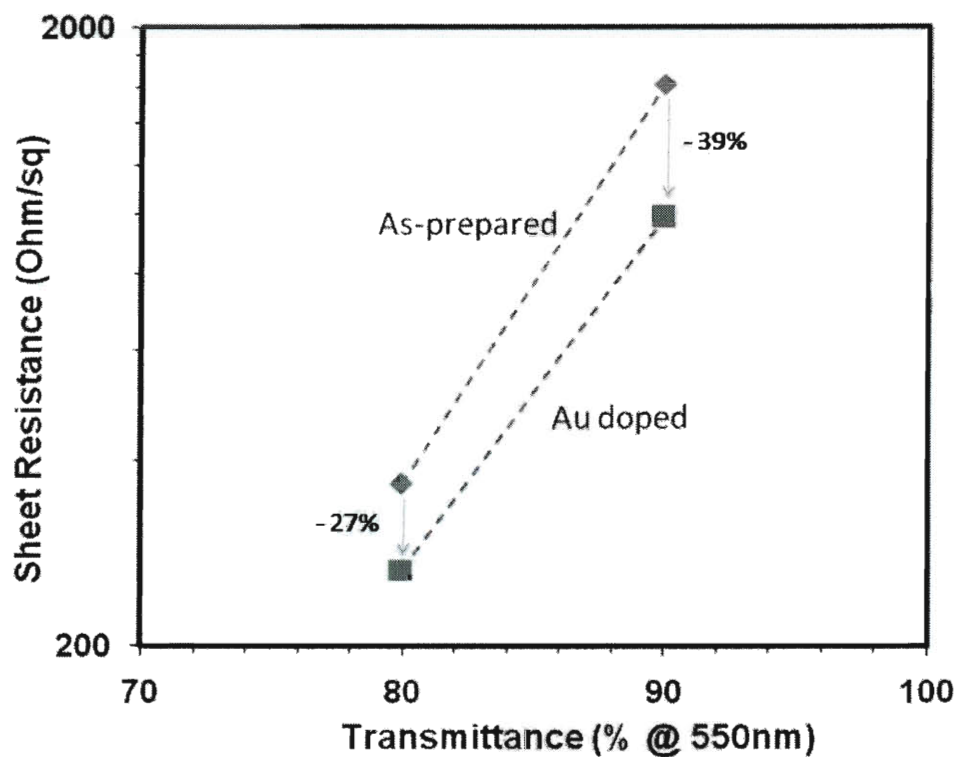


Figure 2.6 : The effect of Au doping on the electrical sheet resistance of SWNT thin films. Two rod coated and surfactant washed SWNT films ( $1630 \Omega/\text{sq}$  and  $370 \Omega/\text{sq}$  at 90% and 80% transparency, respectively) were doped with 80 mM  $\text{AuCl}_3$  in nitromethane for 3 mins, followed by DI water wash and vacuum oven drying. Au doping resulted in 39% and 27% decrease in film sheet resistances, with negligible change in optical transmittance.

stable improvement in the electrical properties of SWNT materials upon acid treatment has been reported before [Ericson *et al.* 2004, Geng *et al.* 2007, Zhou *et al.* 2005], the cause is still a matter of debate. Upon treatment with acids, Geng *et al.* [2007] observed a five-fold increase in the electrical conductivity of SWNT thin films that had been made using a surfactant based dispersion and had been washed to remove residual surfactant. They proposed that the acid removed residual surfactant molecules adsorbed on the surface of the nanotubes, leading to better contact between nanotubes, densification of the films and improvement in overall electrical conduction properties. However, work on macroscopic SWNT fibers [Ericson *et al.* 2004, Zhou *et al.* 2005] spun from surfactant-free acid dispersions provides a different explanation. Ericson *et al.* [2004] and Zhou *et al.* [2005] showed by X-Ray Diffraction that strong acids like oleum penetrate SWNT bundles and networks forming a dense layer of intercalated anhydrous acid anions surrounding individual nanotubes. These physisorbed acid anions protonate and dope the nanotubes by forming charge-transfer complexes, improving their electrical conductivity. Acid doping is reversible and can be removed by heating the SWNTs in an inert or reducing environment [Vavro *et al.* 2003, Zhou *et al.* 2004b].

We acid treated our SWNT thin films by two different methods: wet treatment and vapor treatment. In wet treatment, the SWNT films were dipped in 12 M nitric acid or oleum ( $\text{H}_2\text{SO}_4$ : 20% excess  $\text{SO}_3$ ) for 30 minutes at room temperature, quenched for

30 min in diethyl ether or water and dried at 120°C under vacuum for 24 hours. For vapor treatment, the SWNT films were kept in a sealed, humidity free environment saturated with acid vapors and maintained at high temperature ( $\sim 70^\circ\text{C}$  for nitric acid,  $\sim 120^\circ\text{C}$  for oleum) for 30 min, followed by 30 min of quenching in diethyl ether or water and drying at 120°C under vacuum for 24 hours. Acid treatment by both methods improved significantly (at least 3 fold) the electrical properties of the films while the transparency was unchanged. Figure 2.7(a) shows the optical transmission spectra of SWNT films before and after acid doping. Figure 2.7(b) plots the sheet resistance vs. transmittance for films with varying thicknesses, before and after the acid treatment. Sheet resistance as low as 80  $\Omega/\text{sq}$  and 140  $\Omega/\text{sq}$  for corresponding transmittances of 70% and 80% were obtained after this process. The improvement obtained by acid treatment was highly reproducible and the sheet resistance of films remained stable even after 8 weeks under ambient conditions.

## 2.7 Doped SWNT Film Performance Durability

Among the two routes investigated, acid treatment produced the most pronounced improvement in SWNT film electrical properties. Durability tests were performed on our acid treated as well as untreated SWNT films to study and compare the changes in their electrical conductivity on exposure to various harsh conditions. The tests involved three film samples: (a) rod coated and washed but without any acid

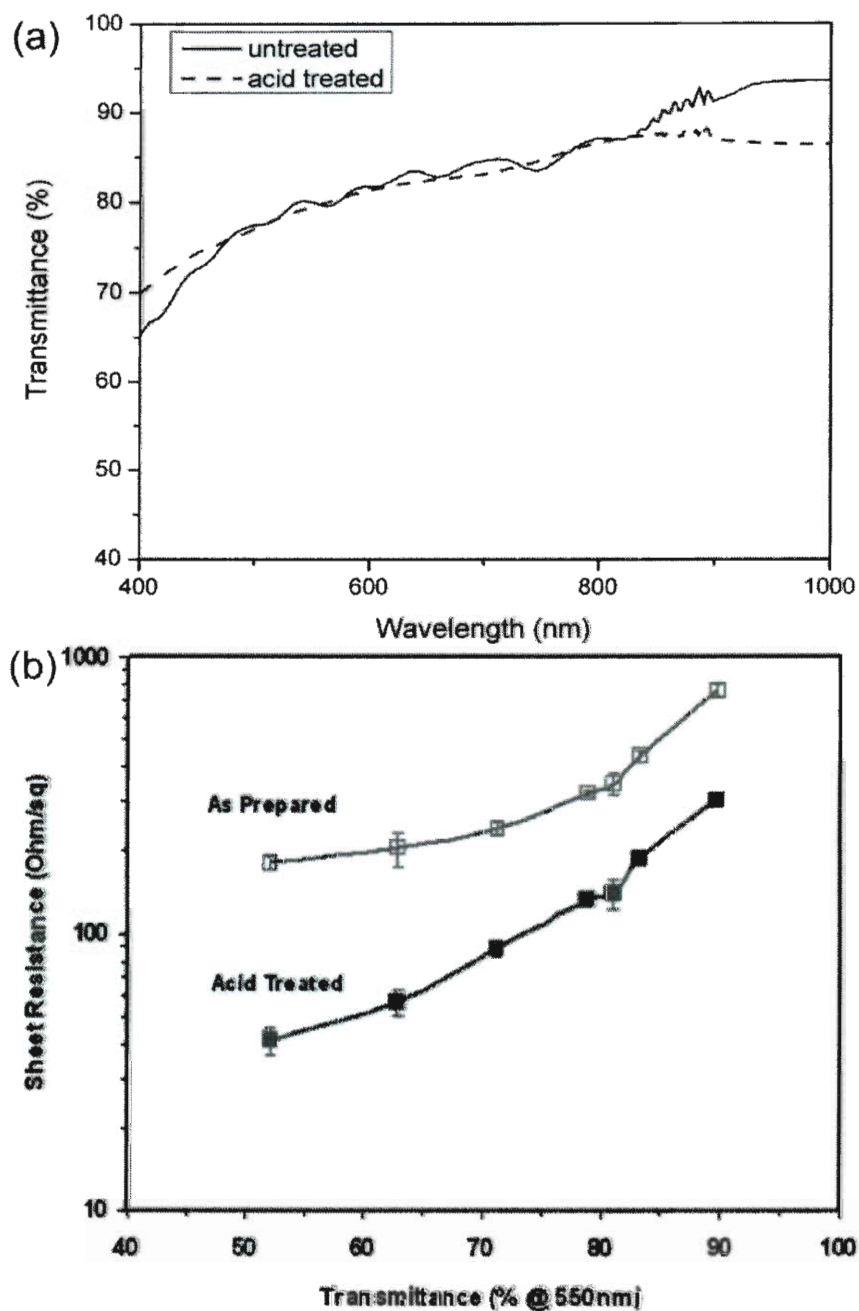


Figure 2.7 : Optical transmission spectra (a) and Sheet resistance vs. transmittance for a series of rod coated SWNT films with varying thicknesses (b), before and after oleum treatment. The films were rod coated from SWNT-SDBS-TritonX100 dispersion (SWNT 0.1 wt%, SDBS 1 wt%, Triton X-100 3 wt%). Sheet resistance of all films improved by more than factor of 3 upon acid treatment.

treatment (control sample), (b) rod coated, washed and treated with 12 M nitric acid and (c) rod coated, washed and treated with oleum. In one test, the films were immersed for 4 hour in a water bath at  $\sim 80^\circ\text{C}$ . In another test, the SWNT films were annealed for 4 hour at  $400^\circ\text{C}$  in an inert ( $\text{N}_2$ ) atmosphere. The results of these tests are summarized in Fig. 2.8. Both tests lowered the electrical conductivity of all the three films. However, the loss of conductivity was much higher for acid treated films than for the untreated film. Moreover, the extent of conductivity loss was different in the cases of nitric acid treated film and oleum treated film. These results show that the conductivity enhancement is due chiefly to the p-doping by acid anions intercalated and physisorbed in the SWNT network, although better removal of residual surfactant may also contribute to the effect.

## 2.8 Results

Figure 2.9 compares the performance of our roll coated SWNT films with other transparent conductive SWNT thin films published in the literature. Figure 2.10 shows the FOM plots for the same set of data using equations 2.1 and 2.2. In Fig.2.10(a) the slopes of the curves are equal to  $\alpha\rho$  ( $\text{FOM}_1$ ), whereas in Fig. 2.10(b) the slopes are  $(Z_0/2) \cdot (\sigma_{ac}/\sigma_{dc})$  or  $(Z_0/2) \cdot \text{FOM}_2$ ; in both cases, lower slope denotes more conductive and transparent material. As can be easily seen, both plots are essentially equivalent, showing similar trends (difference in slopes, deviations from straight line

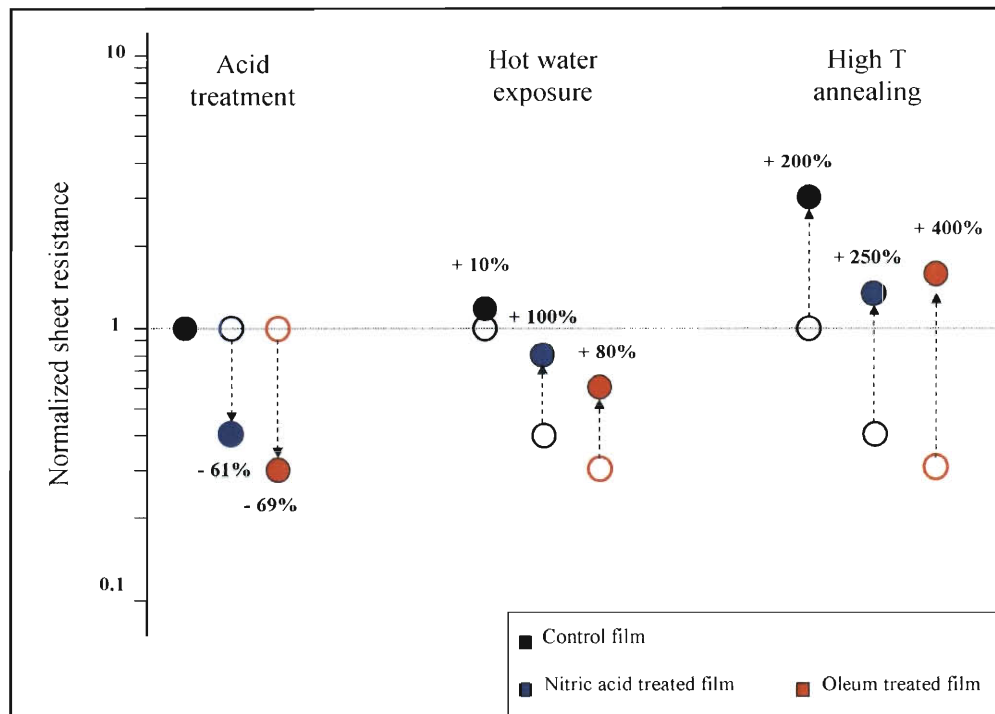


Figure 2.8 : Effect of acid treatment and durability tests (in 80°C hot water and 400°C N<sub>2</sub> environment) on the electrical properties of SWNT films: (black circle) rod coated, washed but without any acid treatment, (blue circle) rod coated, washed and dipped into with 12M nitric acid, (red circle) rod coated, washed and dipped into oleum.



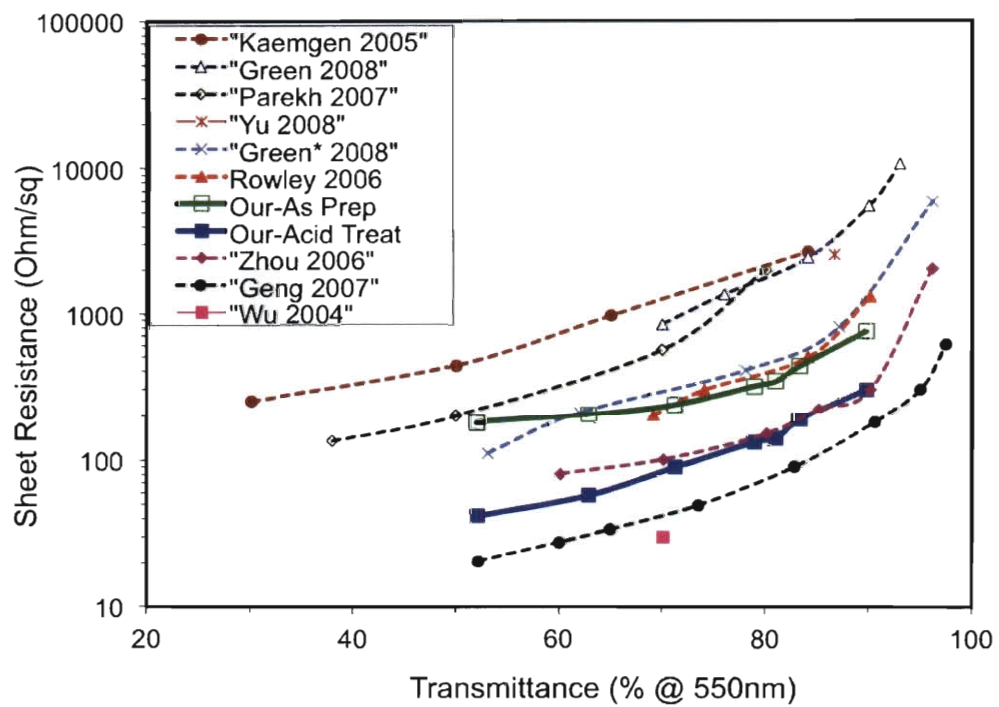


Figure 2.9 : Comparison of the electro-optical performance of our acid treated rod coated SWNT films with other transparent conductive SWNT thin films published in the literature.

behavior, etc.) in a similar fashion.

The FOM plots show that films made from the same material (SWNTs) but by different methods can display substantially different intrinsic material properties (based on the slope of the curves). The electrical and optical properties of a SWNT thin film depend on the network microstructure, which is controlled by the fabrication process. The FOM plots also display the critical transparency beyond which the assumption of homogeneous film (linear plot) fails. At higher transparencies, films are thinner and the constituent SWNT networks approach the limit of percolation; once percolation is lost, the assumption of homogenous material breaks down and the sheet resistance shoots up. Processes like rod coating maintain the linear relationship up to higher transparency because they yield better connected and packed SWNT networks; therefore, they are better suited for large-scale fabrication.

## 2.9 Conclusions

We present a highly scalable and continuous method for making uniform thin films of pristine SWNTs. A combination of surfactants was used to design a coating fluid with high concentration of SWNTs in water and optimal rheological and wetting behavior. The choice of surfactant had a strong effect on the rheological properties of the coating fluids as well as the electro-optical properties of the final SWNT films. Treatment with strong acids p-doped the SWNTs and improved the electrical con-

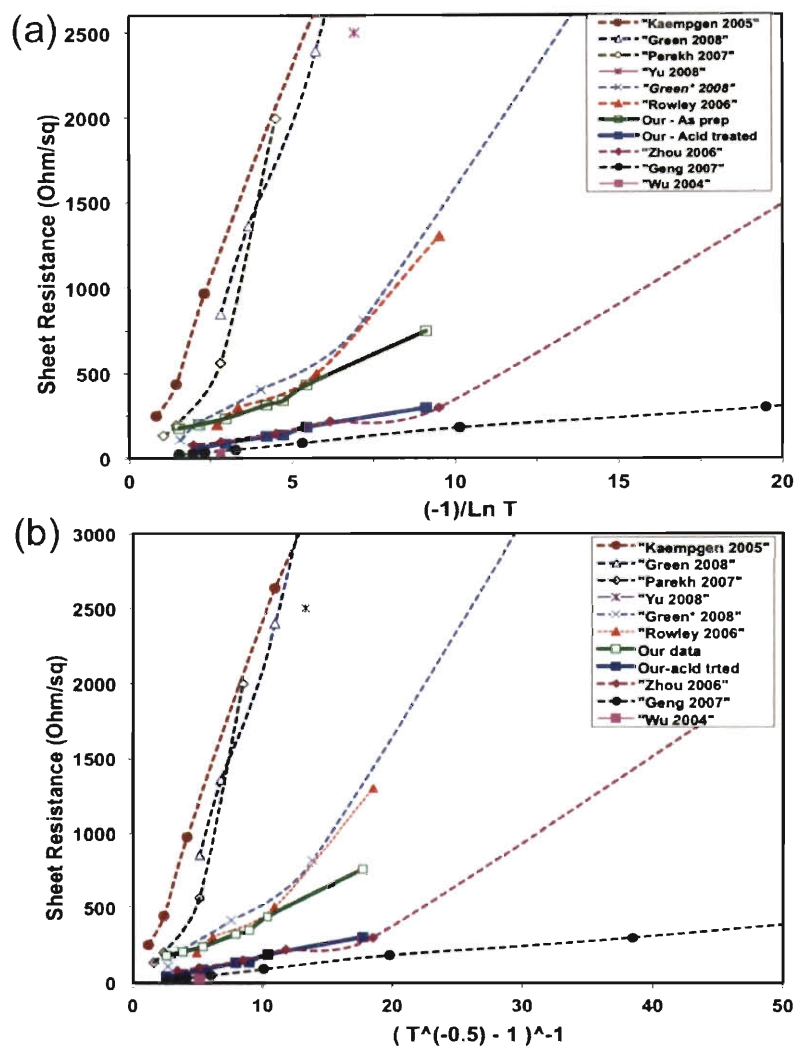


Figure 2.10 : (a) FOM plot of our acid treated rod coated SWNT films and other TC SWNT films published in literature, using equation 2.1. Slope of each line represents  $\alpha \cdot \rho$  ( $FOM_1$ ) for those films. (b) Plot of same data set using equation 2.2. Slope of the lines is  $(Z_0/2) \cdot (\sigma_{ac}/\sigma_{dc})$  or  $(Z_0/2) \cdot FOM_2$ . Lower slopes imply better electro-optical performance. In both graphs, higher  $x$  values indicate higher transparencies. Data sets are cited according to: “first author name, publication year”. (Green\* represents performance of metallic enriched SWNT films form [Green and Hersam 2008].)

ductivity of SWNT thin films by up to five-fold. The doping was stable at ambient conditions. The microstructure and electro-optical performance of the SWNT films was analyzed and compared with SWNT films fabricated by other methods using a FOM, showing that this method outperforms all other literature results except for recent air-spraying. The results presented here, both in terms of scientific understanding of how to control the fluid and processing, and in terms of a scalable technique that can be extended to higher-throughput methods (slot, slide, and roll coating) paves the way to the deployment of transparent conductive SWNT films in large scale commercial applications.

## **2.10 Appendix**

This appendix presents detailed sample preparation techniques, experimental procedures and characterization methods used in this chapter.

### **2.10.1 High Concentration SWNT Dispersions**

The basic procedure for preparation of SWNT-surfactant aqueous suspensions has been reported by O'Connell et al. [2001]. SWNT-surfactant colloidal suspensions for the purpose of coating, where a higher SWNT concentration is desired, were prepared using a slightly modified method as listed below:

1. Mix 1 wt% of desired surfactant and 30 ml of nanopure water in a vial. Stir or bath sonicate till surfactant dissolves completely (solution becomes “clear”).
2. Add 0.4 wt% (120 mg) purified HiPco SWNT in the surfactant-water solution.
3. Homogenize the mixture using a high shear homogenizer (for example, Fisher Scientific Catalog No. 14-261-04), at  $\sim 8000$  rpm for 45 mins. The head of the stator should be slightly lower than the mid-point of liquid column in the vial.
4. Sonicate the homogenized mixture using a 1/4 inch tip sonicator, at 35% amplitude for 30 mins. The end of the tip should be again slightly lower than the mid-point of liquid inside the vial. The vial should be placed in a cold water bath or ice bath to avoid heating during sonication.
5. Centrifuge the sonicated suspension at 5000 rpm for 15 mins. Collect the top 75% of liquid from each centrifuge tube using a pipette, without shaking the centrifuge tubes.

The above procedure typically produces a uniform SWNT-surfactant suspension with  $\sim 0.15$  wt% or higher SWNT loading. The suspension is expected to have individual SWNTs and small to medium size bundles ( $< 100$  nm diameter). The success of the procedure depends on the surfactant used and its efficacy in SWNT suspension. SDBS, Pluronic F87, CTAB, DOC are highly recommended.

In certain cases, the centrifugation step might not be feasible. For example, Triton X-100 is typically a very effective surfactant and the suspension appears similar to the case of SDBS (in texture, uniformity, optical density by visible inspection) till the end of sonication step. However, macroscopic, loose networks or flocculates appear within few minutes if the suspension is left undisturbed, which precipitate out during centrifugation. It is important to note here that the SWNTs in Triton X-100 are still stabilized and wrapped by surfactant, as indicated by lack of dark, particle-like aggregates under optical microscopy. The suspension regains a uniform and “non-flocculated” texture (temporarily) by just 2-5 minutes of bath sonication. This is in contrast to the case of other inefficient surfactants, which can typically suspended only a small fraction of SWNTs, but do so in a stable manner (capable of undergoing centrifugation). Undispersed SWNT matter can be easily observed as dark, particle-like aggregates under optical microscopy.

### **2.10.2 Preparation of SWNT Coating Fluid**

Suspension for rod coating was prepared by adding 2-3 wt% Triton X-100 in a SWNT(0.2 wt%)-SDBS(1 wt%) aqueous suspension. The suspension is maintained at 40-45°C with intermittent gentle swirling to aid Triton X-100 mixing; upon completion of mixing, it is kept undisturbed at room temperature. The introduction of Triton X-100 into the suspension begins the slow flocculation process immediately.

This is similar to the flocculation observed in SWNT-triton X-100 only suspensions, but to a much lesser extent presumably due to the presence of ionic SDBS, which has a stabilizing effect. A certain degree of flocculation is important to render a high 'low shear viscosity' to the suspension, critical for uniform and defect free coating. In 5 - 7 of undisturbed residual time, the suspension is ready for coating. This can be checked by coating 'test films'; once the flocculation has progressed to the desired level, post-coating contact line recession and dewetting of liquid film decreases markedly. The suspension remains optimum for coating for  $\sim 15 - 20$  mins, eventually the flocculation overwhelming the suspension uniformity.

### **2.10.3 Rod Coating Procedure**

The rod coating setup was bought from R.D.Specialties ([www.rdspecialties.com](http://www.rdspecialties.com)) and consisted of a 'drawdown' glass pad, with heavy duty clip as substrate holder, and a series of 'wire-wound' coating rods equipped with wires of varying diameters. The rod numbers (i.e., size of wire on the rod) and the corresponding expected wet film thicknesses can be found here 2.11. Various rods, with wire sizes ranging from 2 - 44 have been used for SWNT film coating. The ultimate liquid film thickness and dry SWNT film transmittance depends on the rheology of the coating fluid, fluid composition etc.

Coating was performed by placing a microscope glass slide (wiped cleaned with

IPA soaked kimwipe), with one end held under the clip, placing the coating rod on the end of the glass slide (immediately following the clip), pouring coating fluid ( $\sim 150 \mu\text{l}$ ) uniformly across the width of the glass slide in the form of a thick line and immediately in front of the coating rod, and rolling the rod at 1-2 cm/s speed in a smooth and uniform stroke across the length of the glass slide and past the other end (so that the extra coating fluid is doctored off the slide end). The coated films were dried either at room temperature or under a 100 W hot lamp.

#### **2.10.4 Acid Treatment Procedure**

Acid treatment was performed using two routes: wet treatment and vapor treatment.

In wet treatment, SWNT film coated microscope glass slides were dipped in 12 M nitric acid or Oleum ( $\text{H}_2\text{SO}_4$ : 20% excess  $\text{SO}_3$ ) kept in a 50 or 100 ml cylindrical beaker, in a glove bag (purged with dry  $\text{N}_2$ ) inside a fume hood. After 30 mins of residual time, the glass slides were transferred to a water or ether bath for quenching the acid. The washed SWNT films were dried in a vacuum oven at  $120^\circ\text{C}$  for at least 2 hours.

In vapor treatment, the SWNT film coated glass slides and a small amount of acid (in a tiny glass container) were placed inside a large glass petri dish and covered with a glass plate. This was performed inside a dry glove bag. The sealed petri dish was then transferred inside a vacuum oven (with no vacuum applied) maintained at a high



Wire Size (or equivalent)			Wet Film Thickness		Dry Coat Weight						Availability			
No.	Inch	mm	Mils	Microns	25% Solids		50% Solids		100% Solids		Wire Wound	Formed	Double Wound	Gapped
					GSM	#/3000	GSM	#/3000	GSM	#/3000				
2	0.002	0.05	0.18	4.57	1.14	0.70	2.29	1.40	4.57	2.81	•	•		
3	0.003	0.08	0.27	6.86	1.71	1.05	3.43	2.11	6.86	4.21	•	•		
4	0.004	0.10	0.36	9.14	2.29	1.40	4.57	2.81	9.14	5.62	•	•		
5	0.005	0.13	0.45	11.43	2.86	1.76	5.72	3.51	11.43	7.02	•	•		
6	0.006	0.15	0.54	13.72	3.43	2.11	6.86	4.21	13.72	8.43	•	•		
7	0.007	0.18	0.63	16.00	4.00	2.46	8.00	4.92	16.00	9.83	•	•		
8	0.008	0.20	0.72	18.29	4.57	2.81	9.14	5.62	18.29	11.24	•	•		
9	0.009	0.23	0.81	20.57	5.14	3.16	10.29	6.32	20.57	12.64	•	•		
10	0.010	0.25	0.90	22.86	5.72	3.51	11.43	7.02	22.86	14.05	•	•	•	
11	0.011	0.28	0.99	25.15	6.29	3.86	12.57	7.73	25.15	15.45	•	•	•	
12	0.012	0.30	1.08	27.43	6.86	4.21	13.72	8.43	27.43	16.86	•	•	•	
13	0.013	0.33	1.17	29.72	7.43	4.57	14.86	9.13	29.72	18.26	•	•	•	
14	0.014	0.36	1.26	32.00	8.00	4.92	16.00	9.83	32.00	19.67	•	•	•	
15	0.015	0.38	1.35	34.29	8.57	5.27	17.15	10.54	34.29	21.07	•	•	•	
16	0.016	0.41	1.44	36.58	9.14	5.62	18.29	11.24	36.58	22.48	•	•	•	
17	0.017	0.43	1.53	38.86	9.72	5.97	19.43	11.94	38.86	23.88	•	•	•	
18	0.018	0.46	1.62	41.15	10.29	6.32	20.57	12.64	41.15	25.29	•	•	•	
19	0.019	0.48	1.71	43.43	10.86	6.67	21.72	13.35	43.43	26.69	•	•	•	
20	0.020	0.51	1.80	45.72	11.43	7.02	22.86	14.05	45.72	28.10	•	•	•	
21	0.021	0.53	1.89	48.01	12.00	7.38	24.00	14.75	48.01	29.50	•	•	•	
22	0.022	0.56	1.98	50.29	12.57	7.73	25.15	15.45	50.29	30.91	•	•	•	
23	0.023	0.58	2.07	52.58	13.14	8.08	26.29	16.16	52.58	32.31	•	•	•	
24	0.024	0.61	2.16	54.86	13.72	8.43	27.43	16.86	54.86	33.72	•	•	•	
25	0.025	0.64	2.25	57.15	14.29	8.78	28.58	17.56	57.15	35.12	•	•	•	
26	0.026	0.66	2.34	59.44	14.86	9.13	29.72	18.26	59.44	36.53	•	•	•	
27	0.027	0.69	2.43	61.72	15.43	9.48	30.86	18.97	61.72	37.93	•	•	•	
28	0.028	0.71	2.52	64.01	16.00	9.83	32.00	19.67	64.01	39.34	•	•	•	
29	0.029	0.74	2.61	66.29	16.57	10.19	33.15	20.37	66.29	40.74	•	•	•	
30	0.030	0.76	2.70	68.58	17.15	10.54	34.29	21.07	68.58	42.15	•	•	•	•
31	0.031	0.79	2.79	70.87	17.72	10.89	35.43	21.78	70.87	43.55	•	•	•	•
32	0.032	0.81	2.88	73.15	18.29	11.24	36.58	22.48	73.15	44.96	•	•	•	•
33	0.033	0.84	2.97	75.44	18.86	11.59	37.72	23.18	75.44	46.36	•	•	•	•
34	0.034	0.86	3.06	77.72	19.43	11.94	38.86	23.88	77.72	47.77	•	•	•	•
35	0.035	0.89	3.15	80.01	20.00	12.29	40.01	24.59	80.01	49.17	•	•	•	•
36	0.036	0.91	3.24	82.30	20.57	12.64	41.15	25.29	82.30	50.58	•	•	•	•
37	0.037	0.94	3.33	84.58	21.15	13.00	42.29	25.99	84.58	51.98	•	•	•	•
38	0.038	0.97	3.42	86.87	21.72	13.35	43.43	26.69	86.87	53.39	•	•	•	•
39	0.039	0.99	3.51	89.15	22.29	13.70	44.58	27.40	89.15	54.79	•	•	•	•
40	0.040	1.02	3.60	91.44	22.86	14.05	45.72	28.10	91.44	56.20	•	•	•	•
42	0.042	1.07	3.78	96.01	24.00	14.75	48.01	29.50	96.01	59.01	•	•	•	•
44	0.044	1.12	3.96	100.58	25.15	15.45	50.29	30.91	100.58	61.82	•	•	•	•
45	0.045	1.14	4.05	102.87	25.72	15.81	51.44	31.61	102.87	63.22	•	•	•	•
46	0.046	1.17	4.14	105.16	26.29	16.16	52.58	32.31	105.16	64.63	•	•	•	•
48	0.048	1.22	4.32	109.73	27.43	16.86	54.86	33.72	109.73	67.44	•	•	•	•
50	0.050	1.27	4.50	114.30	28.58	17.56	57.15	35.12	114.30	70.25	•	•	•	•
55	0.055	1.40	4.95	125.73	31.43	19.32	62.87	38.63	125.73	77.27	•	•	•	•
60	0.060	1.52	5.40	137.16	34.29	21.07	68.58	42.15	137.16	84.29	•	•	•	•
65	0.065	1.65	5.85	148.59	37.15	22.83	74.30	45.66	148.59	91.32	•	•	•	•
70	0.070	1.78	6.30	160.02	40.01	24.59	80.01	49.17	160.02	98.34	•	•	•	•
75	0.075	1.91	6.75	171.45	42.86	26.34	85.73	52.68	171.45	105.37	•	•	•	•
80	0.080	2.03	7.20	182.88	45.72	28.10	91.44	56.20	182.88	112.39	•	•	•	•
85	0.085	2.16	7.65	194.31	48.58	29.85	97.16	59.71	194.31	119.42	•	•	•	•
90	0.090	2.29	8.10	205.74	51.44	31.61	102.87	63.22	205.74	126.44	•	•	•	•
95	0.095	2.41	8.55	217.17	54.29	33.37	108.59	66.73	217.17	133.47	•	•	•	•

Figure 2.11 : R.D.Specialties wire-wound rod sizes and expected film thicknesses.

temperature. ( $\sim 70^{\circ}\text{C}$  for nitric acid,  $\sim 120^{\circ}\text{C}$  for oleum) Inside the heated oven, the acid is expected to evaporate and diffuse into the SWNT film network. After 30 mins, the top glass plate was removed quickly from petri dish, the oven was closed and the vacuum was turned on. The vacuum line purged most of the acid vapors, which were collected in an acid trap hooked on to the vacuum line. Subsequently, the glass slides with SWNT films were collected, quenched and dried in the same manner as mentioned above.

## Chapter 3

# Nematic-like Alignment in SWNT Thin Films from Aqueous Colloidal Suspensions

### 3.1 Introduction

Despite nearly two decades of intense research, the extraordinary properties of individual carbon nanotubes (CNTs) [Odom *et al.* 1998, Tans *et al.* 1997] have not been attained in macrostructures [Behabtu *et al.* 2008, Dan *et al.* 2009]. Specifically, electrical properties are limited by junction resistance, due to a combination of CNT misalignment and mismatch in electronic band structure in the case of single-walled carbon nanotubes (SWNTs) of different chirality [Bachilo *et al.* 2002]. Likewise, mechanical properties are limited by incomplete alignment and poor packing due to polydisperse CNT diameters. Pint *et al.* [2009] found that, in an aligned SWNT film, conductivity along the direction of alignment is two orders of magnitude higher than that in the orthogonal direction. Likewise, the modulus of SWNT fibers drops tenfold as the degree of alignment among constituent SWNTs is degraded [Liu and Kumar 2003]. In terms of mismatch in electronic band structure, Fuhrer *et al.* [2000]

---

Part of this chapter has been submitted to Journal of Materials Chemistry (2011)

showed that junction resistance between a metallic type and semiconducting SWNT is typically 100-fold higher than between SWNTs with similar band structure. In SWNT macrostructures, these high resistance junctions become bottlenecks for electron transport, leading to poor bulk conductivity. A new technique is needed to fabricate highly ordered thin films of SWNTs sorted by electronic type or enriched by chirality.

Ordered transparent, conductive SWNT thin films are desirable for applications including electronic displays, touch screens, O-LEDs and photovoltaics. Recent reports show that SWNTs act as anchoring agents for liquid crystals [Basu and Iannacchione 2009, Park *et al.* 2007, Russell *et al.* 2006, van der Schoot *et al.* 2008]. Fu *et al.* [2010] demonstrated a prototype liquid crystal display where a highly aligned SWNT film serves both as transparent conductive layer and liquid crystal aligning layer, thereby eliminating one layer (e.g., polyimide) and LCD processing steps. Ordered SWNT thin films can also template the large scale assembly and orientational ordering of anisotropic plasmonic nanoparticles [Dan *et al.* 2011, submitted]. Such macroscopic ordered assemblies of nanoparticles on conductive substrate are valuable for optical metamaterials and photovoltaics [Atwater and Polman 2010, Shalaev 2007].

In general, aligned CNT films and fibers can be fabricated by dry and wet methods. In dry methods, aligned arrays of CNTs grown by chemical vapor deposition

(CVD) are “dry processed” into thin films and fibers while preserving the pre-existing alignment [Pint *et al.* 2010, Zhang *et al.* 2005]. In wet methods, orientational order is achieved by forming a nematic liquid crystalline phase in appropriate solvents such as superacids for pristine, high-quality CNTs [Davis *et al.* 2009, Green *et al.* 2009], or water for CNTs, that have been oxidized or stabilized by biomolecules [Badaire *et al.* 2005, Moulton *et al.* 2007, Song *et al.* 2003]. This yields well aligned wet spun macroscopic fibers of pristine nanotubes [Behabtu *et al.* 2008, Davis *et al.* 2009, Ericson *et al.* 2004]. Ordered films ( $\sim 30 \mu\text{m}$  thick) of oxidized CNTs by vacuum filtration [Shaffer *et al.* 1998] or by evaporation of solvent [Shimoda *et al.* 2002] have also been reported.

The current techniques for creating aligned films and fibers have limitations. Despite recent advances in CNT synthesis [Harutyunyan *et al.* 2009], growth of single-chirality SWNTs at significant scales has not been achieved yet, limiting the use of dry methods to produce single-chirality aligned SWNT films. For wet methods, the creation of a nematic phase requires high concentration and hence large amount ( $\sim 0.1 \text{ g}$  or more) of CNTs; in contrast, the most effective sorting and enrichment techniques, such as density gradient ultracentrifugation (DGU) [Arnold *et al.* 2006, Haroz *et al.* 2010] and dielectrophoresis (DEP) [Krupke *et al.* 2003], yield only tens of micrograms.

## 3.2 Slow Filtration Technique

Here, we present a versatile and yet simple technique for fabricating SWNT thin films with high local order. The technique is based on vacuum filtration of SWNT-surfactant colloidal suspensions (Fig. 3.1). The filtration rate is the critical parameter that controls whether the film is ordered or disordered.

To study the effect of filtration rate on the film nanostructure, SWNT-SDBS dispersions were filtered through two PCTE filter membranes with different pore sizes: namely 200 nm (filtration rate  $\sim 1$  ml/min) and 30 nm (filtration rate  $\sim 2$  ml/hr). Upon completion of filtration and 30 min drying under vacuum suction, the retentate on the filter was washed with de-ionized water-ethanol mixture (50:50 v/v) to remove residual surfactant and subsequently dried in a vacuum oven for 2 hour at 80°C. Dissolution of the filter membrane with N-methyl-2-pyrrolidone produced free floating SWNT films which transferred onto silicon substrates. SEM images of the resulting films, Fig. 3.2(a) and (b) respectively, clearly show that “fast filtration” leads to a random SWNT network, similar to the pioneering work of Rinzler’s group [Wu *et al.* 2004], whereas “slow filtration” produces local nematic ordering among SWNTs.

### 3.2.1 Exploring the Role of Surfactants

To explore for any role of surfactants on the ordering, films were fabricated from SWNT dispersions prepared using surfactants with different ionic structures: cetyltrimethy-

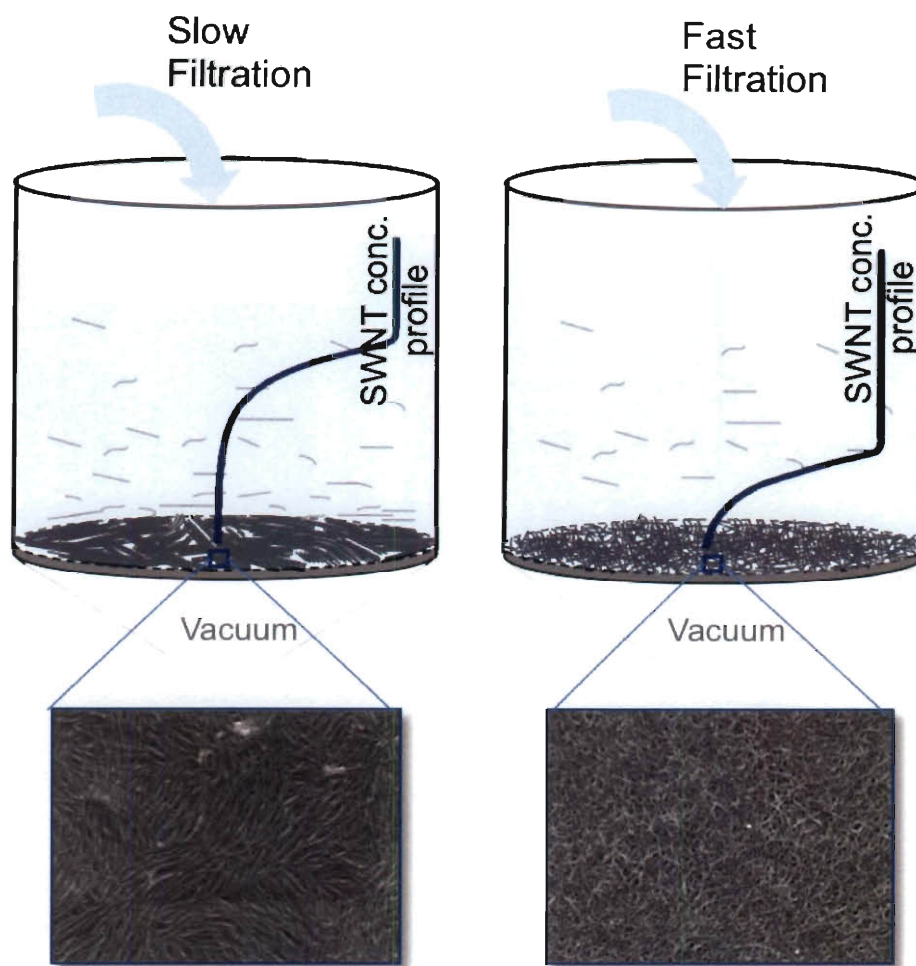


Figure 3.1 : Schematic of differences between slow (2 ml/hr.) and fast (1 ml/min) vacuum filtration. Slow filtration leads to 30 times thicker “high SWNT concentration region”, shown by “SWNT conc. profile” plots (log-log scale), and longer SWNT “residence time” than fast filtration. Orientational ordering of SWNTs in this region leads to formation of nematic like ordered thin films, as opposed to random network films.

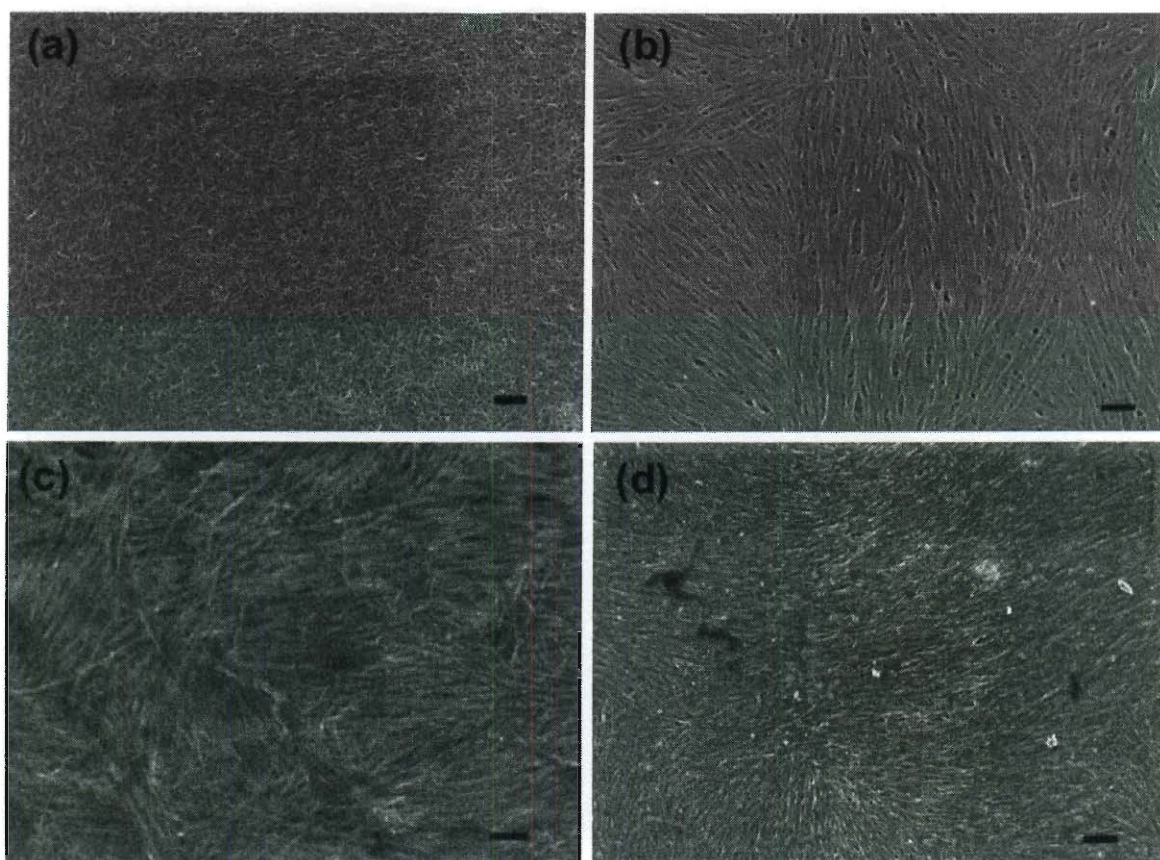


Figure 3.2 : SEM images of SWNT thin films: (a) random SWNT network in “fast filtration” film from SDBS dispersion. (b) nematic like ordering in “slow filtration” film produced from same SDBS dispersion. (c) and (d) show nematic like ordering in slow filtration films produced from CTAB and Pluronic F87 dispersions. The scale bar in each image is 200 nm.



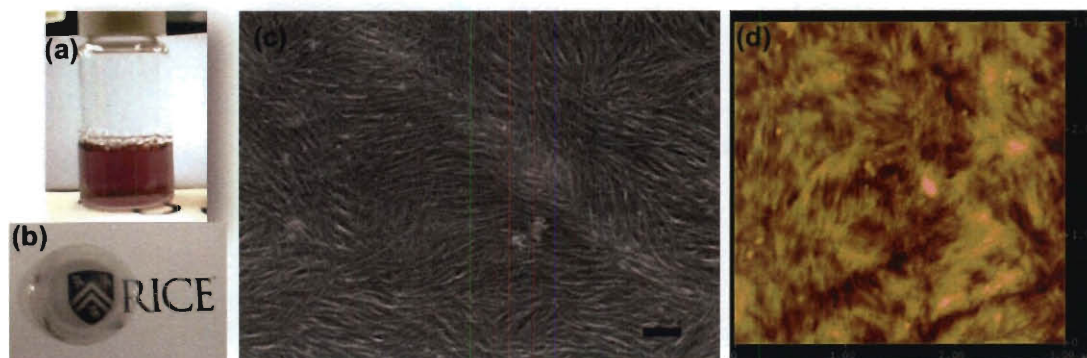


Figure 3.3 : (a) Metallic enriched SWNT suspension obtained from DGU process, (b) SWNT thin film fabricated via “slow filtration”. SEM and AFM images (c and d) show the nematic-like ordering of SWNTs in the film. Scale bar in (c) is 200 nm. AFM image is  $3 \mu\text{m} \times 3 \mu\text{m}$ .

lammonium bromide (CTAB, cationic) and Pluronic F87 (non-ionic). The SEM images in Fig. 3.2(c)-(d) show the similar nematic-like ordering observed in these cases as well. The slow filtration technique was applied to a SWNT dispersion enriched in metallic SWNTs prepared using DGU [Haroz *et al.* 2010] and used in its as-produced form, containing multiple surfactants and iodixanol - the density gradient medium. Further characterizations of the DGU SWNT dispersion are provided in the appendix. Figure 3.3(a - d) shows the metallic enriched SWNT dispersion and ensuing film with local nematic ordering. Interestingly, all slowly filtered films show ordering irrespective of type, quantity, and combination of surfactants used.

In addition to surfactant type and filtration rate, concentration of SWNTs is another parameter of interest. The highest achievable individualized SWNT concen-

tration in each of our SWNT-surfactant dispersions remained within a narrow range (30-60 mg/l) [Duque *et al.* 2010]. The effect of CNT concentration on filtered film microstructure was studied by Shaffer *et al.* [1998]. Their studies on oxidized CNT aqueous dispersions showed that a low CNT concentration (dilute regime) was important to achieve ordering. Higher concentrations lead to CNT entanglement and low rotational diffusivity, likely preventing orientational ordering during film formation and resulting in random network films.

### 3.3 Analysis of Alignment in SWNT Films

Further analysis of nematic ordering in SWNT films were performed using the scalar order parameter,  $S$ , which quantifies degree of alignment among individual molecules with respect to an average direction of orientation  $n$ , known as director. The 2-D scalar order parameter is [Shaffer *et al.* 1998]:

$$S_{2D} = 2 \langle \cos^2 \alpha \rangle - 1 \quad (3.1)$$

where  $\alpha$  is the angle between molecular axis and  $n$ , and angular brackets denote an ensemble average over the orientational distribution function (ODF). Analysis of SEM images was performed using ImageJ coupled with ‘‘OrientationJ’’ plugin [Fonck *et al.* 2009]. Figure 3.4(b) depicts the microstructure of a SWNT-SDBS nematic-like

Table 3.1 : Average 2-D scalar order parameter ( $S_{2D}$ ) for a random network SWNT film from fast filtration and nematic like ordered SWNT films prepared by slow filtration of different SWNT surfactant dispersions (listed in the first column), along with average square cell sizes used for calculation. For the random network film a series of square cells with sides ranging from 200-2500 nm were used.

Film Type	$S_{2D}$	Average Domain Size (nm)
SDBS suspension	$0.82 \pm 0.05$	$1338 \pm 157$
F87 suspension	$0.76 \pm 0.05$	$653 \pm 56$
CTAB suspension	$0.71 \pm 0.05$	$797 \pm 101$
Metallic enriched	$0.77 \pm 0.09$	$661 \pm 110$
Isotropic (SDBS)	$0.24 \pm 0.04$	-

film (Fig. 3.4(a)), consisting of adjoining “domains” of aligned SWNTs, highlighted by different false colors. Largest fitting square cells, denoting areas of uniform SWNT alignment were selected from these domains (Fig. 3.4(c)) and analyzed to obtain an ODF for SWNTs (Fig. 3.4(d)). The angle corresponding to intensity maxima is taken as director ( $\alpha = 0$ ) and the ODF is used to calculate an ensemble average of  $\cos^2 \alpha$  which gives  $S_{2D}$  according to Eq. 3.1. As the SEM cannot resolve individual SWNTs, they are assumed to be aligned axially within each bundle, i.e.,  $S_{2D, \text{bundle}} \approx S_{2D, \text{SWNT}}$ .  $S_{2D}$  values of numerous cells from multiple SEM images were averaged to determine an average  $S_{2D}$  for each film, listed in Table 5.1 along with the typical cell sizes. For the isotropic film, average  $S_{2D}$  was calculated from a series of cell sizes ranging from 200 to 2500 nm; hence no particular cell size is reported. The significantly higher  $S_{2D}$  of “slow filtration” nematic like films can be readily observed.

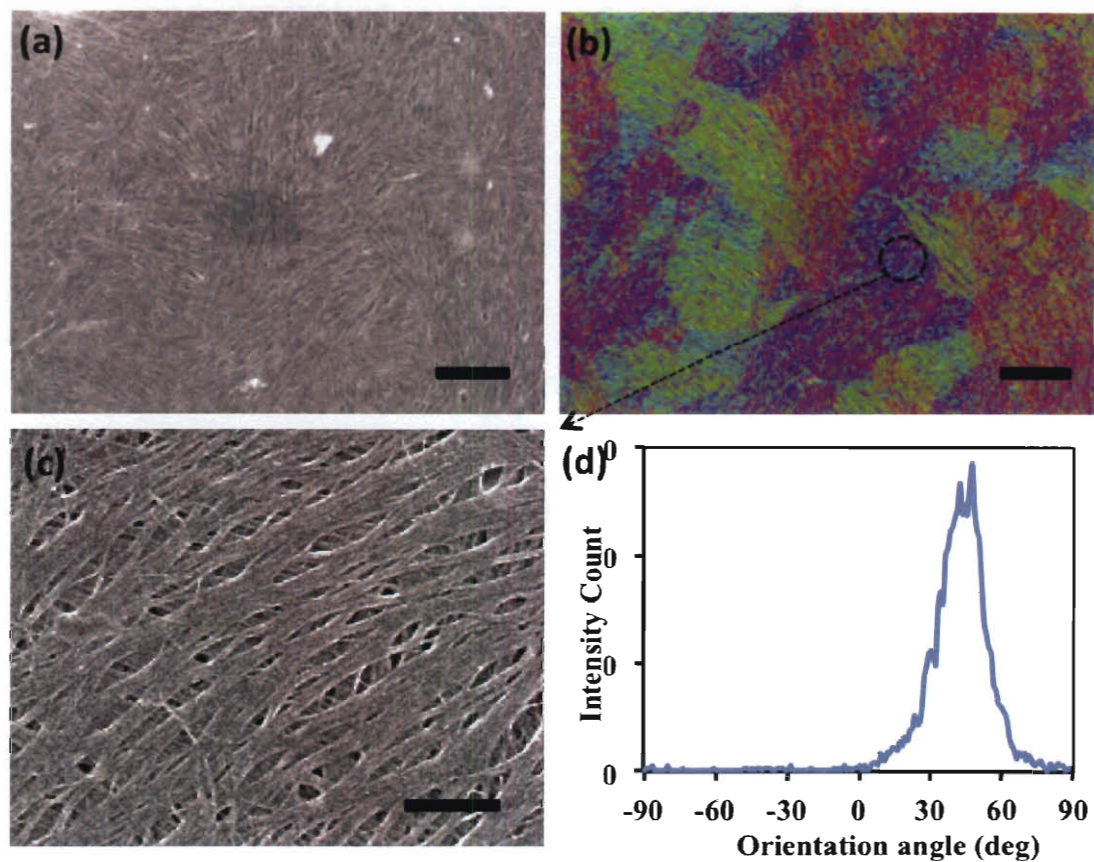


Figure 3.4 : (a) Nematic like ordered SWNT film from SDBS suspension (scale bar  $1 \mu\text{m}$ ). (b) “Domains” of aligned SWNTs, detected automatically by “OrientationJ” plugin in imageJ software.(scale bar  $1 \mu\text{m}$ ) (c) Aligned SWNTs within a single cell, (d) Orientation distribution of SWNTs in image (c). (scale bar  $250 \text{ nm}$ ) Orientation distribution was used to calculate a 2D scalar order parameter ( $S_{2D}$ ) for SWNTs.  $S_{2D} \sim 0.87$  for image (c).

### 3.4 Electro-optical Characterization

SWNT thin films were also characterized for electro-optical properties. Under cross-polarized light microscopy, the films did not show any distinguishable birefringence, probably due to small size of domains compared to optical resolution. The bulk conductivity of films was measured using 4-point probe. (Jandel Microposition Probe with cylindrical probe head, probe spacing 1 mm). Both locally ordered and disordered films showed similar properties (300-350  $\Omega/\text{sq}$  for 65-70% transmission at 550 nm wavelength) - probably because the measurement length scale was much larger than the size of the ordered domains (hundreds of nm).

### 3.5 SWNT Nematic Ordering Mechanism

The local nematic like ordering of SWNTs is clearly caused by the slow filtration process. As the solvent is removed by filtration, a concentration gradient develops in the filtration funnel; SWNTs increasingly concentrate near the filter membrane. Once the SWNT concentration in this “high concentration region” exceeds the isotropic-nematic transition point, SWNTs begin to align spontaneously. The slow filtration rate affects the above process in two ways: first, it yields a less steep concentration gradient and hence a thicker high concentration region; the characteristic thickness of this region is  $\delta_{\text{conc}} \propto \frac{D}{v_f}$ , where  $D$  is the translational diffusivity of SWNTs and  $v_f$  is

average fluid velocity (function of filtration speed). Second, SWNTs move slower and therefore have sufficient time to reorient into locally ordered domains while traversing the high-concentration region before depositing on the filter membrane.

We estimated the SWNT concentration profile in liquid dispersion inside the filtration funnel during filtration process. The steady equation of continuity can be expressed as,  $v_f \cdot \nabla c = D \nabla^2 c$ , where  $c$  is SWNT mass fraction and is a function of distance from filter ( $z$ ). The fluid velocity  $v_f$ , obtained from filtration rate, was assumed to be constant. Assuming uniform flow across the filtration membrane, the above equation was solved in one dimension to obtain the SWNT concentration profile:  $c(z) = (C_0 - C_b)e^{-\frac{v_f \cdot z}{D}} + C_b$ , where  $C_0$  is SWNT concentration at the surface of filter (or developing SWNT film) and  $C_b$  is the initial SWNT concentration in dispersion. SWNT concentration profiles for fast and slow filtration cases are depicted in Fig. 3.1, shown in log-log scale to highlight the high concentration region. The high concentration region for slow filtration was typically  $\sim 30$  times thicker than for fast filtration (few microns).

The time required for SWNTs to travel from a region with  $c \sim c_{\text{biphasic}}$  (i.e.,  $z_{\text{biphasic}}$ ) to the filter membrane ( $z = 0$ ) can be defined as the ‘residence time’ ( $t_{\text{res}}$ ) of SWNTs in the high concentration region. and can be computed as :  $t_{\text{res}} = \int_{z_{\text{biphasic}}}^{z=0} \frac{1}{v_{\text{swnt}}} dz$ , where  $z_{\text{biphasic}}$  denotes  $z$  where  $c \sim c_{\text{biphasic}}$ .  $c_{\text{biphasic}}$  is the concentration marking the onset of biphasic region for a lyotropic system; for HiPco SWNTs,

assuming non-interacting rods,  $c_{\text{biphasic}} \sim 4000$  ppm [Green *et al.* 2009, Wensink and Vroege 2003]; attractive interactions would lower this threshold.  $z_{\text{biphasic}}$  was calculated from the SWNT concentration profile and SWNT velocity can be defined as:  $v_{\text{swnt}} = \frac{1}{c}(v_f - D\nabla c)$ . For slow filtration  $t_{\text{res}} \sim \text{O}(1 \text{ s})$  whereas for fast filtration  $t_{\text{res}} \sim \text{O}(1 \text{ ms})$ . In dilute SWNT dispersions, SWNTs have a rotational diffusivity  $D_R \sim 250 \text{ s}^{-1}$  [Duggal and Pasquali 2006], giving a characteristic time scale of  $\tau \sim \text{O}(1 \text{ ms})$ . Intuitively, residence times shorter than this characteristic time make reorientation and alignment of SWNTs very unlikely, before immobilizing into a film.

Previous studies [Bradac *et al.* 2002, Chen *et al.* 2008] (on thermotropic LCs) have shown that isotropic to nematic phase transitions typically involve three stages: (a) nucleation: independent nucleation of multiple ordered domains, with no correlation between directors of different domains, (b) domain growth: a period of domain size growth, typically following the dynamical scaling law  $r_d \approx t^{0.5}$ , where  $r_d$  is domain diameter and  $t$  is time, (c) Late stage: healing of domain boundaries and dynamics of LC defects. The staggered domain structure of nematic-like SWNT films suggests that SWNT ordering during slow filtration likely follows similar developmental pathway but lacks a “late stage”, likely due to consolidation of SWNTs into a solid (or gel-like) film. SWNT films with larger domain sizes can potentially be obtained by increasing the residence time, i.e., reducing further the filtration rate, or by varying SWNT length.

## 3.6 Conclusions

We presented a simple technique for fabricating SWNT thin films with local nematic-like ordering. This technique is applicable to a number of aqueous SWNT suspensions, irrespective of type, quantity, and combination of surfactants present as well as metallic enriched SWNT dispersion as-produced by DGU. Scalar order parameter calculations show a high degree of local ordering among SWNTs in the film. These ordered films of pristine SWNTs can serve as useful functional materials and a platform for development of metamaterials, electrodes, and transparent conductive coatings with ordered SWNTs.

## 3.7 Appendix

### 3.7.1 Density Gradient Ultracentrifugation

Density gradient ultracentrifugation (DGU) was performed on several different SWNT materials, described in H  roz et al. [2010] using Rice-produced, HiPco batch HPR188.2. Upon completion of a DGU run, 250  $\mu\text{L}$  fractions were extracted from each centrifuge tube, starting at the top of the metal DGU band. The material from multiple runs was combined to form a total of 6 ml for each fraction. ‘Fraction 5’

---

Metallic-type enriched SWNT obtained by density gradient ultracentrifugation was prepared and characterized by Erik Haroz from Prof. J. Kono’s research group.



was used here for this study with an estimated metallic nanotube purity of 91% by integrated absorption area.

The optical absorption spectra (Shimadzu UV-3101PC scanning spectrophotometer) of the starting SWNT surfactant suspension and DGU enriched “Fraction 5” material, for film as well as liquid samples, are shown in Fig. 3.5. A 1% (wt/vol) DOC (water) reference was used for the as-produced liquid sample. The reference for the metal-enriched liquid sample was produced by running a DGU run without nanotubes to approximate the mixture of surfactants and density gradient medium present in the enriched fraction.

Raman scattering spectra (Renishaw inVia Raman microscope) of films fabricated from the starting SWNT suspension and metallic enriched DGU material are shown in Fig. 3.6.

### **3.7.2 Preparation of SWNT Dispersions**

The detailed procedure for SWNT dispersion preparation is reported in O’Connell et al. [2001]. The basic steps are outlined below:

1. Mix 1 wt% of desired surfactant in 200 ml of nanopure water, in a glass vial. Stir or bath sonicate till surfactant dissolves completely.(solution becomes ‘clear’)
2. Mix  $\sim$  200 mg purified HiPco SWNT in the surfactant-water solution.

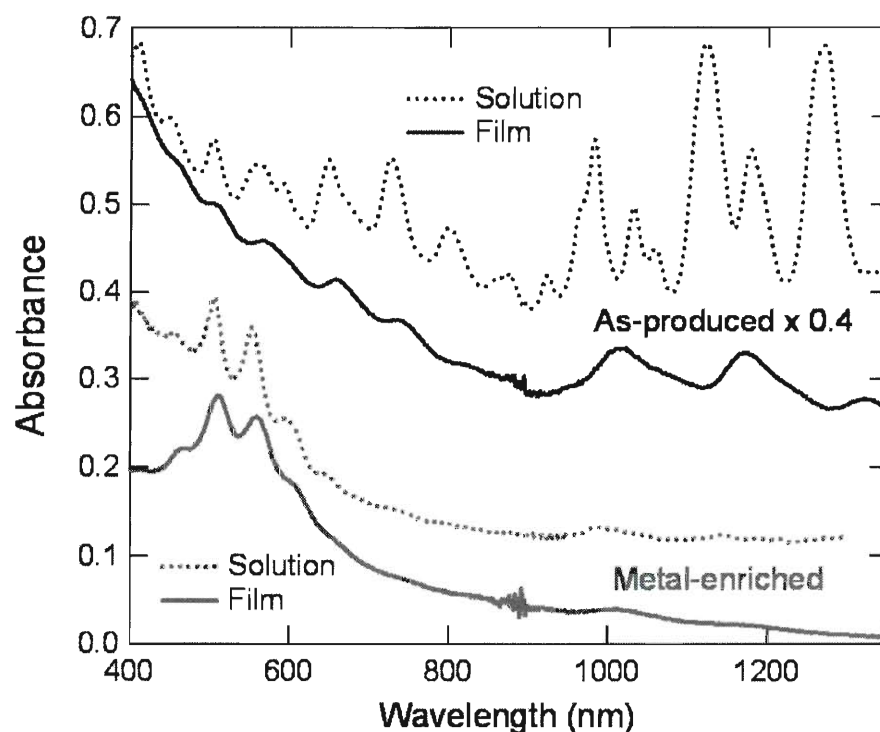


Figure 3.5 : Optical absorption spectra of as-produced material (SWNT surfactant suspension) and metallic enriched SWNT suspension obtained through DGU. Red solid (dotted) traces are for metallic-enriched SWNT film (solution), and black solid (dotted) traces are for as-produced material film (solution) multiplied by 0.4. Traces are vertically offset for clarity. Note the enrichment of metallic peaks in the DGU material versus the as-produced material and the relatively strong, well-defined metallic features that remain after film formation, as compared to the semiconductor features which show significant broadening and red-shifting.

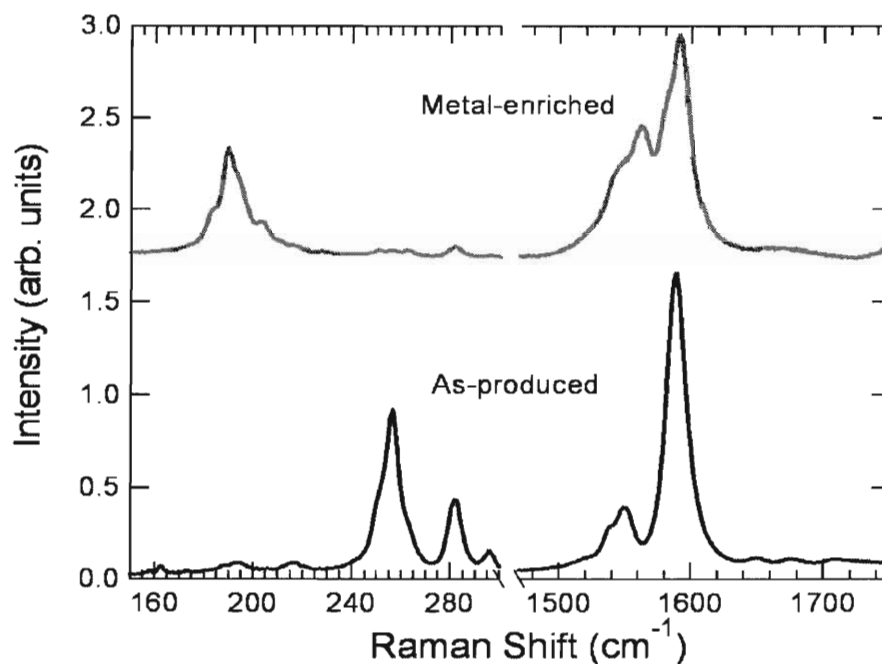


Figure 3.6 : Raman scattering spectra of films fabricated from starting SWNT suspension and metallic enriched DGU material, performed at 633 nm excitation wavelength. The spectra indicate the strong enrichment of radial breathing mode features ( $100\text{-}300\text{ cm}^{-1}$ ) corresponding to metallic chiralities of nanotubes in the metal-enriched sample as well as the characteristically broad, metallic G-band lineshape ( $1500\text{-}1600\text{ cm}^{-1}$ ).

3. Homogenize the mixture using a high shear homogenizer (for example, Fisher Scientific Catalog No. 14-261-04), at  $\sim 8000$  rpm for 45 mins. The head of the stator should be slightly lower than the mid-point of liquid column in the vial.
4. Sonicate the homogenized mixture by pouring into a cup-horn sonicator, and sonicating at 90% amplitude for 10 mins. This process usually leads to strong heating of the suspension. Transfer the suspension back into the vial and place in cold water or ice bath.
5. Centrifuge the sonicated suspension at 29,000 rpm for 4 hours. Collect the top 75% of liquid from each centrifuge tube using a pipette, without shaking the centrifuge tubes.

The above procedure typically produces what is often referred to as “SWNT-surfactant decant” with SWNT concentration on the order of 10-100 mg/L. The suspension is expected to have mostly individual SWNTs and some small diameter bundles ( $< 20$  nm diameter). The result of the procedure is dependent on the surfactant used and its efficacy in SWNT suspension. SDBS, Pluronic F87, CTAB, DOC are highly recommended.

### 3.7.3 Slow Vacuum Filtration

Vacuum filtration was performed using the lab vacuum line and a standard micro-filtration setup (Fisher Scientific) with 25 mm diameter glass frit filter membrane holder and Poly Carbonate Track Etched (PCTE) filter membranes. Each SWNT film was prepared by filtering 1.5 - 2 ml of the desired SWNT dispersion (30-60 mg/L conc.), keeping the filtration funnel covered with water saturated tissue to minimize solvent evaporation. The vacuum suction through filtration setup was allowed to run for at least 15 mins after the end of filtration (by visible inspection) to ensure complete consolidation of the SWNT film. About 8 - 10 ml of DI water was added in the filtration setup by gently pouring through the sides of the filtration funnel, and filtered through the PCTE-SWNT film membrane already in place, for removal of surfactant. Upon completion of water filtration, the filter-SWNT film membrane was recovered from the filtration setup and allowed to dry at room temperature ( $\sim 30$  mins). For detachment of the filter membrane, the 'dry' filter-SWNT film membrane was entirely dunked inside a N-Methyl-2-pyrrolidone (NMP) bath. The filter-SWNT film membrane typically has a tendency to float on the NMP free surface; it is important that the entire film is pulled (or dunked) inside the solvent to ensure complete and uniform wetting from all sides, and avoid stretching and cracking in SWNT film, as the PCTE gradually softens and dissolves away ( $\sim 30$  mins). The free SWNT film can then be recovered on to any substrate of interest by slipping the substrate

under the floating SWNT film and lifting it out. The residual NMP can be either evaporated or washed away with acetone/IPA. A final round of vacuum oven drying is recommended for the SWNT film.

#### **3.7.4 Analysis of SWNT Alignment in Nematic Films**

The microstructure of slow filtered SWNT films was found to be “locally nematic” ordered, consisting of adjoining “domains” or regions of uniform and unidirectional SWNT alignment with almost no correlation between direction of alignment in neighboring domains. The degree of alignment among SWNTs inside each domain was characterized using free image analysis software ImageJ and a plugin OrientationJ, developed by the Biomedical Imaging Group (BIG) at École Polytechnique Fédérale de Lausanne (EPFL). The plugin and basic usage instructions can be found at <http://bigwww.epfl.ch/demo/orientation/> .

The plugin was used to obtain an orientation distribution function, with 180 data points (angles), for SWNTs in a domain. The intensity at each point can be understood as the number of SWNTs aligned along that ‘angle’. The ‘angle’ of maximum intensity was taken as the director ( $\alpha=0$ ); i.e., the numerical value of this angle was subtracted from all angles, setting this as zero and re-defining all other angles, relative to this new axis.  $\text{Intensity} \cdot \cos^2 \alpha$  was calculated for each of the 180 data points, and their sum was normalized by dividing with the sum total of only

intensities; this represents  $\langle \cos^2 \alpha \rangle$ , i.e., the ensemble average.

## Chapter 4

# Aligned SWNT Ribbons and Flakes from Superacid Solutions

### 4.1 Introduction

Superacids are currently the only solvents capable of athermally *dissolving* SWNTs [Davis *et al.* 2009, Parra-Vasquez *et al.* 2010]. This is in contrast to water and other organic solvents (like isopropanol, N-Methyl-2-pyrrolidone) which *disperse* SWNTs as colloidal particles. A superacid is an acid stronger than 100% sulfuric acid. Previous studies [Davis *et al.* 2009, Zhou *et al.* 2005] have shown that superacid anions intercalate SWNT bundles and protonate the SWNTs, forming charge transfer complexes consisting of positively charged individual SWNTs surrounded by negatively charged acid anions (Fig. 4.1(a)). The resulting electrostatic repulsion leads to spontaneous individualization and stable dissolution of SWNTs, confirmed by cryo-TEM imaging (Fig. 4.1).

The main advantages of using superacids for liquid phase SWNT processing include:

- Spontaneous dissolution by stirring. SWNTs dissolve in superacids without



need of high-power sonication or chemical functionalization. Both these processes, required for colloidal dispersion in water or organic solvents, are known to cause SWNT “cutting” and structural damage.

- Capable of dissolving long SWNTs. (hundreds of microns) In contrast, colloidal dispersion in water and organic solvents is typically limited to SWNTs with length of up to a few microns only.
- High SWNT loadings achievable. ( $> 10$  wt% or two orders of magnitude higher than colloidal dispersions)

#### 4.1.1 SWNT-Superacid Phase Behavior

Due to the rod-like structure of SWNTs, SWNT-superacid solutions form lyotropic systems offering rich phase behavior and characteristic phase transitions predicted by Onsager [1949]. The phase diagram of HiPco SWNTs (average length  $\sim 500$  nm) in superacids of varying strengths is shown in Fig. 4.2.

At dilute concentrations (few parts per million) the solutions are isotropic. As the SWNT concentration increases above  $\sim 4000$  ppm the solution transitions to an ordered state. Due to polydispersity in the length of SWNTs, this ordered state is biphasic where liquid crystalline domains of SWNTs co-exist with the isotropic SWNT solution. Complete single-phase liquid crystallinity is achieved at much higher

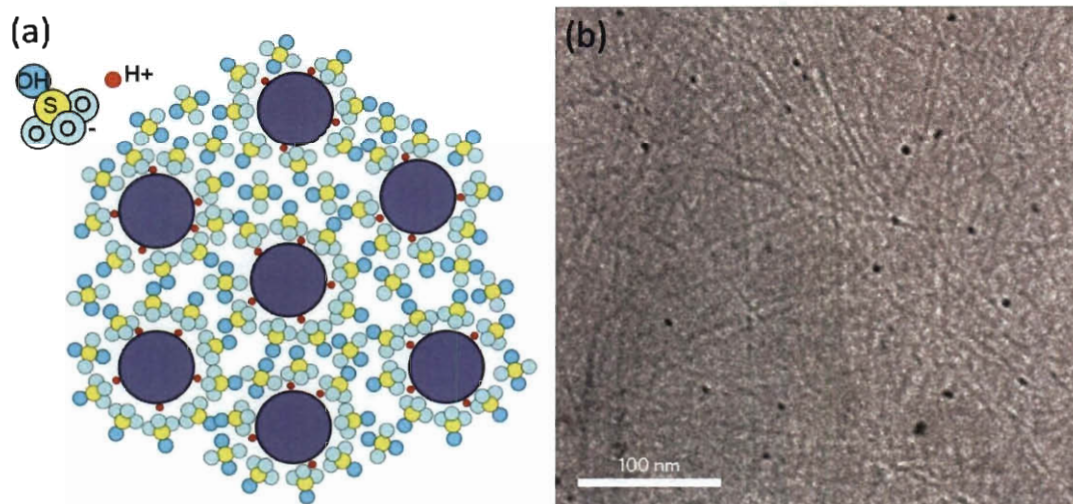


Figure 4.1 : (a) Schematic: intercalation of sulfuric acid anions in SWNT bundles. Acid anions protonate SWNTs forming charge-transfer complexes and resulting in debundling and dissolution of SWNTs. (b) Cryo-TEM image of HiPco SWNTs (0.134 vol%) dissolved in  $\text{ClSO}_3\text{H}$ . (Images re-produced from [Ericson *et al.* 2004](a), [Davis *et al.* 2009](b), without permission.)

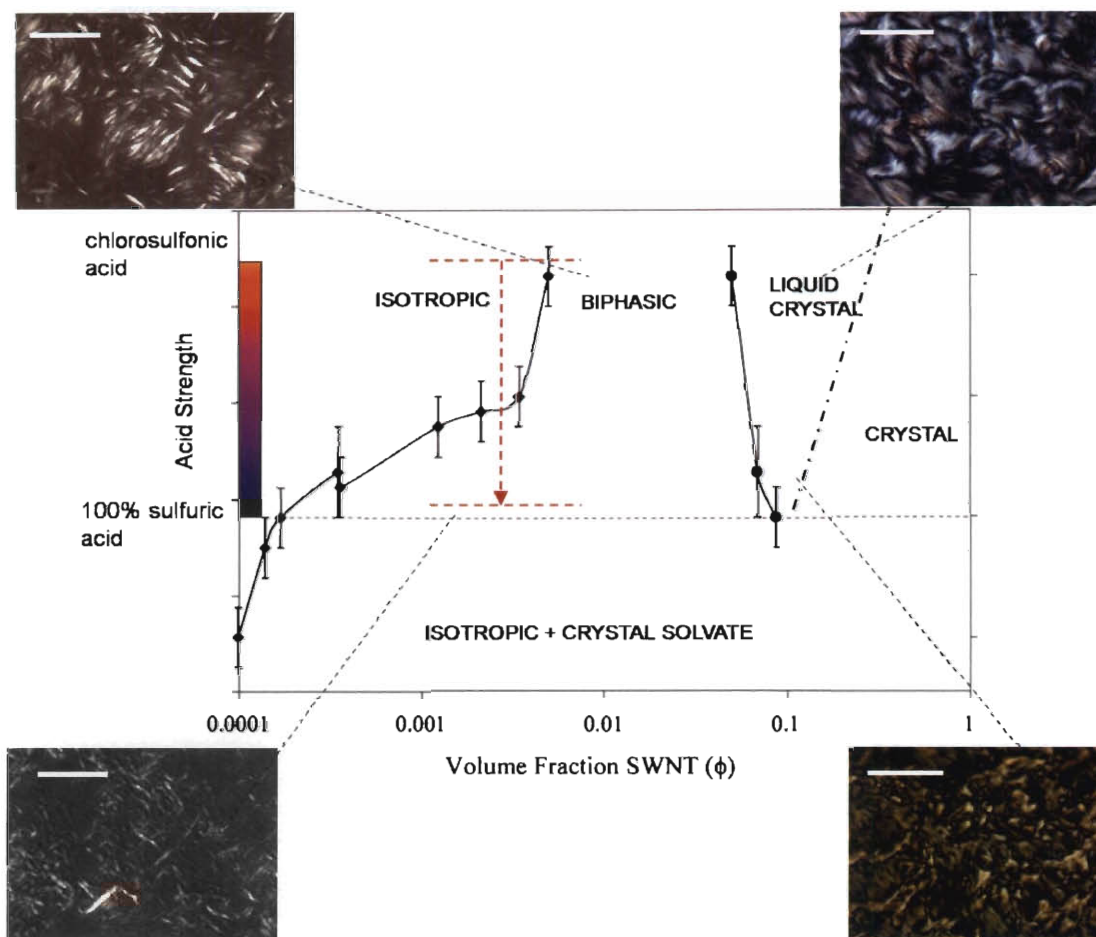


Figure 4.2 : Phase diagram of HiPco SWNTs in superacids (center) and cross-polarized light micrographs (corners) showing effect of solvent strength on SWNT microstructure at different SWNT concentrations. Light microscopy images, from top-left and going clockwise: 1.21 vol% in  $\text{ClSO}_3\text{H}$  (scale:  $50 \mu\text{m}$ ), 12.1 vol% in  $\text{ClSO}_3\text{H}$  (scale:  $20 \mu\text{m}$ ), 10.6 vol% in 120%  $\text{H}_2\text{SO}_4$  (scale:  $20 \mu\text{m}$ ), 0.132 vol% in 120%  $\text{H}_2\text{SO}_4$  (scale:  $20 \mu\text{m}$ ). The red dotted arrow represents the phase trajectory and crossing of phase boundary, driving the formation of aligned SWNT macrostructures. Part of image reproduced from [Davis *et al.* 2009] without permission.

concentrations of  $\sim 70000$  ppm (7 wt%). The specific concentrations at which a solution undergoes phase transition depends on the average length of SWNTs as well as the details of inter-SWNT interactions [Green *et al.* 2009]. Reduction in acid strength (reduced stabilizing power of solvent against attractive van der Waals forces between SWNTs) pushes the phase boundary to lower concentrations, as can be seen in Fig. 4.2.

#### 4.1.2 Novel Fabrication Method for 2-D Aligned SWNT Macrostructures

The spontaneous ordering of SWNTs in high concentration lyotropic solutions has been used for fabricating macroscopic fibers (diameter  $\sim 10$ - $100$   $\mu\text{m}$ ) of highly aligned pristine SWNTs. Fabrication of aligned SWNT thin films (hundreds of nanometers) and 2-D macrostructures has, however, remained elusive; the high concentration of SWNTs in liquid crystalline solutions makes thin film fabrication challenging and impractical using currently existing methods. In this chapter, we present a novel technique for fabricating macroscopic 2-D flakes and flat ribbons of aligned SWNTs from SWNT-superacid solutions. We induced phase transition and achieved SWNT ordering in *low concentration* SWNT-superacid solutions by slowly reducing solvent quality (acid strength) through controlled exposure to moisture. The ordered SWNT domains in solution were extracted as SWNT macrostructures by precipitation. The phase trajectory driving the SWNT macrostructure fabrication is depicted by a dot-

ted line in Fig. 4.2. Characterization using polarizing optical microscopy and Raman spectroscopy revealed that most macrostructures were optically transparent (thin) and consisted of highly aligned SWNTs; the 2-D nature of these SWNT macrostructures likely stems from the low concentration of SWNTs in the starting solution.

## 4.2 Experimental Methods

### 4.2.1 SWNT-Superacid Solution Preparation

SWNT-superacid solutions were prepared by adding purified and dried HiPco SWNTs in chlorosulfonic acid, followed by gentle swirling, stirring using magnetic stir bar, or mild bath sonication (< 5 minutes). The entire process was carried out inside a glove-box purged with dry air.

### 4.2.2 SWNT Macrostructure Fabrication Procedure

The experimental setup and procedure are shown schematically in Fig. 4.3. In a typical experiment, 0.5 - 1.0 ml of SWNT-superacid solution (200-4000 ppm) in a teflon capped dry glass vial was placed inside a glove bag purged with dry  $N_2$ . A measured volume of water (quenching solvent) was introduced in the glove bag and the teflon cap of SWNT-superacid containing vial was removed; the water molecules evaporate and diffuse into the superacid solution, reducing the acid strength. The amount of water introduced into the glove bag corresponded to that required for

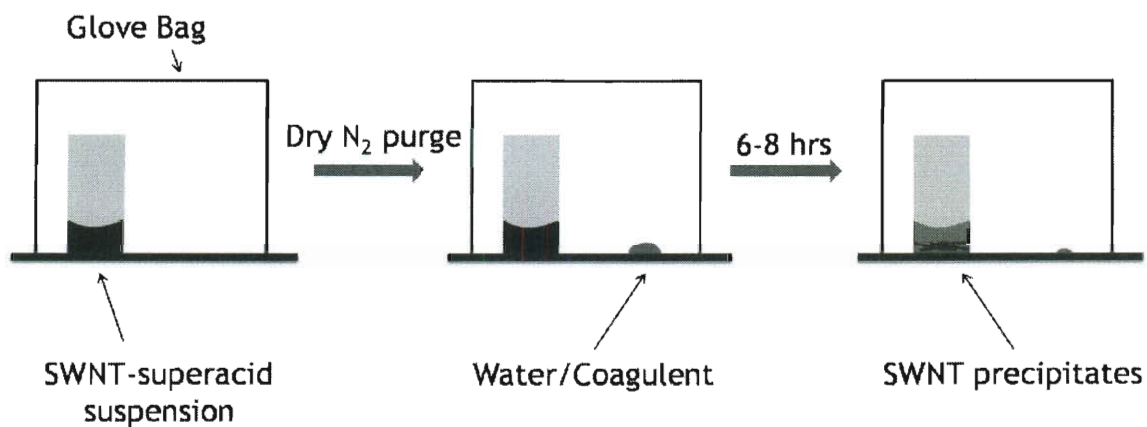


Figure 4.3 : Experimental setup used for fabrication of aligned SWNT macrostructures. Small quantity of pre-mixed SWNT-ClSO<sub>3</sub>H solution in a sealed vial, was kept inside a glove bag purged with dry N<sub>2</sub>. A measured amount of water (quenching solvent) was introduced in the glove bag and the SWNT-superacid solution vial was unsealed. Over 6-8 hours, water molecules evaporate and diffuse into the solution, slowly reducing the acid strength and resulting in precipitation of highly aligned SWNT macrostructures.

converting chlorosulfonic acid into  $\sim 70\%$  sulfuric acid according to the chemical reaction formula:  $\text{HSO}_3\text{Cl} + \text{H}_2\text{O} \rightarrow \text{H}_2\text{SO}_4 + \text{HCl}$ . Drop in acid strength below 100% sulfuric acid typically led to precipitation of SWNT macrostructures.

Upon completion of experiment, the precipitated SWNT flakes and ribbons were collected on glass or silicon substrates, washed with water and annealed for  $\approx 1$  hour at 200°C under vacuum, before characterization.

## 4.3 Results & Discussion

### 4.3.1 Optical Microscopy

SWNT macrostructures were fabricated starting from SWNT solutions of various concentrations. The resulting macrostructures were analyzed for shape and size, optical transparency, and SWNT alignment using polarizing optical microscopy.

The optical micrographs of SWNT macrostructures formed by slow quenching of a 200 ppm SWNT-chlorosulfonic acid solution are shown in Fig. 4.4. Most structures were in the shape of flat ribbons or 2-D flakes with typical dimensions on the order of  $\sim 100 \mu\text{m}$ . Optically “transparent” appearance under bright field transmission mode microscopy indicated that the SWNT macrostructures were  $\approx 50 - 200 \text{ nm}$  in thickness (based on similar transparencies and thicknesses encountered with transparent conductive thin films, see Chapter 2). Strong optical birefringence, observed between crossed-polarizers, demonstrated a high degree of SWNT alignment in these 2-D SWNT macrostructures.

SWNT macrostructures produced from 1000 ppm and 4000 ppm SWNT-chlorosulfonic acid solutions are shown in Fig. 4.5 and Fig. 4.6, respectively. Structures obtained from 4000 ppm SWNT-chlorosulfonic acid solution were observed to be typically darker (higher opacity) under transmission mode microscopy indicating their higher thicknesses, see Fig. 4.6(a). This is likely due to the higher SWNT concentration in

starting solution; it underscores the importance of having a low SWNT concentration in solution for fabrication of thin films and 2-D structures, as opposed to high concentrations used for fiber spinning.

### 4.3.2 Raman Spectroscopy

Polarized Raman spectroscopy (Renishaw inVia Raman microscope) was used to probe the degree of SWNT alignment in these macrostructures. The optical image of a SWNT ribbon fabricated from 1000 ppm SWNT-chlorosulfonic acid solution is shown in Fig. 4.7(a). Strong birefringence observed under crossed-polarizers indicates significant alignment of SWNTs in the ribbon. The Raman spectra (785 nm excitation laser) with laser polarization parallel and perpendicular to the ribbon longitudinal axis were collected at three different spots along the SWNT ribbon; the averaged spectra are shown in Fig. 4.7(c). The Raman G-peak signal ( $\sim 1591 \text{ cm}^{-1}$ ) for parallel laser orientation was four times stronger than that for perpendicular laser orientation, confirming high degree of SWNT alignment, see Fig. 4.7(c)-inset.

## 4.4 Conclusions

A novel route for fabrication of highly aligned 2-D SWNT macrostructures from SWNT-superacid solutions is presented. Orientational ordering was achieved in low concentration SWNT-superacid solutions by inducing phase transitions via reduction



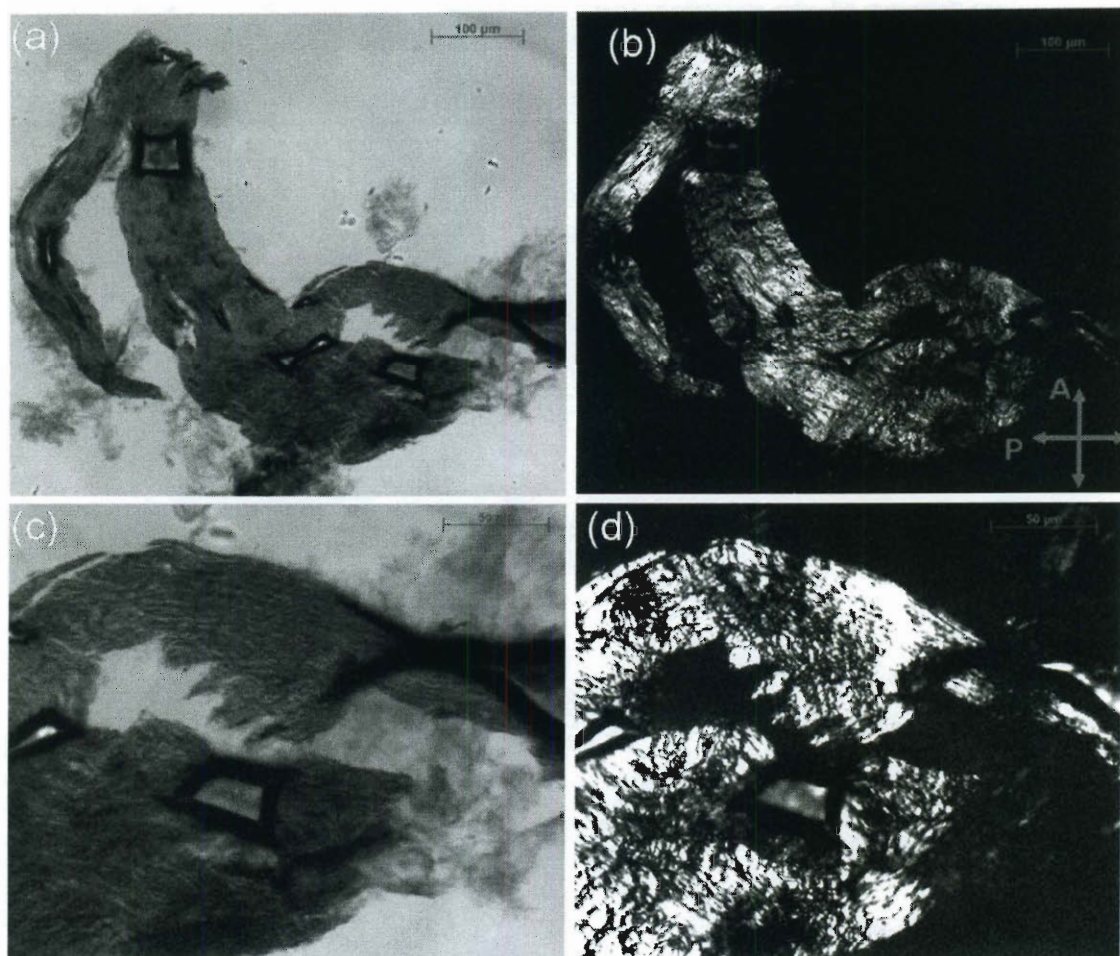


Figure 4.4 : Optical micrographs of aligned SWNT macrostructures, under transmission mode (a,c) and crossed-polarizers (b,d). Crossed red arrows indicate polarizer and analyzer orientations. The macrostructures were prepared by slow quenching of 200 ppm SWNT-ClSO<sub>3</sub>H solution with water, inside a glove bag. Scale bars: 100 μm for (a-b), 50 μm for (c-d).

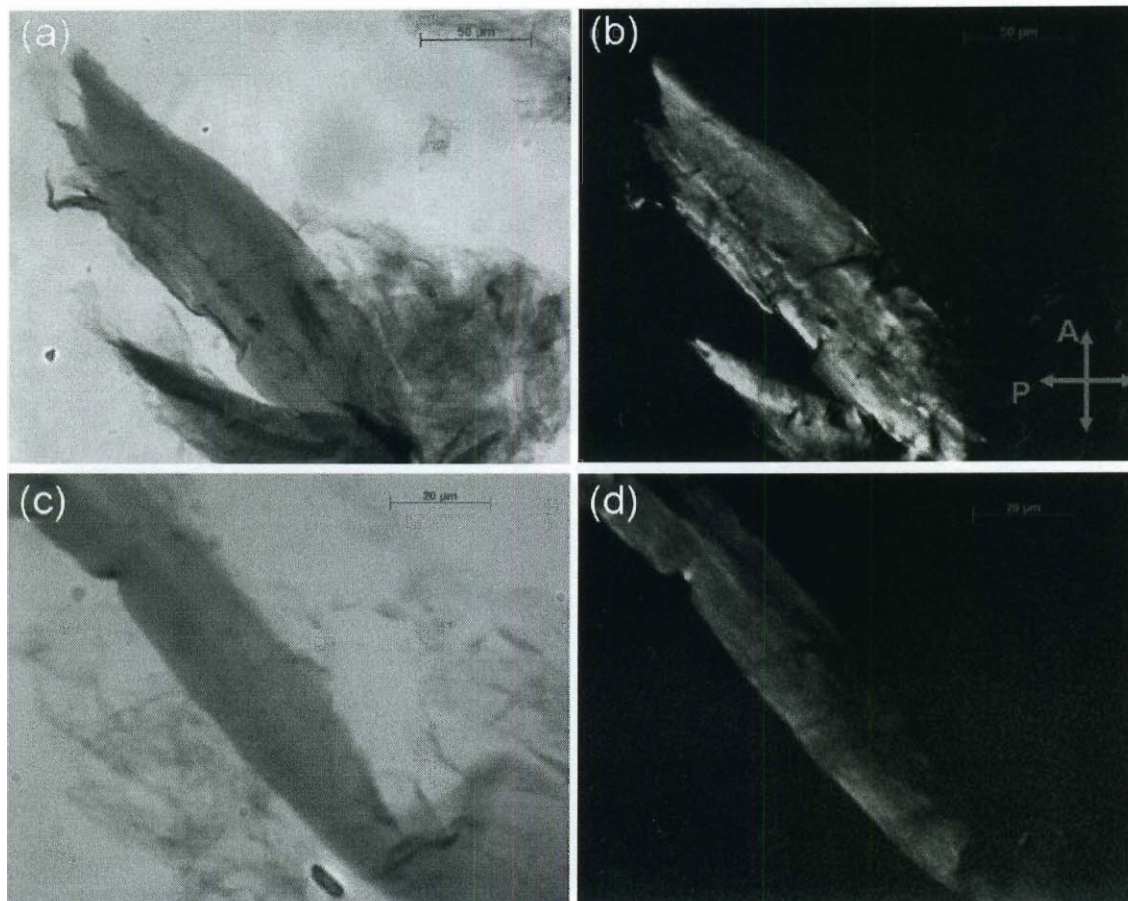


Figure 4.5 : Optical micrographs of aligned SWNT macrostructures, under transmission mode (a,c) and crossed-polarizers (b,d). Crossed red arrows indicate polarizer and analyzer orientations. The macrostructures were prepared by slow quenching of 1000 ppm SWNT-ClSO<sub>3</sub>H solution with water, inside a glove bag. Scale bars: 50 μm for (a-b), 20 μm for (c-d).

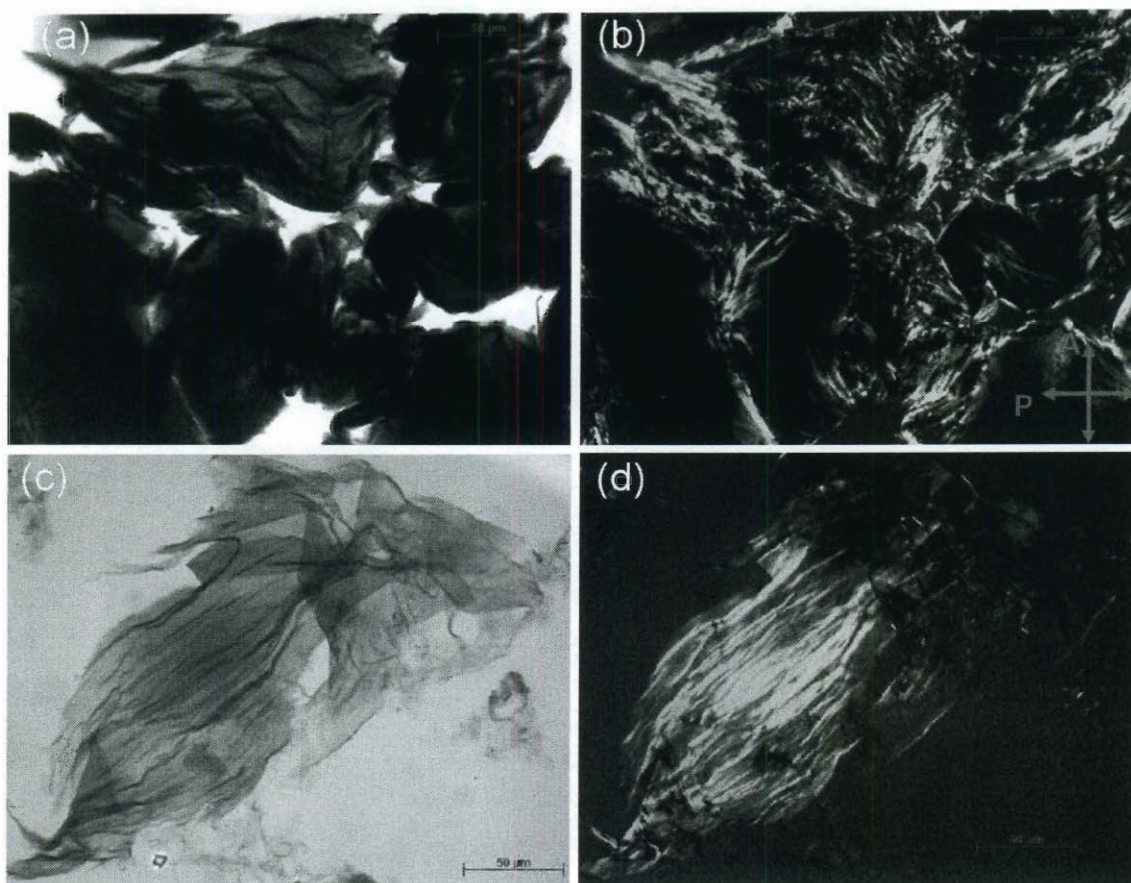


Figure 4.6 : Optical micrographs of aligned SWNT macrostructures, under transmission mode (a,c) and crossed-polarizers (b,d). Crossed red arrows indicate polarizer and analyzer orientations. The macrostructures were prepared by slow quenching of 4000 ppm SWNT-ClSO<sub>3</sub>H solution with water, inside a glove bag. Scale bars: 50 μm for all images.

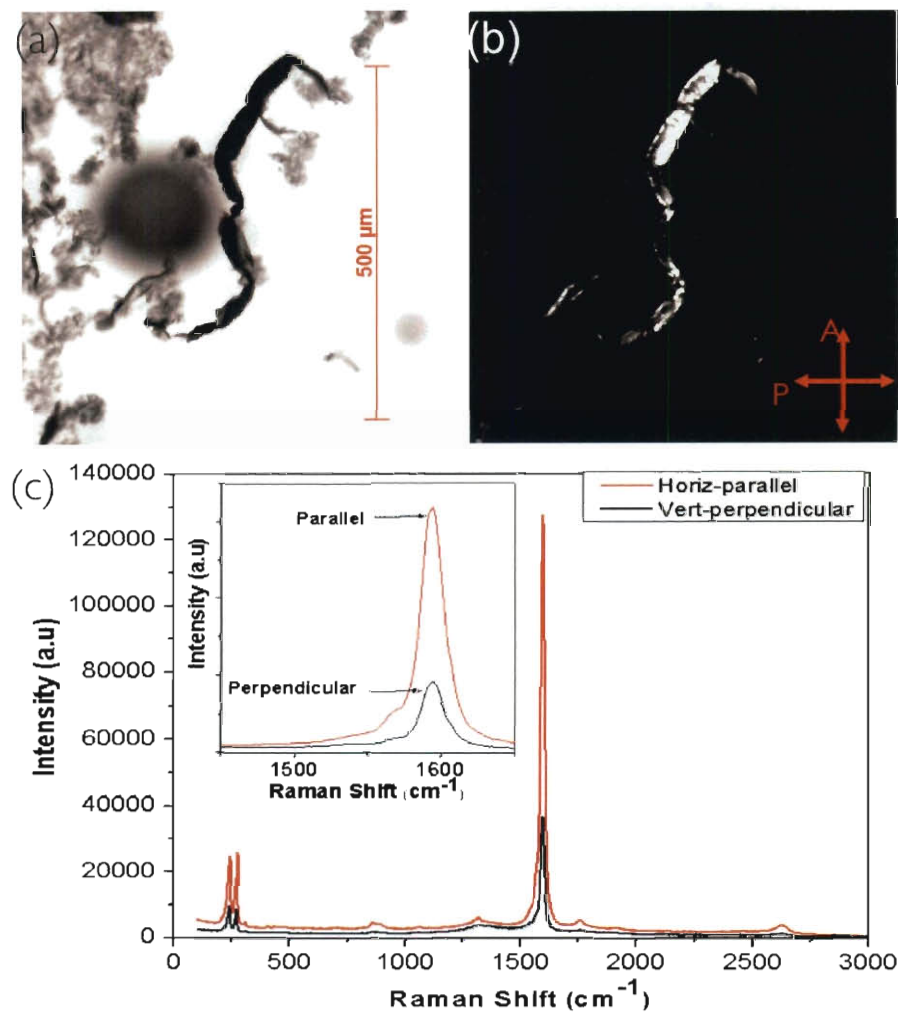


Figure 4.7 : Optical micrograph of a ribbon like macrostructure from 1000 ppm SWNT-ClSO<sub>3</sub>H solution, under transmission mode (a) and crossed-polarizers (b). (c) Raman spectra with 785 nm excitation laser, polarized parallel to and perpendicular to the ribbon longitudinal axis. Parallel orientation generated four times stronger G-peak ( $\sim 1591 \text{ cm}^{-1}$ ) signal, compared to perpendicular orientation, indicating high degree of SWNT alignment in the ribbon. (Inset: magnified G-peak spectra.)

in solvent quality. The ordered SWNT phases were precipitated as aligned SWNT macrostructures by further reduction of solvent acidity (below 100 % sulfuric acid). Bright field transmission mode optical microscopy revealed that typical structures were hundreds of microns in dimension and optically semi-transparent (hundreds of nanometers in thickness). Polarized Raman spectroscopy showed a G-peak ratio of  $\sim 4$ , indicating significant SWNT alignment.

## 4.5 Appendix

### 4.5.1 Fabrication of Aligned Macrostructures from Metallic-type Enriched SWNTs

Currently, there is strong interest in fabrication of aligned SWNT structures from metallic-type enriched SWNT material. The techniques capable of separating SWNTs according to electronic type, however, have low yields which make fabrication of macrostructures, especially aligned macrostructures, challenging. For example, density gradient ultracentrifugation(DGU) [Arnold *et al.* 2006, Haroz *et al.* 2010] typically produces 10 ml of metallic-type enriched SWNT suspension with  $\sim 20$  ppm concentration; equivalently, 300  $\mu\text{g}$  of metallic enriched SWNT material.

The SWNT-superacid based macrostructure fabrication procedure has minimal SWNT material requirements and can be an ideal route for achieving the above goal.

For example, only  $\sim 30 \mu\text{g}$  SWNT is required to prepare  $100 \mu\text{l}$  of 200 ppm SWNT-superacid solution, which is enough to carry out the procedure and produce aligned SWNT macrostructures.

## Chapter 5

# Spontaneous Templating of Anisotropic Gold Nanoparticles on Ordered SWNT Macrostructures

### 5.1 Introduction

Metallic nanoparticles have been the subject of intense research owing to their unusual electro-optical properties and a vast array of potential applications [Daniel and Astruc 2004, Murphy *et al.* 2005]. Current research towards nanoparticles for metamaterial applications is primarily focused in two directions: synthesis and ordered assembly. Synthesis involves designing new methods for fabrication of nanoparticles from a variety of materials, with varied anisotropic shapes, sizes and aspect ratios. Particles are being tailored to possess highly tunable plasmonic and optoelectronic properties aimed for specific advanced applications. Ordered assembly entails deposition of nanoparticles on surfaces, incorporation into bulk liquid crystalline media, or chemically mediated crystallization in an organized manner. In this way, the unique properties of individual nanoparticles can be leveraged collectively to attain func-

---

Part of this chapter has been submitted to ACS nano, (2011). Part of this work was performed at Dept. of Physics and Liquid Crystal Materials Research Center, University of Colorado, Boulder, with Prof. Ivan Smalyukh.

tional behavior on macroscopic scales. Gold nanorods (GNRs) are a particularly interesting class of nanoparticles because their transverse and longitudinal surface Plasmon resonance (SPR) depend on polarization and can be easily tuned across the visible and near IR spectrum by changing the GNR aspect ratio [Link *et al.* 1999]. Promising GNR applications include photovoltaics [Atwater and Polman 2010, Morfa *et al.* 2008, Westphalen *et al.* 2000], surface enhanced Raman scattering (SERS) based detection and imaging [Nikoobakht and El-Sayed 2003, Orendorff *et al.* 2006], biological imaging and therapy [Durr *et al.* 2007, Huang *et al.* 2006; 2007], and optical metamaterials [Liu *et al.* 2010, Shalaev *et al.* 2005]; large scale ordered assembly of GNRs is a critical step for the development of many of these applications.

Recent advances in ordered assembly and nanoscale alignment of GNRs include incorporation into lyotropic liquid crystals [Liu *et al.* 2010], stretched polymer films [Murphy and Orendorff 2005, Shenhar *et al.* 2005], electric field driven alignment in liquid medium [van der Zande *et al.* 1999], colloid based self-assembly [Jana *et al.* 2002, Nikoobakht *et al.* 2000], and deposition onto patterned surfaces [Liu *et al.* 2006]. In most cases, however, the substrates or surrounding material (for bulk incorporation) possess minimal or no functionality; the lack of essential properties like electrical conductivity, mechanical strength, or chemical durability often limits the range of possible applications for these hybrid materials.

Single-walled carbon nanotubes (SWNTs) offer a promising alternative in this



context. SWNTs offer the functional and structural features of high performance polymers [Green *et al.* 2009], coupled with superior electro-optical properties and chemical inertness [Tans *et al.* 1997]. Their nanoscale diameter combined with high aspect ratio ( $> 1000$ ) makes them ideal candidates for forming high performance thin films [Dan *et al.* 2009, Wu *et al.* 2004] and fibers [Behabtu *et al.* 2008, Davis *et al.* 2009, Li *et al.* 2004] which in turn serve as basic functional materials for a host of engineering applications, devices and materials. For example, SWNT thin films are being developed as transparent conductive coatings for touch screens, flat electronic displays, OLEDs, electrodes for solar cells, etc. [Hu *et al.* 2010]. High specific surface area,  $\approx 1300 \text{ m}^2/\text{g}$  [Peigney *et al.* 2001], makes SWNT macrostructures highly desirable substrates for hosting other functional nanoparticles, for example, SWNT based supports for catalyst nanoparticles, SWNT electrodes for fuel cells [Girishkumar *et al.* 2004, Planeix *et al.* 1994], and oriented attachment of GNRs on sidewalls of individual polymer coated MWNTs [Correa-Duarte *et al.* 2005]. In this article, we report the spontaneous ordered templating of plasmonic GNRs on various highly aligned SWNT macrostructures. The superior electro-optical properties of SWNTs coupled with optical properties of plasmonic nanoparticles make SWNT-GNR composites potential candidates for a number of optoelectronic applications.

## 5.2 Materials and Methods

### 5.2.1 Fabrication of Gold Nanorods and Microparticles

GNRs with medium ( $\sim 5$ -12) and high aspect ratios, ( $\sim 12$ -35) were fabricated using standard seed mediated growth in the presence of CTAB (Cetyl trimethylammonium bromide) [Jana *et al.* 2002, Murphy *et al.* 2005, Nikoobakht *et al.* 2000]. Briefly, spherical gold seeds were produced by reducing chloroauric acid with sodium borohydride in the presence of CTAB. Next, three identical growth solutions were prepared with chloroauric acid, CTAB, and ascorbic acid.

To produce medium length GNRs, the seed was added to the first solution and the reaction was allowed to take place progressively in each growth solution for a couple of hours, followed by pipette transfer to the next growth solution. To produce long rods, the reaction was allowed to proceed in the first two growth solutions for less than a minute and then left in the third solution overnight. In both cases, the final product was obtained in the form of a precipitate consisting of CTAB capped GNRs. The GNRs were recovered and re-dispersed to form dilute aqueous suspensions (1 mg/ml). Short GNRs (aspect ratio  $\sim 2$ -4) were directly purchased from Nanopartz Inc.

High aspect ratio, polydisperse gold triangles and polygonal platelets with up to 10  $\mu\text{m}$  side lengths and 5 nm thickness were produced using an aloe vera extract

mediated technique: 30 g of aloe vera leaf were boiled in 100 ml of de-ionized water to produce the extract, 1 ml of the extract was then added to 1 mM chloroauric acid in 9 ml of methanol and allowed to sit at room temperature for several days [Chandran *et al.* 2006].

### 5.2.2 Fabrication of Aligned SWNT Macrostructures

Thin films of horizontally aligned SWNTs were prepared from vertically aligned SWNT “carpets” produced using the method described by Xu *et al.* [Xu *et al.* 2006]. These carpets typically consisted of 20-200  $\mu\text{m}$  long vertical array of SWNTs bound to Fe catalyst particles and supported on Silicon substrates, as shown in Fig. 5.1(a). Thin films were obtained from the SWNT carpets using a modified version of the “roll-over” method [Pint *et al.* 2008]. Briefly, vertically aligned SWNTs were “tilted” towards the desired direction of alignment by gentle unidirectional rubbing with a clean strip of velvet cloth, followed by the “rolling” process which compresses the carpet into a dense, highly aligned SWNT film (Fig. 5.1(b)). A thin sheet of aluminum foil was used during rolling to prevent transfer of any SWNTs from the carpet on to the roller. Dipping these SWNT films in 1 M HCl solution etches away the catalyst particles, resulting in their immediate detachment from Silicon substrates; the free floating films can then be transferred onto any desired substrate.

SWNT fibers were produced by wet spinning from high concentration ( $> 8$  wt

%) SWNT-Oleum (100 % sulfuric acid + 20 % SO<sub>3</sub>) solutions [Booker *et al.* 2008, Davis *et al.* 2009, Ericson *et al.* 2004, Wang *et al.* 2005]. Under polarized Raman spectroscopy, the fiber showed a G-peak ( $\sim 1591 \text{ cm}^{-1}$ ) intensity ratio (longitudinal vs. transverse directions) of 2.4, indicating a high degree of SWNT alignment, further confirmed by SEM (Fig. 5.2(a)).

### 5.2.3 Gold Nanorod Deposition Procedure

The GNR deposition process consisted of drop drying GNR colloidal suspensions (few microliters) on top of the SWNT macrostructures. Upon completion of drying under ambient conditions, the samples were further heated to  $\sim 90^\circ\text{C}$  for 5 minutes to ensure complete removal of the solvent. The desired density of GNRs on SWNT films and fibers was achieved by repeating the drop drying procedure multiple times. GNRs with a wide range of aspect ratios ( $\sim 2\text{-}35$ ) were deposited on SWNT films using this procedure. The GNR deposition and assembly on SWNT fibers was tested only with short GNR samples.

## 5.3 Results

The GNR-SWNT composites were analyzed using SEM imaging (JEOL JSM-7401F FESEM). Remarkably, we found that a large fraction of GNRs spontaneously align along the SWNTs in the films and fibers during the deposition process, as shown

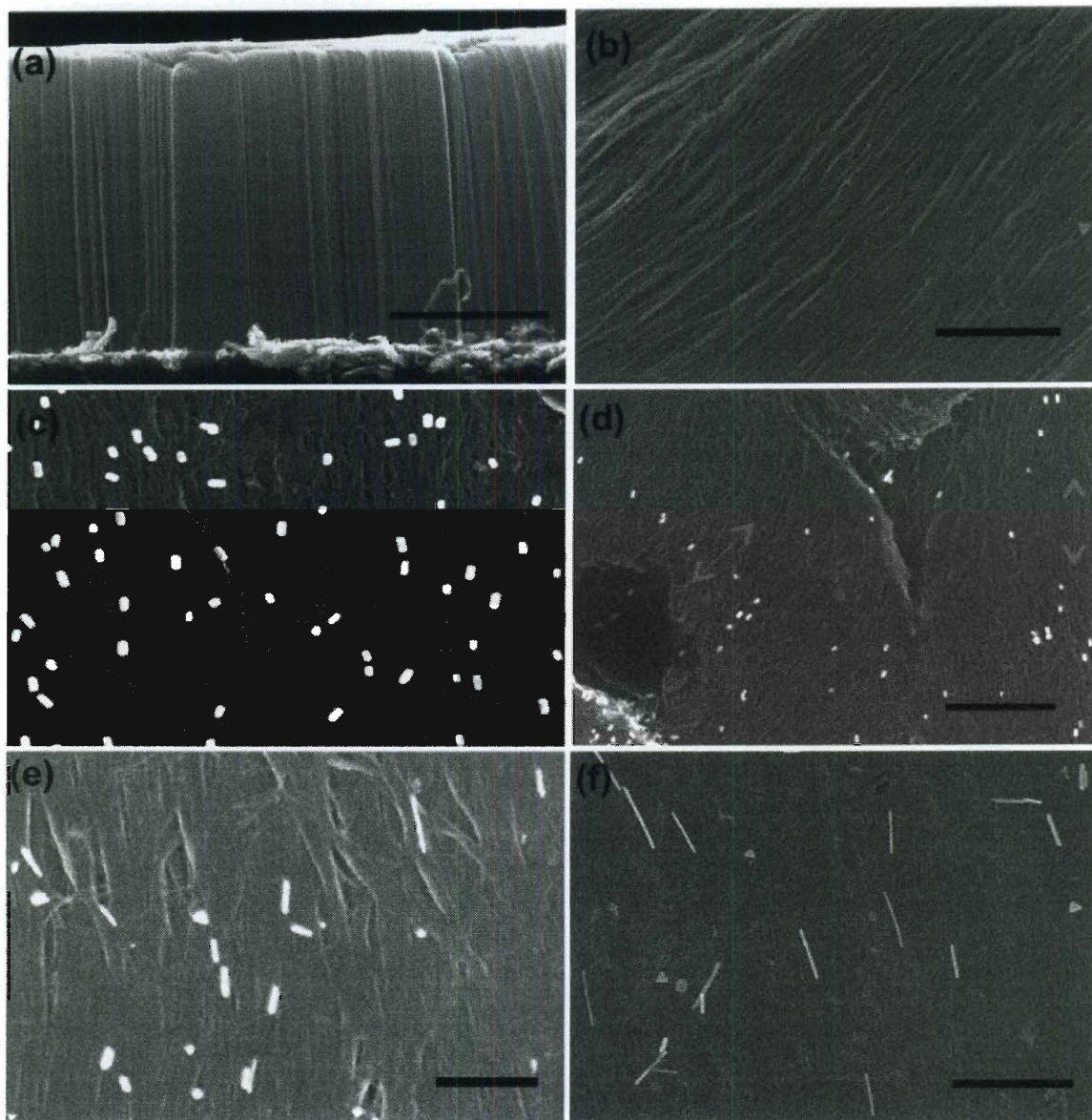


Figure 5.1 : SEM images showing macroscopic ordered assemblies of gold nanorods (GNRs), of varying aspect ratios, produced by drop drying GNR suspensions on aligned SWNT films. (a) Vertically aligned SWNT carpet, (b) aligned SWNT film fabricated from SWNT carpet, (c) Spontaneous alignment of short GNRs (aspect ratio 2-4) on SWNT film, (d) GNRs replicating the alignment defect (shown with red arrows) in underlying film, (e) and (f) Alignment of medium (5-12) and long (12-35) aspect ratio GNRs with SWNTs. Scale bars: (a)  $15\ \mu\text{m}$ , (b)  $1\ \mu\text{m}$ , (c)  $400\ \text{nm}$ , (d)  $1\ \mu\text{m}$ , (e)  $500\ \text{nm}$ , (f)  $1\ \mu\text{m}$ .

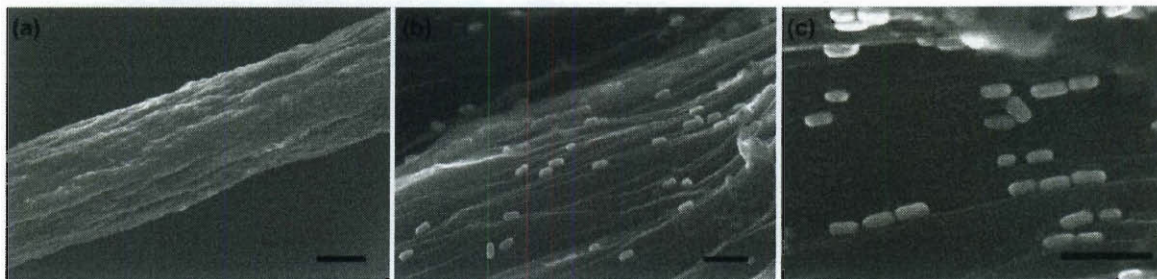


Figure 5.2 : SEM image of SWNT fiber (a) and spontaneous alignment of short GNRs with SWNTs (b-c) in the fiber. GNRs were deposited onto the fiber by drop drying as well as dip coating, both methods producing similar results. Scale bars: (a) 40  $\mu\text{m}$ , (b) and (c) 200 nm.

in Figs. 5.1(c - f) and Figs. 5.2(b - c). In addition, the strong spontaneous alignment to the SWNT substrate was observed for all GNR aspect ratios. Most of the non-aligned GNRs were within rare aggregates. Non-uniformities (cracks, sharp protrusions, misaligned domains and domain boundaries, etc.) in the underlying SWNT macrostructure promoted aggregation and accumulation of GNRs, often leading to their non-uniform distribution. Employing dilute GNR suspensions limited the extent of GNR aggregation during drop drying and yielded an ordered and oriented GNR deposition. Closer inspection of regions in GNR-SWNT thin films with imperfect alignment, like in Fig. 5.1(d), reveal that GNRs also follow defect and distortion patterns in their underlying SWNTs, providing further insights into the origins of the observed oriented assembly.

### 5.3.1 Orientation Distribution Function for Gold Nanorods

GNR alignment on SWNT macrostructures was quantified by measuring the angular orientation of individual GNRs with respect to the aligned SWNTs in the SEM images. Multiple SEM images were analyzed for each GNR type (short, medium and long) to collect data for statistically significant number of GNRs. For example, a total of 322 short GNR particles were analyzed for SWNT films and 97 particles for short GNRs on SWNT fibers. It is important to note that SWNTs in the films and fibers used for our experiments possess good alignment over large length scales (microns and higher), but show considerable waviness and undulations at shorter length scales (tens of nanometers). Consequently, an array of GNRs deposited on these films and fibers can appear less ordered at large length scales, in spite of a high degree of alignment between individual GNRs and the local, immediately underlying SWNT/SWNT bundle; this of course is a shortcoming of substrate quality rather than the alignment procedure. In order to obtain a true estimate for the degree of alignment of GNRs with SWNTs, the angular orientation of individual GNRs (defined as  $\alpha$ ) were measured with respect to the direction of alignment of the locally underlying or nearest observable SWNTs ( $\alpha=0$ ). Figure 5.3 shows the normalized orientation distribution function obtained for short GNRs deposited on aligned SWNT carpet films and SWNT fibers. Higher aspect ratio GNRs deposited on SWNT films showed a similar angular distribution.

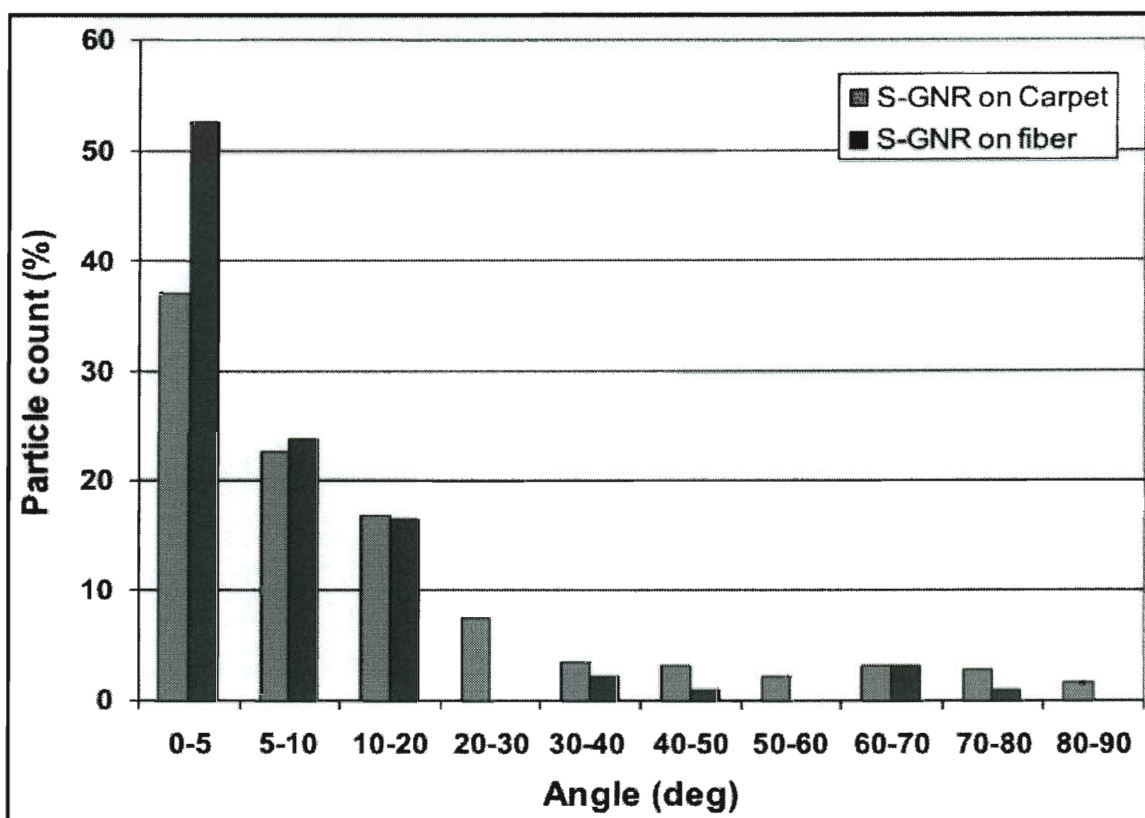


Figure 5.3 : Orientational distribution function for spontaneously aligned short GNRs on aligned SWNT macrostructures. Orientation angle for each GNR was calculated with respect to the underlying SWNT/SWNT bundle. Total of 322 particles were analyzed for S-GNRs on SWNT carpets, and 97 particles were analyzed for S-GNRs on SWNT fibers.



### 5.3.2 Scalar Order Parameter for Gold Nanorod Arrays

The angular orientation measurements for individual GNR particles were used to calculate the 2-D scalar order parameter ( $S_{2D}$ ) for GNR arrays deposited on SWNT macrostructures.  $S_{2D}$  was obtained by evaluating  $2 \langle \cos^2 \alpha \rangle - 1$  for each GNR and taking an average over all GNRs belonging to each aspect ratio group. As mentioned in previous paragraph,  $S_{2D}$  values obtained using our method of analysis represents the degree of ordering in a GNR array deposited on a perfectly aligned SWNT substrate. It “filters out” the undulations imparted onto the GNR assembly due to alignment imperfections in the SWNT substrate. The values of  $S_{2D}$  listed in Table 5.1 further illustrate the high degree of spontaneous alignment between SWNTs and GNRs, for all GNR aspect ratios. Interestingly, SWNT fibers produced better alignment among GNRs than the films. This is likely due to the grooved surface morphology of the fibers, which are composed of substructures of smaller diameter SWNT ropes and fibrils. The alignment of GNRs on SWNT fibers demonstrates the portability of this technique to other SWNT macrostructures, including curved surfaces. Since the alignment behavior of GNRs on SWNT films was independent of GNR aspect ratio, the deposition on fibers was tested with only short GNRs.

Self-alignment of gold nanoparticles with other interesting shapes, like high aspect ratio triangles and polygonal platelets, on aligned SWNT macrostructures was also studied using the same drop drying procedure. Interestingly, a significant number of

Table 5.1 : 2D scalar order parameter values for ordered arrays of GNRs, with varying aspect ratios, deposited on highly aligned SWNT films and short GNRs on fibers.

<b>Films</b>		<b>Fibers</b>	
GNR aspect ratio	Order Parameter	GNR aspect ratio	Order parameter
2-4	0.73	2-4	0.87
5-12	0.70	-	-
12-35	0.73	-	-

gold triangles and polygons spontaneously aligned during deposition, with one side of polygon parallel to the SWNT alignment direction. This demonstrates that alignment is not restricted to only rod shaped particles. The aligned triangles did not show any predominant polarity and the fraction of aligned nanoparticles was lower than that in the case of GNRs.

## 5.4 Discussion

The spontaneous alignment of GNRs on aligned SWNT substrates is driven by anisotropic interactions between GNRs and the SWNT structures. These anisotropic interactions are likely due to a combination of capillary, entropic and van der Waals forces that arise during drop drying on highly anisotropic nanostructured surfaces of aligned carpets and fibers. During drop drying, GNRs become confined into a progressively thinning liquid film and are pushed closer to the liquid free surface as well as the substrate which consists of aligned, anisotropic SWNTs and nanoscale grooves between

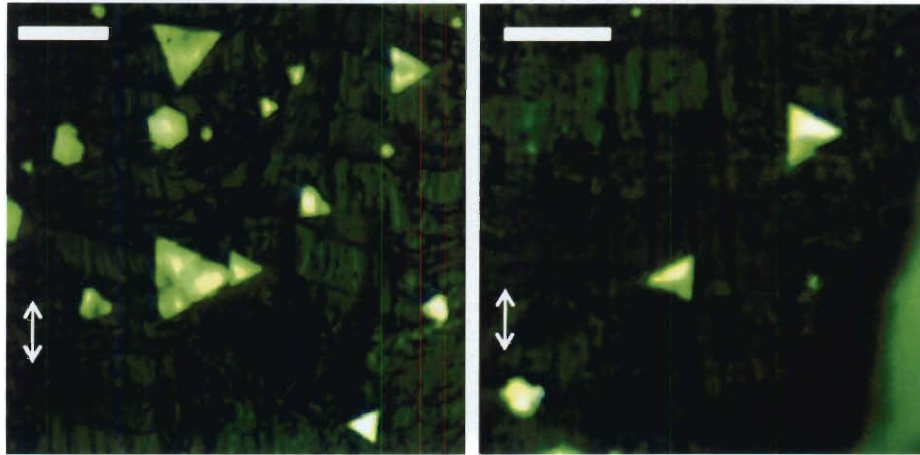


Figure 5.4 : Optical images (reflection mode, 50x lens) showing the spontaneous alignment of 2D gold triangles and platelets, with one side of each polygon aligned parallel to underlying SWNTs in aligned SWNT films. The direction of SWNT alignment is shown by double sided arrows. Scale bar is  $10\ \mu\text{m}$  in both images.

them. Under these circumstances, anisotropic capillary and combing forces may play an important role (Fig. 5.5(a)). Nanoscale orientation and assembly of colloidal particles and biopolymers mediated by capillarity and receding contact lines on similar micro- and nanostructured surfaces have been observed before [Huang *et al.* 2001, Lewandowski *et al.* 2008, Messer *et al.* 2000, Petit and Carbeck 2003, Salalha and Zussman 2005, Sharma *et al.* 2007]. For example, Strano *et al.* [Sharma *et al.* 2007] reported the role of hydrodynamic and capillary forces in the alignment, nanoscale positioning and deposition of individual SWNTs inside a cylindrical liquid droplet. Petit and Carbeck [Petit and Carbeck 2003] reported the molecular combing in microchannels, a process where DNA molecules get oriented and stretched at the interface

of liquid suspension and hydrophobic capillary substrate. Stebe et al. [Lewandowski *et al.* 2008] observed spontaneous rotation, alignment and ordering among anisotropic colloidal particles to minimize distortions at the liquid free surface and surface free energy. Anisotropic capillary forces and surface energy minimization are frequently used for the alignment and assembly of nanowires in device fabrication [Messer *et al.* 2000, Salalha and Zussman 2005].

In close proximity to the nanostructured SWNT substrate, overall translational and orientational entropy of GNRs is orientation dependent which gives rise to entropic alignment forces. Spontaneous alignment on nanoscale grooved surfaces has been observed for liquid crystals as well. However, there are important differences between these two systems. For thermotropic small-molecule LCs with molecular dimensions of the order of 1 nm (typically several nanometers in length and sub-nanometer in width), the entropic effects can be neglected (the ensuing entropic interactions are much smaller than confinement-induced elastic forces and anisotropic van der Waals interactions of LC molecules with the surfaces). The entropic forces become important in lyotropic LCs composed of cylindrical micelles (surfactant-based LCs) or long molecular aggregates (chromonic LCs) that can have lengths comparable to that of our nanorods ( $\sim 50$  nm). However, the most important difference is that LCs, due to their bulk elasticity, exhibit coupling of the orientation of micelles and chromonic aggregates at the surface with the far-field director away from the surface, which is

not the case for nanorods studied here. Our observations have closer resemblance to the entropy-mediated templating of patterns, from micro and nanostructured surfaces to colloidal particles in suspension, observed in other systems [Dinsmore *et al.* 1996, Gupta *et al.* 2006, Yodh *et al.* 2001]. Onsager theory [Onsager 1949] of nematic liquid crystals describes the spontaneous ordering of colloidal rigid rods for minimization of excluded volume and maximization of entropy; in our case, similar interactions between each rigid rod and the features on structured surfaces like walls of channels, protrusions and corners, help colloidal particles to attain well-defined positions and orientations. In the case of anisotropic colloids like GNRs, in unidirectional nanochannels created by SWNTs, alignment leads to reduction in their excluded volume by  $\sim(L-D)\cdot A$ , where  $A$  is the surface area of channel-like substrate nanostructures,  $L$  is the length of a GNR, and  $D$  is its diameter, as depicted in Fig. 5.5(b). This effect likely plays an important role in achieving the high orientational ordering of GNRs, especially for the case of SWNT fibers which can have a particularly “grooved” surface.

Finally, as GNRs deposit on the substrate, van der Waals interactions with individual SWNTs and SWNT bundles strongly affect their orientation, as depicted in Fig. 5.5(c). Aligning with SWNTs in the substrate, allows GNRs to maximize their area of contact and achieve a lower energy state by means of increased van der Waals interaction. An important point to note here is that GNRs should have stronger van

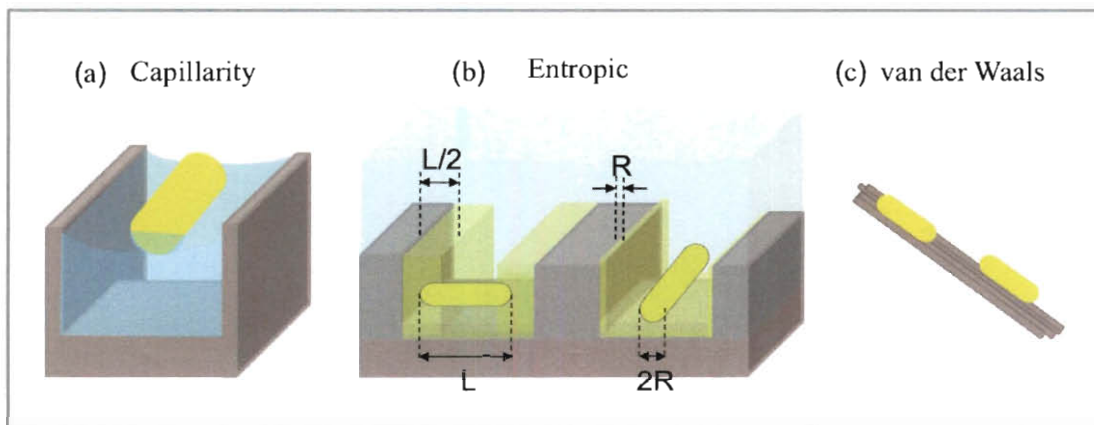


Figure 5.5 : The various forces contributing to assembly and alignment of gold nanorods on SWNT substrates: (a) Capillarity: capillary forces promote alignment of nanorods to minimize distortions in the liquid free surface. (b) Entropic forces: aligning with SWNTs and nanochannels between SWNTs minimizes excluded volume (depicted by the shaded region, which are inaccessible by the rod center of mass) and maximizes entropy. (c) Anisotropic van der Waals interactions; by aligning with the SWNTs, nanorods maximize their area of contact and reduce free energy.

der Waals attraction towards each other than to SWNTs, because gold has a higher Hamaker constant than carbon. However, a stabilization layer of micellar CTAB on GNRs prevents their self-aggregation and flocculation in suspension, while allowing them to interact with bare uncoated SWNT surfaces during deposition. Using a high concentration GNR suspension during deposition, however, can lead to deposition of multiple layers of GNRs over the same spot. The secondary and more layers of GNRs may experience much weaker templating effect of the underlying SWNT.

Similar forces are possibly in play for the case of anisotropic gold platelets and polygons (Fig. 5.4). In the simplest case, an anisotropic gold triangle or platelet (5

nm thick, 10  $\mu\text{m}$  wide) approaching the SWNT film surface with its plane perpendicular to it behaves like a GNR with 5 nm diameter. Thus, the interplay of various alignment forces leads to deposition of the triangle with one of the sides parallel to SWNT orientation. The interactions and potential benefits of alignment become more complex for other possible plane orientations, which explains the lower fraction of aligned particles observed in the case of polygonal, compared to GNRs.

## 5.5 Conclusions

We have demonstrated a drop-drying based simple and versatile technique for the ordered assembly of gold nanoparticles on highly aligned SWNT films and fibers. The method was successfully demonstrated using GNRs with aspect ratios ranging from 2-35, gold triangles with side length up to 10  $\mu\text{m}$  and 5 nm thickness, and other polygonal shapes. The nanoparticles show strong interaction with SWNTs, and spontaneously align on the anisotropic substrates during deposition. These ordered arrays of plasmonic GNRs supported on strong, durable, inert and electrically conductive SWNT substrates can potentially better serve the currently existing GNR applications and act as a platform for development of advanced metamaterials.

## Chapter 6

# Self-assembly and Dielectrophoresis: 1-D Fibrils from Aqueous SWNT Suspensions

### 6.1 Introduction

SWNTs are a promising class of material for a host of electronic applications. Their high aspect ratio, high current carrying capacity, ballistic charge transport, and low turn on fields are ideal for field emission devices, high frequency transistors, alternative probes for AFMs, conductive AFMs, and STMs [Baughman *et al.* 2002, Choi *et al.* 1999, Dai *et al.* 1998, Hafner *et al.* 1999, Konishi *et al.* 2007, Lee *et al.* 2005, Park *et al.* 2005, Tang *et al.* 2005, Wong *et al.* 1998, Yu *et al.* 1999]. Their low density, excellent electrical and thermal conductivity, mechanical strength and chemical inertness make them desirable candidates for high strength fibers and conductive wires, as demonstrated by several groups [Badaire *et al.* 2004, Davis *et al.* 2009, Ericson *et al.* 2004, Koziol *et al.* 2007, Vigolo *et al.* 2000]. The electrical and mechanical performance of macroscopic SWNT fibers partly depends on the properties of individual constituent molecules, like SWNT chirality, average length, diameter, and quality [Behabtu *et al.* 2008]. There is a strong interest in understanding the effect of



each of these parameters on the performance of macroscopic fibers. That will allow us to determine the optimal CNT sample for fiber fabrication, and obtain a practical estimate for highest achievable fiber performance.

The current techniques for obtaining chirality or electronic-type enriched SWNTs [Haroz *et al.* 2010, Harutyunyan *et al.* 2009, Krupke *et al.* 2003], and long CNTs (> tens of microns) with good control over diameter and quality [Xu *et al.* 2006], produce limited amount of material (milligrams). This is unsuitable for fabrication of macroscopic fibers which typically requires  $\sim 1$  gram of material. Aligned “SWNT fibrils” can offer a solution to this issue. SWNT fibrils can be defined as 1-D structures that are sub-micron to several microns in diameter and hundreds of microns in length. Being composed of 100-1000s of SWNTs in cross-section as well as length, their performance should mimic that of bulk materials like macroscopic fibers. Moreover, they can be fabricated from dilute suspensions prepared using small amount of material (< milligrams), as described below.

Fabrication of fibrils from dilute SWNT suspensions, with a high degree of SWNT alignment, requires the ability to trap, align, and assemble individual SWNTs in a controlled and preferably continuous manner. The small size of SWNTs, their Brownian nature and strong tendency to aggregate or flocculate makes this a challenging task. Electrophoresis (EP) and dielectrophoresis (DEP) were recently shown as effective tools to control and manipulate SWNTs. In 2003, Krupke *et al.* [2003]

demonstrated that alternating current (AC) DEP can be used to polarize SWNTs, align them along the e-field direction (overriding their tendency to orient randomly by Brownian motion) and move them along the e-field gradient. A high axial polarizability of SWNTs makes these e-field based techniques extremely powerful; their successful applications include SWNT separation according to electronic type and thin film deposition [Henrich *et al.* 2005, Krupke *et al.* 2004, Lutz and Donovan 2005].

The amplification of e-field at a sharpened metal tip and the associated e-field gradient have been frequently utilized for deposition of individual CNTs and small diameter bundles to fabricate microscopy probe tips, and field emission devices [Konishi *et al.* 2007, Lee *et al.* 2005, Tang *et al.* 2005, Wei *et al.* 2008a;b]. Gommans *et al.* [2000] and Annamalai *et al.* [2005] reported spinning of macroscopic 1-D SWNT “fibrils” from SWNT bundles and networks suspended in organic solvents, using DC-electrophoresis. Tang *et al.* [2003] and Ma *et al.* [2009] reported fabrication of SWNT fibrils using dielectrophoresis on functionalized/shortened SWNTs suspended in water. Hulman *et al.* [2007] reported fabrication of long fibrils from MWNT networks suspended in DMF. The fabrication of macroscopic fibrils from *pristine* and *individualized* SWNTs has, however, remained largely elusive.

A commonly used technique for dispersion of individualized SWNTs is with the aid of surfactants in water. The typical steps involved in the dispersion process are

outlined in O'Connell et al. [2001]. Primary advantages of this mode of SWNT dispersion include: minimal to no structural damage to SWNTs (in contrast to chemical functionalization) and hence preservation of the pristine molecular properties, availability of a host of suitable surfactants with wide range of properties [Moore et al. 2003] (ionic-nonionic, polymer chain length, nature of hydrophilic-hydrophobic groups, to name a few), a relatively large fraction of individualized SWNTs in the suspension [Sun et al. 2008, Zhou et al. 2004a]. The Brownian nature of individualized SWNTs, however, makes their trapping and manipulation with DEP challenging. The surfactant micellar layer adsorbed on each SWNT screens their effective polarizability, further reducing the efficacy of DEP. Infact, the first successful fabrication of SWNT fibril from a SWNT-surfactant aqueous suspension was reported by Han et al. [2010] only recently.

In this Thesis chapter, we present a novel two-step process for fabrication of macroscopic SWNT fibrils from SWNT-surfactant aqueous suspensions. In the first step, colloidal self-assembly among surfactant stabilized SWNTs is induced by addition of an electrolyte. In second step, DEP is performed on this modified suspension leading to the formation of macroscopic SWNT fibrils. The two-step process is shown schematically in Fig. 6.1. We show that the self-assembled SWNT aggregates have a significantly better response to external e-fields, (owing to their larger size) which in turn dramatically improves efficacy and reproducibility of the DEP fibril formation

process.

## **6.2 Experimental Methods**

Aqueous SWNT suspensions were prepared by dispersing SWNTs in a solution of 1 wt% sodium deoxycholate (DOC) in water using the process described by O'Connell et al. [2001]. The SWNT-surfactant suspensions were ultracentrifuged at 150,000 g for 4 hours, resulting in SWNT concentration in the range of 40 - 100 ppm and consisting of primarily individual SWNTs.

### **6.2.1 Colloidal Self-Assembly: Mini-Fibrils**

Controlled colloidal aggregation in SWNT suspension was initiated by addition of small amounts of electrolyte NaCl. Different concentrations, ranging from 1.25 mM to 1 M, of NaCl were added to a SWNT suspension and a 1 wt% solution of DOC in water (control sample). Both the samples were observed under an optical microscope daily over a period of several days in order to monitor the self-assembly process. Suspensions for DEP were prepared by adding about 0.05 M salt to SWNT-DOC suspensions and leaving overnight.

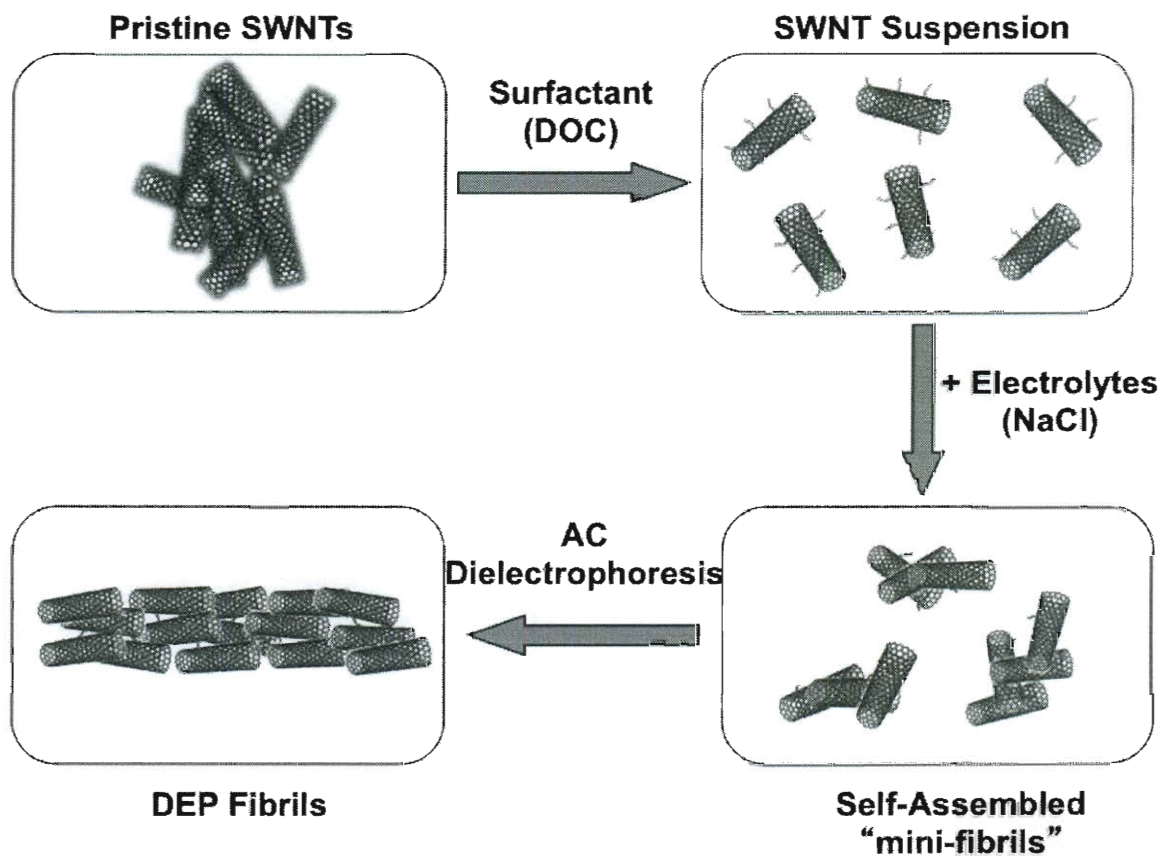


Figure 6.1 : Schematic diagram of the two step SWNT fibril fabrication process. Individual SWNTs stabilized with sodium deoxycholate (DOC) and suspended in water are self assembled into mini-fibrils by addition of NaCl. DEP on this modified suspension, with preformed mini-fibrils, leads to formation of macroscopic SWNT fibrils.

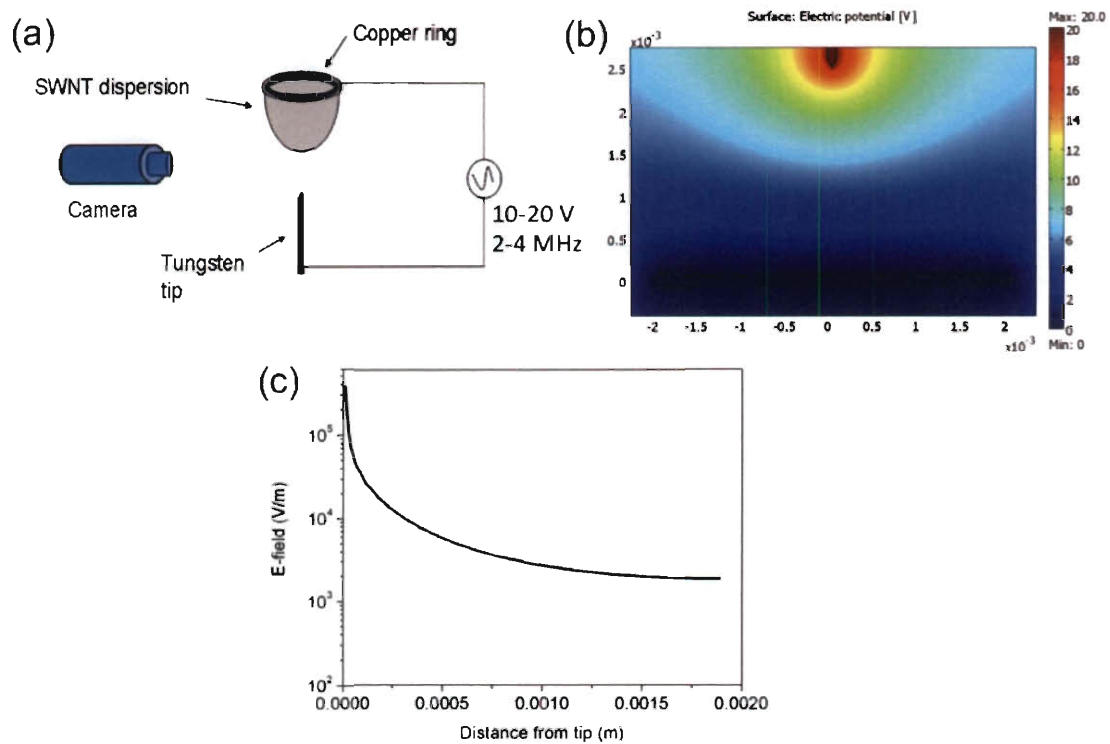


Figure 6.2 : (a) Cartoon of the experimental setup used for DEP experiments. (b) Electric potential inside the liquid sample, between the tungsten tip and copper ring (electrodes), under 20 V<sub>p-p</sub> (1 MHz) applied voltage (c) Variation of electric field between the 2 electrodes inside liquid droplet. (b) and (c) were obtained using COM-SOL multiphysics modeling software (2-D axisymmetric model).

### 6.2.2 AC Dielectrophoresis

DEP was conducted on SWNT suspensions using the setup shown in Fig. 6.2. A RF power amplifier (ENI 3200L) connected to a signal generator (Wavetek model 2407) was used to produce 4 MHz AC current. An oscilloscope (Tektronix 465B) was used to measure the voltage across the electrodes, which consisted of an electrochemically sharpened tungsten tip [Guise *et al.* 2002] and a 4 mm diameter copper ring made out of 1 mm diameter copper wire. A few drops of the sample were placed inside the copper ring and the tungsten tip was inserted into the drop. A voltage ranging from 10 to 20 volts (peak-to-peak) was applied between the electrodes. A long working distance camera coupled with a CCD detector (Photometrics CoolSnap cf) was employed to image the tungsten tip inside the sample droplet and visualize the fibril formation process. Typically fibrils could be observed on the tip within a period of 2-5 minutes after which the tip was slowly pulled out of the droplet. The voltage was kept on till the fibril was completely pulled out of the liquid.

## 6.3 Results and Discussions

### 6.3.1 Mini-Fibrils

The addition of small amounts (as low as 1.25 mM) of salt in the SWNT-DOC suspension led to the formation of long and slender needle-like fibrillar structures, referred

Table 6.1 : List of microstructures formed by the addition of varying amounts of NaCl in  $\sim 50$  ppm SWNT-DOC aqueous suspension and DOC aqueous solution (control sample). All samples were left overnight after addition of salt, and then observed under optical microscope.

<b>Salt (M)</b>	<b>Conc.</b>	<b>SWNT-DOC Suspension</b>	<b>DOC Solution</b>
0.0025		Abundant needle shaped mini-fibrils	No fibrils
0.005		Abundant needle shaped mini-fibrils	No fibrils
0.05		Abundant needle shaped mini-fibrils	No fibrils
0.08		Fewer mini-fibrils	No fibrils
0.1		Few mini-fibrils, Dark aggregates	No fibrils
0.5		No mini-fibrils, Dark aggregates	No fibrils
0.8		Entangled mesh	Entangled mesh
1.0		Entangled mesh	Entangled mesh

to as “mini-fibrils”. The number of mini-fibrils in suspension decreased with increasing salt concentration. For salt concentrations above  $\sim 0.1$  M, the mini-fibrils were pre-dominantly replaced by dark, lumpy aggregates. At very high salt concentrations ( $\sim 1$  M), the suspension turned gel-like and consisted of dense entangled mesh of large strand-like structures. In contrast, the control sample (1 wt% DOC solution) did not show any needle-like fibrillar structure for low concentrations of salt; a few dark aggregates could be observed at intermediate concentrations. At very high concentrations ( $> 0.8$  M), the solution turned gel-like and consisted of dense entangled mesh of large strand-like structures; similar to the case of SWNT suspension. The observed morphology vs. salt concentration is summarized in Table 6.2.

It is evident that SWNTs in the suspension play a key role in the mini-fibril



formation process at low salt concentrations. Previous studies have shown that addition of counter-ions to an ionic surfactant solution destabilizes the electric double layer around surfactant micelles, screening their electrostatic repulsion and leading to changes in micellar shape and aggregation or flocculation among surfactant stabilized colloidal particles [Cates and Candau 1990, Lopez *et al.* 1996]. In our case, the addition of NaCl facilitates self-assembly of surfactant coated individual SWNTs into needle-like mini-fibrils; the SWNTs effectively serve as templates for formation of 1-D mini-fibrils instead of 3-D lumps.

The mini-fibrils were characterized using optical microscopy and Raman spectroscopy. The transmission mode optical microscopy image of a network of mini-fibrils in SWNT-DOC-NaCl suspension is shown in Fig. 6.3(a). Optical monitoring of the mini-fibrils over a period of time revealed that their structure is labile and the average length of structures decreases over time. This can be attributed to instability of the larger structures and their drive towards equilibrium. The length distribution of mini-fibrils in a SWNT suspension as a function of time can be found in the appendix section.

The presence of SWNTs in mini-fibrils was confirmed using Raman spectroscopy (633 nm excitation, Renishaw inVia). Figure 6.3(b) shows a mini-fibril (gray) spin coated from SWNT-DOC-NaCl suspension on a quartz substrate. Raman spectra were collected at 10 different spots along a straight line (black-green) drawn per-

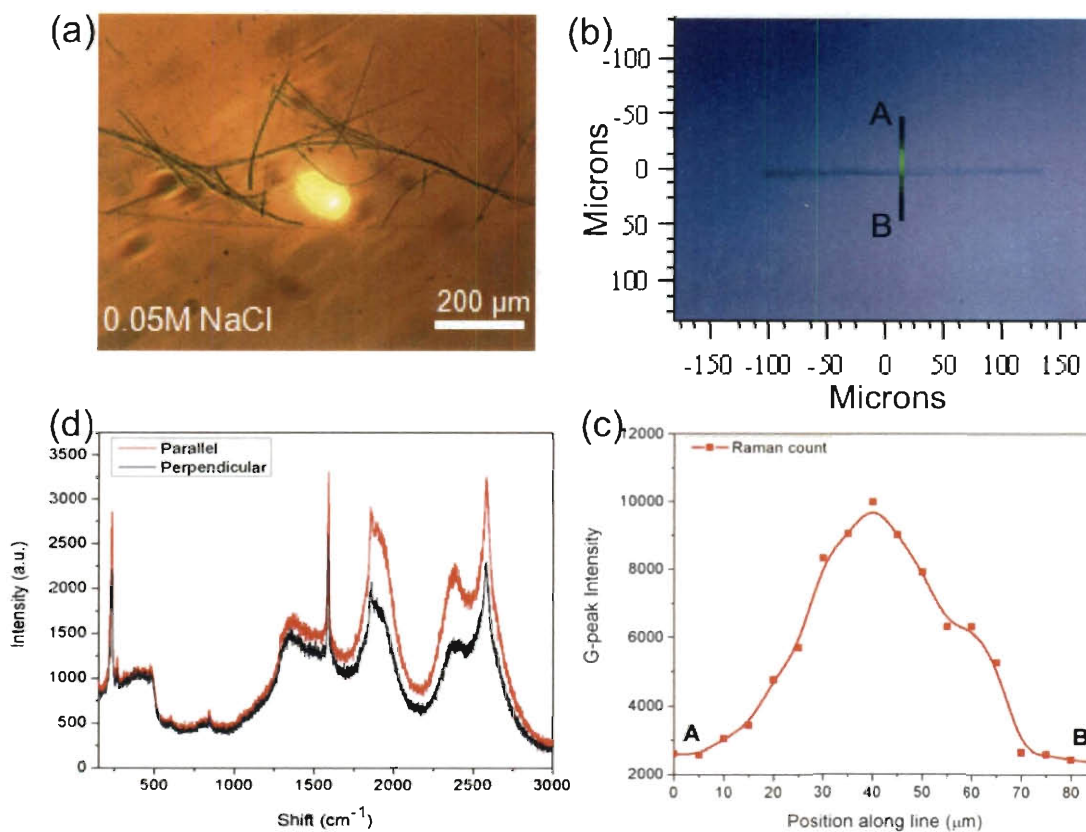


Figure 6.3 : (a) Transmission mode optical microscopy image of mini-fibrils in suspension, formed by addition of 0.05 M NaCl to SWNT-DOC suspension. (b) Reflection mode optical image of a mini-fibril (gray) deposited on quartz substrate by spin coating. Raman spectroscopy, at 633 nm excitation, was performed at 10 spots along the straight line A-B (perpendicular to the fibril). The plot of G-peak ( $1591\text{ cm}^{-1}$ ) intensity vs. position along the line is shown in (c). A five-fold increase in signal strength on top of the minifibril confirms presence of SWNTs. (d) Raman spectra, with laser polarization parallel and perpendicular to the long axis of minifibril.

pendicular to the mini-fibril. The G-peak ( $1591\text{ cm}^{-1}$ ) intensity shows more than five-fold increase as the laser spot passes over the mini-fibril (Fig. 6.3(c)), indicating the presence of SWNTs in the mini-fibrils. Note that the G-peak intensity profile shows a gradual rise and fall instead of a sharp peak over the mini-fibril location. This is likely due to the laser beam spot size ( $\sim 15 \times 15\ \mu\text{m}^2$ ) being much larger than mini-fibril's expected diameter ( $< 1\ \mu\text{m}$ ). The base signal of  $\sim 2500$  counts observed in regions away from mini-fibril (ends of line A-B) is due to scattered SWNTs from the suspension which get coated on the quartz substrate during spin coating. The mini-fibrils were also probed for potential alignment among SWNTs, by collecting Raman spectra with the laser polarized parallel and perpendicular to its along axis. The polarized Raman spectroscopy did not show any significant alignment (Fig. 6.3(d)).

In addition to SWNT, the mini-fibrils contain high amounts of surfactant. Under scanning electron microscopy (SEM), several seconds of exposure to an e-beam (15 kV and x 2,500 magnification) was typically sufficient to damage and fragment the mini-fibrils. The mini-fibrils collected on a glass or silicon substrate by spin coating were also easily destroyed by the addition of water and ethanol, suggesting their high surfactant content.

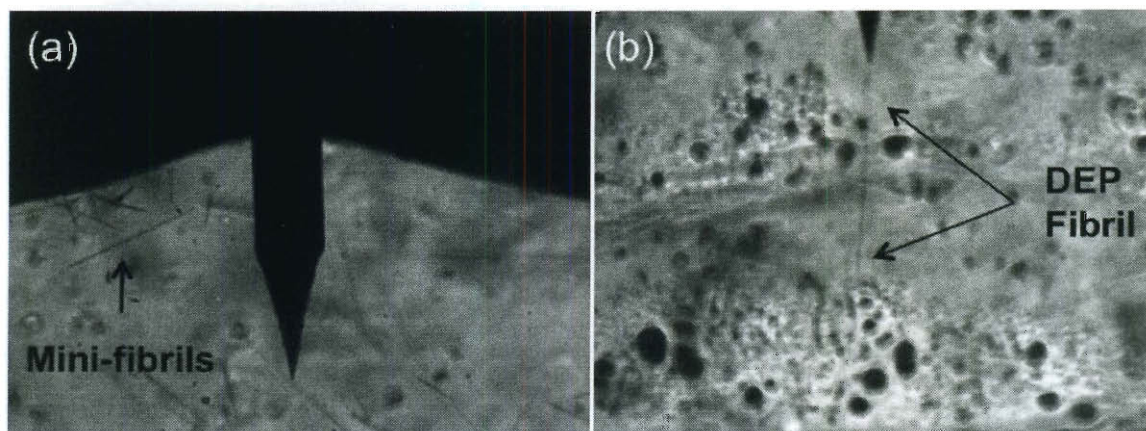


Figure 6.4 : (a) Image of a Tungsten tip inside SWNT-DOC-NaCl suspension drop (40-100 ppm SWNT, 0.05 M NaCl) during DEP (20 V<sub>p-p</sub>, 1 MHz). Preformed mini-fibrils in suspension can be observed. (b) A fibril attached to the Tungsten tip via DEP process. Images were obtained using a long working distance camera couple to a CCD detector.

### 6.3.2 DEP SWNT Fibrils

The DEP experiment was carried out on 3 type of suspensions: (a) pure SWNT-DOC suspension (without any salt or preformed mini-fibrils), (b) SWNT-DOC-NaCl suspension right after addition of NaCl (i.e., without preformed mini-fibrils), (c) SWNT-DOC-NaCl suspensions with NaCl added at least a day before (i.e., with preformed mini-fibrils). Remarkably, DEP on samples (a) and (b) typically did not produce macroscopic fibrils (length > 100  $\mu\text{m}$ ). In contrast, long fibrils, several hundred microns in length, were fabricated reproducibly using (c), which had preformed mini-fibrils in suspension.

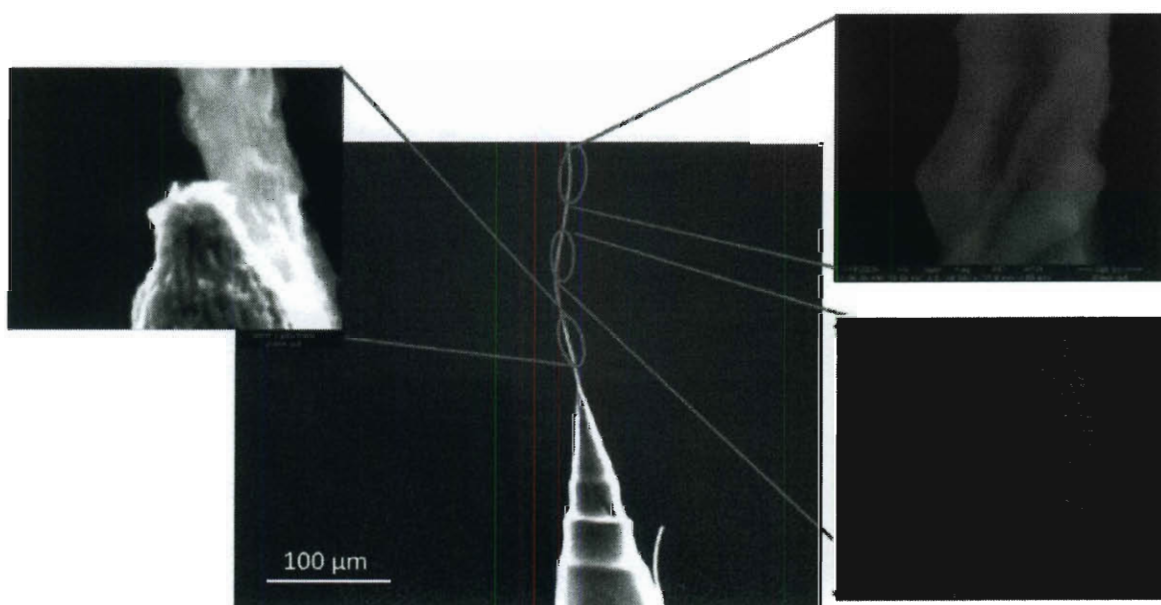


Figure 6.5 : SEM images of a DEP fibril, fabricated from a SWNT-DOC-NaCl suspension (40-100 ppm SWNT, 0.05 M NaCl) with preformed mini-fibrils. The fibril is  $\sim 1 \mu\text{m}$  in diameter and more than  $200 \mu\text{m}$  in length. The insets show higher magnification images of various parts of the fibril, depicting smooth, strand-like substructures indicating that the fibril is composed of multiple mini-fibrils.

Figure 6.4(a) shows image of a tungsten tip inside the SWNT-DOC-NaCl suspension drop during a DEP experiment. Several preformed mini-fibrils can be seen in suspension. A SWNT fibril attached to the tip via DEP can be observed in Fig. 6.4(b). The images were obtained using a long working distance camera coupled to a CCD detector. Figure 6.5 shows SEM images of a typical fibril fabricated from SWNT-DOC-NaCl suspension using DEP. The particular fibril imaged here is  $\sim 1 \mu\text{m}$  in diameter and more than  $200 \mu\text{m}$  in length. Strand-like substructures, like the one shown in top-right inset, indicate that the DEP fibril is composed of smaller mini-fibrils present in the suspension. The smooth morphology of the outer skin, shown in the lower-right inset, indicates the presence of surfactants in the fibril.

The Raman analysis of DEP fibrils is shown in Fig. 6.6. The DEP fibrils showed a high degree of SWNT alignment; as documented by a five times higher G-peak intensity when probed with the laser beam parallel to the fibril axis, in comparison to perpendicular orientation. This is in sharp contrast to mini-fibrils, which did not possess significant SWNT alignment. The higher alignment in DEP fibrils can be attributed to two main reasons: Mini-fibrils are loose aggregates whose formation is primarily guided by weak inter-micellar interactions and van der Waals forces between micelle encapsulated individual SWNTs, which are Brownian particles at room temperature. In contrast, the alignment and assembly of the mini-fibrils into DEP fibrils occurs under a strong electric field. Secondly, as the tip (with the fibril attached

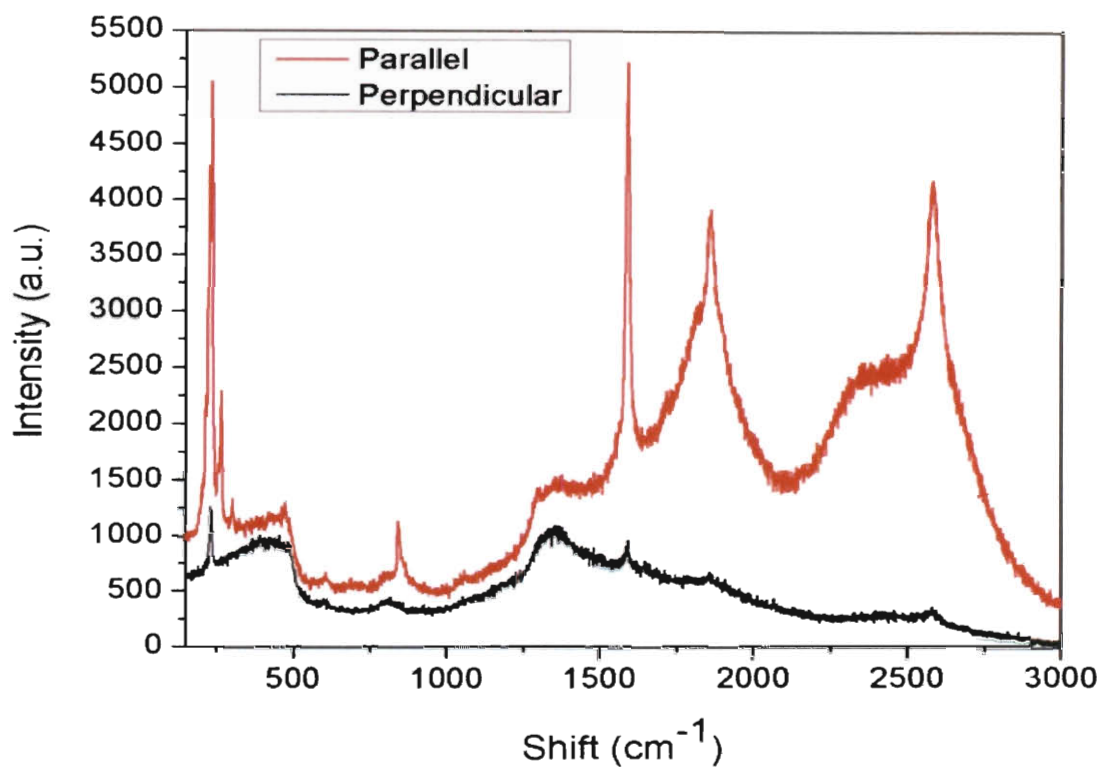


Figure 6.6 : Raman spectrum, obtained with 633 nm excitation laser, of a DEP fibril with the laser polarization parallel and perpendicular to the fibril long axis. A five-fold stronger G-peak ( $1591\text{ cm}^{-1}$ ) signal for parallel laser polarization indicates significant alignment among SWNTs in the fibril. The DEP fibril was fabricated from SWNT-DOC-NaCl suspension containing pre-formed mini-fibrils.

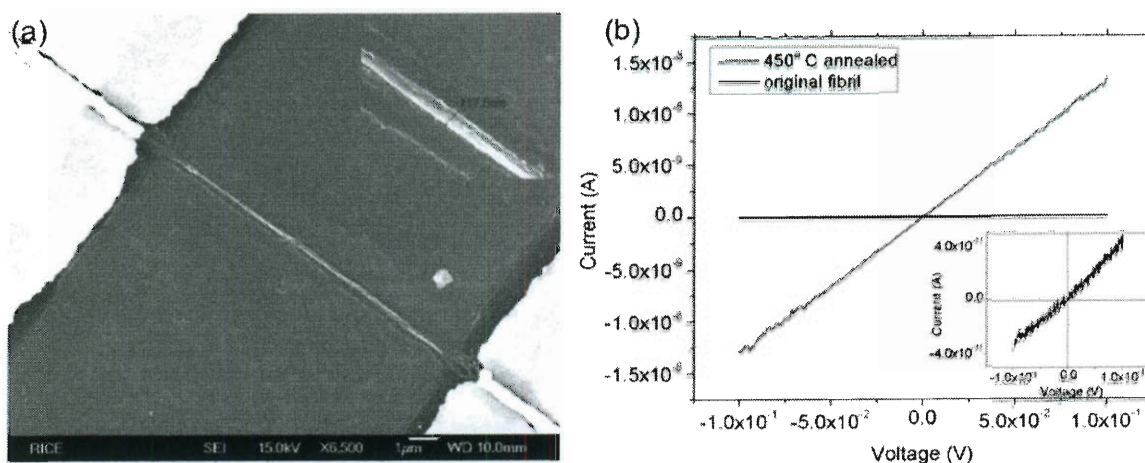


Figure 6.7 : (a) SEM of a DEP fibril, fabricated from SWNT-DOC-NaCl suspension and annealed at 450 °C under Argon flow, with gold electrodes deposited on top. (b) The I-V transport properties of the SWNT fibril measured using a 4 point probe before and after annealing. Inset shows scaled up version of I-V measurements of original fibril before annealing. Annealing led to almost five orders of magnitude improvement in fibril electrical conductivity.

to its end) is slowly extracted from the liquid droplet, the fibril passes through the meniscus where the capillary forces produce a strong “compacting” and “combing effect”, further enhancing SWNT alignment. On average, the DEP fibrils were found to have at least 3.5 - 4 times higher SWNT alignment than the mini-fibrils.

The DEP fibrils were collected on silicon substrates for electrical characterization. Four gold electrodes (500 nm thick, 10  $\mu$ m spacing) were deposited on the fibril by means of photolithography (Fig. 6.7(a)). The electrical transport properties of the fibril were measured using 4-probes on a semiconductor analyzer/probe station under high vacuum. The electrical conductivity of an as-prepared DEP fibril, shown



in Fig. 6.7(b) inset, was measured to be  $5.6 \times 10^{-4} \text{ S}\cdot\text{m}^{-1}$ . The low conductivity value, compared to typical values obtained for SWNT fibers [Badaire *et al.* 2004, Davis *et al.* 2009], can be attributed to the presence of high amount of surfactant encapsulating the fibrils. Thermo-gravimetric analysis (TGA) of pure solid DOC powder revealed that it loses more than 80% of its mass upon heating to a temperature of 450 °C under inert environment. Based on the TGA study data, the DEP fibril was subsequently annealed at 450 °C in Argon flow for a period of 4 hours. The electrical conductivity of the fibril improved by almost five orders of magnitude upon annealing; the conductivity of the annealed fibril was measured to be  $1.5 \times 10^1 \text{ S}\cdot\text{m}^{-1}$ , as shown in Fig. 6.7(b).

DEP fibrils were also found to be significantly more stable and durable than self-assembled mini-fibrils. They were able to withstand exposure to e-beam under SEM (15 kV x27000 magnification) and addition of polar solvents such as water or ethanol without fragmenting or significant structural damage.

### 6.3.3 Theoretical Analysis

We performed force balance and scaling analysis to gain further insights on why mini-fibrils show better response to DEP forces, compared to individualized SWNTs, and the subsequent effect on fibril formation process. A comprehensive analysis on the motion of SWNTs under AC-DEP can be found in Mendes *et al.* [2008]. A colloidal

particle (e.g., SWNT), suspended in liquid medium (with no liquid flow) and exposed to non-uniform electric field, has two competing forces acting on it: DEP force, trying to align the particle in the direction of electric field and move it along electric field gradient, and Brownian force trying to disorient the particle. The relative strength and dominance of these two forces, which scales with the dimensions of the colloidal particle (length in the case of rod like particles), ultimately governs the success of DEP fibril formation.

The translational DEP force acting on a SWNT can be expressed as:

$$F_{\text{DEP}} = V_{\text{NT}}\varepsilon_m \text{Re}[K]\nabla E^2 \quad (6.1)$$

where  $V_{\text{NT}}$  is the SWNT effective volume,  $\varepsilon_m$  is the dielectric constant of the liquid medium,  $K$  is the Clausius-Mossotti factor, and  $E$  is the electric field. The Clausius-Mossotti factor depends on the difference between complex dielectric functions of the particle and medium, and depolarization factors ( $L^{\parallel}, L^{\perp}$ ) which take into account particle shape anisotropy [Mendes *et al.* 2008]. Collecting the length dependence of each term on the RHS of eq. 6.1 ( $V_{\text{NT}} \propto l_{\text{NT}}, K \propto l_{\text{NT}}^2$ , where  $l_{\text{NT}}$  is the length of SWNT), it can be shown that the DEP force scales as  $l_{\text{NT}}^3$ .

The Brownian force acting on a SWNT is a Gaussian random variable with zero

mean and a second moment given by:

$$\langle F^B(t')F^B(t'') \rangle = 2k_B T \zeta \delta(t' - t'') \quad (6.2)$$

where  $k_B$  is the Boltzmann constant,  $T$  is the temperature, and  $\zeta$  is the translational friction coefficient. Since,  $\zeta$  ( $\zeta \propto l_{NT}$ ) is the only “particle length” dependent term in the RHS of Eq. 6.2, the Brownian force scales with the length of the particle as  $l_{NT}^{0.5}$ . Therefore, in the interplay between DEP and Brownian forces, the DEP forces grow faster than the Brownian fluctuations, as the size of colloidal particles increases.

Similar analysis performed on the rotational motion of rod-like colloidal particles suspended in liquid medium (with no liquid flow) and exposed to non-uniform electric field shows that the DEP torque scales as  $l_{NT}^3$  whereas the Brownian random torque scales as  $l_{NT}^{1.5}$ . (Further details in appendix and Mendes et al. [2008]) Therefore, for a given e-field and e-field gradient, the effectiveness of the DEP force in aligning, and moving a particle increases as the length of the particle increases.

The relative strengths of the DEP force and Brownian motion can be monitored by employing two dimensionless numbers:

$$\begin{aligned} T_{\text{DEP-B}} &= \left| \frac{U_{\text{DEP}}^T}{kT} \right| \\ R_{\text{DEP-B}} &= \left| \frac{U_{\text{DEP}}^R}{kT} \right| \end{aligned} \quad (6.3)$$

where  $U_{\text{DEP}}^T$  is the translational DEP energy defined as  $U_{\text{DEP}}^T = V_{\text{NT}}\varepsilon_m \text{Re}[K]E^2$  ([Krupke *et al.* 2004]), and  $U_{\text{DEP}}^R$  is the rotational DEP energy defined as  $U_{\text{DEP}}^R = \text{Max}\{V_{\text{NT}}\varepsilon_m \text{Re}[K^{\parallel}K^{\perp}](L^{\parallel} - L^{\perp})E_{\text{RMS}}^2(\vec{u} \cdot \vec{r})(\vec{u} \times \vec{r})\}$ , where  $k$  is the Boltzmann constant,  $T$  is temperature,  $K^{\parallel}$  and  $K^{\perp}$  are the parallel and perpendicular components of  $K$ ,  $L^{\parallel}$  and  $L^{\perp}$  are the parallel and perpendicular depolarization factors [Mendes *et al.* 2008]. When the translational and rotational DEP powers become close to 1, the DEP forces begin to dominate over Brownian forces and fibril formation becomes feasible.

The effective size and dielectric properties of an ionic surfactant encapsulated individual SWNT are reported by Mendes *et al.* [2008] and Krupke *et al.* [2004] For HiPCo SWNTs,  $l_{\text{NT}} \sim 400$  nm,  $r_{\text{NT}} \sim 0.5$  nm,  $\varepsilon^*$  (semiconducting SWNT) =  $5\varepsilon + i0.35/\omega$ ,  $\varepsilon^*$  (metallic SWNT) =  $10^4 + i\sigma_m/\omega$ , where  $\sigma_m = 10^4$  S/m is the conductivity of metallic SWNTs and  $\omega$  is the DEP signal frequency.

The average size of the mini-fibrils, determined using AFM, was found to be  $l_{\text{mini-fibril}} \sim 25$   $\mu\text{m}$  and  $r_{\text{mini-fibril}} \sim 150$  nm. In order to estimate the dielectric properties of mini-fibrils, their composition needed to be determined. Annealing the mini-fibril samples at 450 °C under Argon flow and performing SEM imaging before and after annealing, revealed that the mini-fibrils contain  $\sim 10$  vol% SWNTs. Their dielectric response can, therefore, be modeled as that of a composite material with DOC as the host matrix and 3 vol% metallic SWNTs and 7 vol% semiconducting

SWNTs as conductive fillers.

The dielectric properties of mini-fibrils was calculated using a method known as “dielectric mixing rule” [Sihvola 2000]. Dielectric mixing rules are arithmetic formulas which allow calculation of the effective dielectric permittivity of a mixture or composite, based on the permittivities, fractional volumes, shape, size and orientation of the constituents. The estimates are typically considered valid in the ‘long wavelength limit’; i.e., when the electric field wavelength is much larger ( $\sim$  factor of 10) than the size of inclusions of fillers. In our case, the applied electric field wavelength, 300 meters (corresponding to 1 MHz), is nine orders of magnitude larger than the length of SWNTs.

According to the dielectric mixing rule, the effective complex permittivity of a composite ( $\epsilon_{\text{eff}}$ ), comprising of  $n$  different inclusion phases (i.e., filler materials) with each phase consisting of high aspect ratio ellipsoids with permittivity -  $\epsilon_{i,n}$  ( $i$  can be  $x, y$  or  $z$  direction), embedded into a host matrix (permittivity -  $\epsilon_{\text{mat}}$ ), can be calculated using the following expression [Sihvola 2000]:

$$\epsilon_{\text{eff}} = \epsilon_{\text{mat}} + \epsilon_{\text{mat}} \cdot \frac{\sum_{n=1}^N \left( \frac{f_n}{3} \sum_{j=x,y,z} \frac{\epsilon_{i,n} - \epsilon_{\text{mat}}}{\epsilon_{\text{mat}} + L^{j,n} (\epsilon_{i,n} - \epsilon_{\text{mat}})} \right)}{1 - \sum_{n=1}^N \left( \frac{f_n}{3} \sum_{j=x,y,z} \frac{\epsilon_{i,n} - \epsilon_{\text{mat}}}{\epsilon_{\text{mat}} L^{j,n} (\epsilon_{i,n} - \epsilon_{\text{mat}})} \right)} \quad (6.4)$$

where  $f_n$  is volume fraction of the  $n^{\text{th}}$  inclusion phase,  $L^{j,n}$  (i.e.,  $L^{x,n}$ ,  $L^{y,n}$  and  $L^{z,n}$ )

Table 6.2 : Dimensionless quantities  $T_{\text{DEP-B}}$  and  $R_{\text{DEP-B}}$  quantifying the relative strengths of translational and rotational DEP and Brownian forces, respectively, on individual SWNTs suspended in a SWNT-DOC suspension and mini-fibrils suspended in a SWNT-DOC-NaCl suspension.

	$T_{\text{DEP-B}}$	$R_{\text{DEP-B}}$
Individual SWNT	$1.0 \times 10^{-4}$ (metallic)	$4.92 \times 10^{-5}$ (metallic)
	$7.58 \times 10^{-7}$ (semiconducting)	$3.34 \times 10^{-7}$ (semiconducting)
Mini-fibril	0.31	0.02

are the depolarization factors of the ellipsoids of  $n^{\text{th}}$  inclusion in the  $x$ ,  $y$  and  $z$  directions respectively.

In case of mini-fibrils, the following parameter values were used to calculate its dielectric permittivity ( $\epsilon_{\text{mfb}}$ ): dielectric permittivity of host matrix -  $\epsilon_{\text{DOC}} = 2.5 + i0.2$  (see appendix for details), two inclusion phases- metallic type SWNTs and semiconducting SWNTs with volume fractions of 3 % and 7 % respectively,  $L^{x,n} = L^{\parallel}$  and  $L^{y,n}, L^{z,n} = L^{\perp}$  for both metallic and semiconducting SWNTs. Using the above dielectric mixing expression, the complex permittivity of the mini-fibrils was estimated to be,  $\epsilon_{\text{mfb}} = 101.77 + i0.38$ .

Table 6.2 lists the values of  $T_{\text{DEP-B}}$  and  $R_{\text{DEP-B}}$  for individual SWNTs in a SWNT-DOC decant and mini-fibrils in a SWNT-DOC-NaCl suspension, under DEP. The dimensionless quantities were calculated at temperature  $T=300$  K and electric field  $E= 9500$  V/m, which is the average electric field between the electrodes in our ex-

periments (calculated via COMSOL modeling, shown in Fig. 6.2). Both quantities elucidate that for a fixed electric field, the DEP force is about 10,000 times more effective in controlling and attracting mini-fibrils than individual SWNTs; corroborating our experimental observations.

## 6.4 Conclusions

This study establishes a novel technique for the fabrication of macroscopic, highly ordered SWNT fibrils from SWNT-surfactant colloidal dispersions. The method is essentially a combination of two versatile and well known processes: surfactant micelle self assembly and alternating current dielectrophoresis. It presents a significant improvement from current fibril fabrication methods in that it allows fabrication of these 1-D structures from widely used dilute SWNT-surfactant dispersions, including single chirality enriched SWNT suspensions produced by DGU process, without inducing any structural damage to the SWNT. Through further engineering and development, this versatile method would allow the large scale continuous fabrication of highly ordered SWNT fibrils and fibers with superior performance which truly represent the properties of the individual SWNT molecule.

## 6.5 Appendix

### 6.5.1 Rotational Motion of Colloidal Particles under DEP

The DEP torque acting on a particle (SWNT in this case), suspended in liquid medium (with no liquid flow) and exposed to non-uniform electric field, can be expressed as [Mendes *et al.* 2008]:

$$M_{\text{DEP}} = V_{\text{NT}} \epsilon_m \text{Re}[K^{\parallel} K^{\perp}] (L^{\perp} - L^{\parallel}) E_{\text{RMS}}^2 (\vec{u} \cdot \vec{r}) (\vec{u} \times \vec{r}) \quad (6.5)$$

where  $V_{\text{NT}}$  is the SWNT effective volume,  $\epsilon_m$  is the dielectric constant of the liquid medium,  $K$  is the Clausius-Mossotti factor, and  $E_{\text{RMS}}$  is the root mean square electric field. The Clausius-Mossotti factor depends on the difference between complex dielectric functions of the particle and medium, and depolarization factors ( $L^{\parallel}$ ,  $L^{\perp}$ ) which take into account particle shape anisotropy [Mendes *et al.* 2008]. Collecting the length dependence of each term on the RHS of eq. 6.5 ( $V_{\text{NT}} \propto l_{\text{NT}}$ ,  $K \propto l_{\text{NT}}^2$ ,  $L^{\parallel}$  and  $L^{\perp} \propto 1/l_{\text{NT}}^2$  where  $l_{\text{NT}}$  is the length of SWNT), it can be shown that the rotational DEP force scales as  $l_{\text{NT}}^3$ .

The Brownian torque acting on the SWNT is a Gaussian random variable with zero mean and a second moment given by:

$$\langle M^B(t') M^B(t'') \rangle = 2k_B T \zeta^R \delta(t' - t'') \quad (6.6)$$



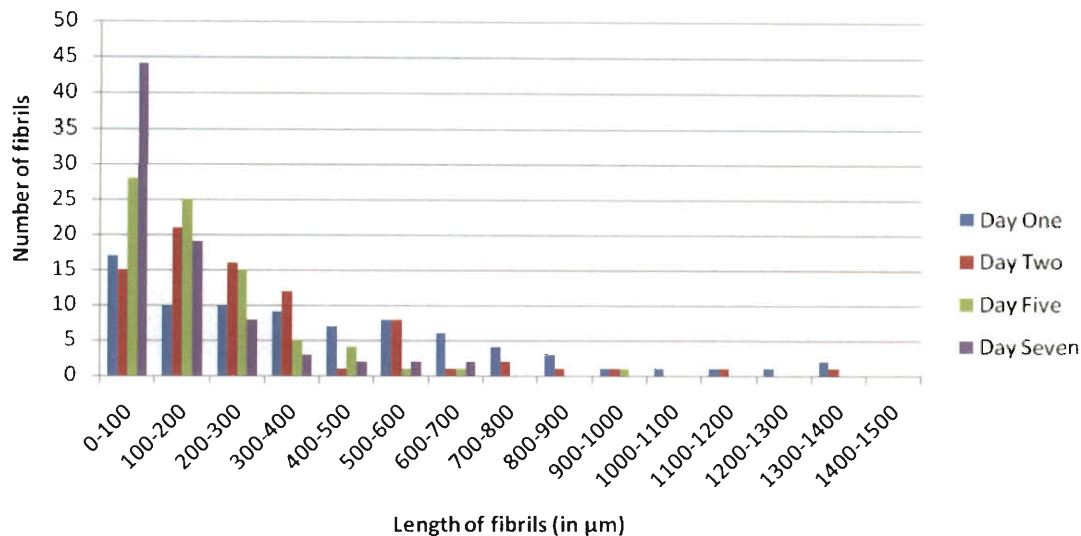


Figure 6.8 : Changes in the length distribution of mini-fibrils in a SWNT-DOC-NaCl suspension over time. The suspension was prepared by adding 0.05 M NaCl in 50 ppm SWNT-DOC (1 wt%) aqueous suspension. Liquid samples were withdrawn from the suspension at regular intervals and observed under a microscope to obtain the length distribution.

where  $k_B$  is the Boltzmann constant,  $T$  is the temperature, and  $\zeta^R$  is the rotational friction coefficient. Since the only particle length dependent term in the RHS of eq. 6.6 is  $\zeta^R$  ( $\zeta^R \propto l_{\text{NT}}^3$ ), the Brownian force scales with the length of the particle as

$$l_{\text{NT}}^{1.5}.$$

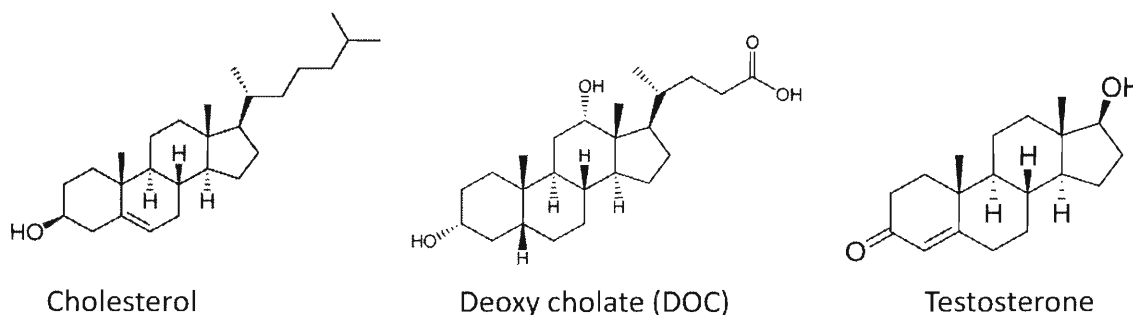


Figure 6.9 : Chemical structure of DOC, and structurally similar molecules: cholesterol and testosterone.

### 6.5.2 Changes in Length Distribution of Mini-Fibrils in Suspension Over Time

### 6.5.3 Dielectric Permittivity of Sodium Deoxycholate

We estimate the approximate complex dielectric permittivity of sodium deoxycholate (DOC) at room temperature (solid), around 1 MHz frequency, because an exact value for this quantity was not available from previous literature. We derived a reasonable value by considering the dielectric permittivity of structurally and functionally similar materials, as stated below.

- DOC being a bile salt is structurally similar to cholesterol (a steroid metabolite) and testosterone (steroid hormone), as shown in Fig. 6.9. The dielectric permittivity values (at 9.4 GHz) for these molecules are [Aruna and Behari 1981]:

$$\epsilon_{cholesterol}=1.828+i0.129 \text{ and } \epsilon_{testosterone}=1.709+i0.227$$

- The dielectric permittivity values for typical polymers over a wide range of frequencies is shown in Fig. 6.10. It can be readily observed that the dielectric constants for a wide range of polymers vary in between 2-12, in the MHz frequency regime. The values of permittivity in the MHz and GHz frequencies differ by less than 50% for each polymer.

Based on the above information, the complex dielectric permittivity of DOC was approximated to be  $\epsilon_{\text{DOC}}=2+i0.2$ .

#### **6.5.4 Thermo-gravimetric Analysis of Pure DOC**

Thermo-gravimetric analysis (TGA) of pure and dry surfactant DOC, performed under Argon flow and at a ramp rate of 10 °C/min using “SDT Q-600” by TA Instruments is shown in Fig. 6.11. The surfactant lost almost 80% of its weight by 450 °C.

Name	$t/^{\circ}\text{C}$	1 kHz	1 MHz	1 GHz
Polyacrylonitrile	25	5.5	4.2	
Polyamides (nylons)	25	3.50	3.14	2.8
	84	11	4.4	2.8
Polybutadiene	25	2.5		
Polycarbonate	23	2.92	2.8	
Polychloroprene (neoprene)	25	6.6	6.3	4.2
Polychlorotrifluoroethylene	23	2.65	2.46	2.39
Polyethylene	23	2.3		
Poly(ethylene terephthalate) (Mylar)	23	3.25	3.0	2.8
Polyisoprene (natural rubber)	27	2.6	2.5	2.4
Poly(methyl methacrylate)	27	3.12	2.76	2.6
	80	3.80	2.7	2.6
Polyoxymethylene (polyformaldehyde)	25	3.8		
Poly(phenylene oxide)	23	2.59	2.59	
Polypropylene	25	2.3	2.3	2.3
Polystyrene	25	2.6	2.6	2.6
Polysulfones	25	3.13	2.10	
Polytetrafluoroethylene (teflon)	25	2.1	2.1	2.1
	50		3.5	
Poly(vinyl acetate)	150		8.3	
	25	3.39	2.9	2.8
Poly(vinyl chloride)	100	5.3	3.3	2.7
	23	4.6	3.2	2.7
Poly(vinylidene chloride)	23	4.6	3.2	2.7
Poly(vinylidene fluoride)	23	12.2	8.9	4.7

Figure 6.10 : The dielectric permittivity values for typical polymers over a wide range of frequencies [Lide 2009].

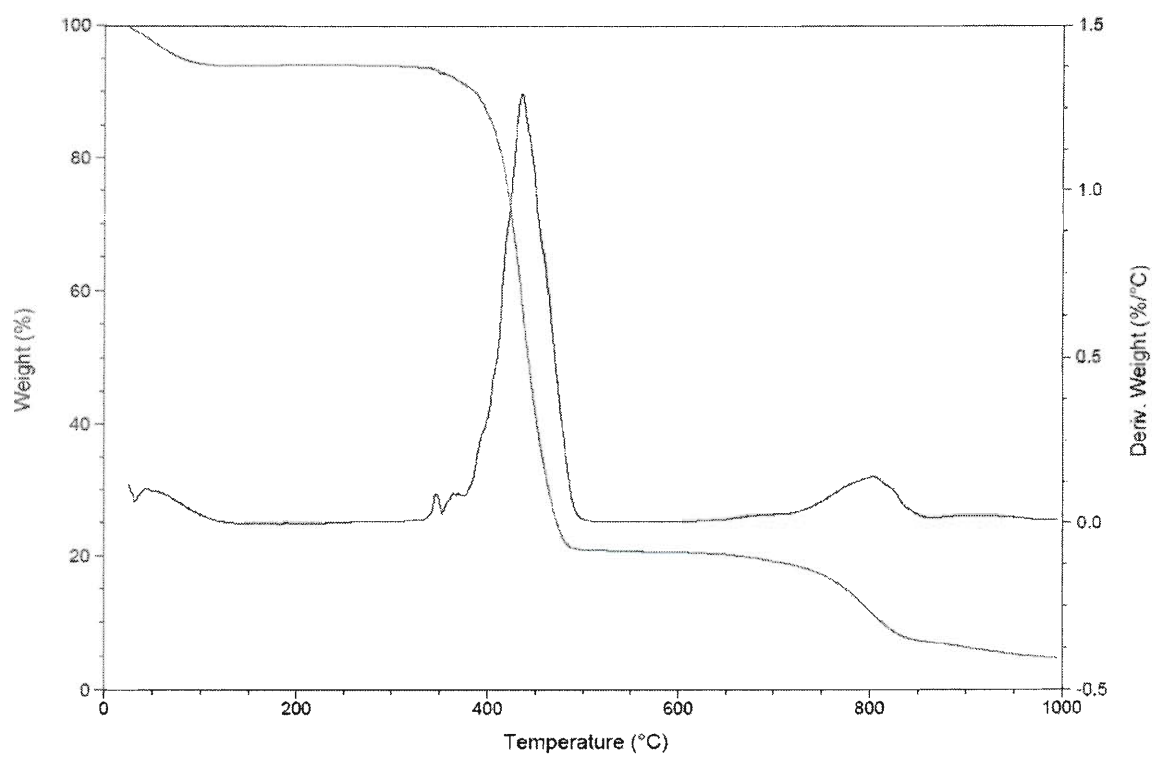


Figure 6.11 : Thermo-gravimetric analysis (TGA) of pure and dry surfactant DOC, performed under Argon flow and at a ramp rate of 10 °C/min.

## Chapter 7

# Liquid Crystalline Gel of Aqueous, Giant Graphene Oxide Flakes

### 7.1 Introduction

Colloidal suspensions of anisotropic particles have been the subject of continued research for over 100 years, owing to their rich variety of liquid crystalline phases and fascinating phase transitions [de Gennes and Prost 1995]. Initial studies on the orientational ordering, optical properties, response to external fields, and anisotropic elasticity of liquid crystals (LCs) were performed primarily on suspensions of rod-like particles [Bawden *et al.* 1936, Onsager 1949, Vroege and Lekkerkerker 1992, Zocher 1925]. In the seminal work on phase behavior and thermodynamic stability of mesophases, Onsager [1949] noted that liquid crystallinity is not restricted to only rod-like molecules, but should also extend to other anisotropic shapes, like disks and platelets. Experimental realization of disk and platelet LC systems, however, was achieved only three decades ago [Chandrasekhar *et al.* 1977] and has been a topic of

---

Part of this chapter has been submitted to *Nano Lett.* (2011) for publication. Part of this work was performed at Dept. of Physics and Liquid Crystal Materials Research Center, University of Colorado, Boulder, with Prof. Ivan Smalyukh.

intense research since then [Bisoyi and Kumar 2010, Chandrasekhar and Ranganath 1990].

The earliest observation of mesophases from disk-like molecules was in mid 1960's, during the high temperature carbonization of graphitizable substances like petroleum and coal tar pitches [Brooks and Taylor 1965]. Their complex, polydisperse composition, consisting of multicomponent polyaromatic molecules, likely impeded a detailed fundamental investigation of this naturally occurring "carbonaceous mesophase". The first experimental observation of discotic mesophase in a pure, single-component organic molecule system was reported in 1977 by Chandrasekhar et al. [1977]. They prepared a number of benzene-hexa-*n*-alkanoates, compounds with rigid aromatic cores and flexible aliphatic side chains, and established the existence of a new class of LCs named discotic LCs, from optical and X-ray data.

The ensuing three decades saw the development of more than 50 different organic cores and 3000 subsequent derivatives capable of forming discotic LCs [Bisoyi and Kumar 2010]. Most molecules are single atomic layer thin (thickness  $h < 1$  nm) and a few nanometers in diameter ( $D$ ), i.e., of typical aspect ratios  $D/h \sim 5$ . A majority of these aromatic-core based compounds demonstrate columnar discotic LC phases, where strong  $\pi - \pi$  interactions allow the disk-like molecules to assemble into cylindrical structures which in turn act as mesogens. A nematic mesophase, which is the prevalent mesophase observed in calamitic molecules, is not common among discotic

organic molecules [Dunmur *et al.* 2000]. Lyotropic LC phases have been observed in colloidal dispersions of inorganic platelets, often termed as “discotic mineral liquid crystals” [Gabriel and Davidson 2000, Sonin 1998, van der Kooij *et al.* 2000]. Isotropic to discotic nematic, and columnar LC phase transitions have been reported in dispersions of several mineral platelets including nickel hydroxide [Brown *et al.* 1999], gibbsite [van der Beek and Lekkerkerker 2003, van der Kooij and Lekkerkerker 1998] and layered double hydroxide [Liu and Kumar 2003, Mourad *et al.* 2008]. These mineral platelets are typically larger in size ( $D \sim$  hundreds of nanometers). However, an accompanying higher thickness often limits the highest achievable aspect ratio to only  $D/h \sim 20$ .

Recently, Behabtu *et al.* [Behabtu *et al.* 2010] reported the liquid crystallinity of graphene suspensions in chlorosulfonic acid at high graphene concentration (2 wt%), further expanding the range of systems forming discotic LCs. Observation of liquid crystalline ordering in graphene suspensions is exciting for several reasons: individualized graphene flakes represent atomically thin and extremely high aspect ratio ( $D/h \sim 10^4$ ) discotic particles which is closer to ideal theoretical models [Bates and Frenkel 1999, Eppenga and Frenkel 1984] but hasn’t been previously observed experimentally. From an applications point of view, spontaneous liquid crystalline ordering of graphene flakes may allow scalable processing into basic functional engineering materials, like wet spinning of high strength fibers [Davis *et al.* 2004, Ericson *et al.*



2004]. With its unique electronic properties, and extraordinary thermal and mechanical properties, graphene expands the realm of potential applications and the available variety of discotic LCs.

## 7.2 Phase Behavior of Giant Graphene Oxide Aqueous Suspensions

We explored the phase behavior of high aspect ratio ( $D/h \sim 10^4$ ) giant graphene oxide (GGO) flakes in an aqueous suspension. With increasing GGO concentration, we observe isotropic, biphasic and liquid crystalline phases. Various optical methods are employed to deduce the alignment of GGO flakes in the ordered phase, and to estimate the birefringence, order parameter and Frank elastic constant of this novel discotic LC system. Furthermore, LC defects are induced by use of controlled sample confinement geometries and elastic distortions are produced in the GGO director field by colloidal inclusions.

Studied GGO flakes were prepared by the method of Ref. [Marcano *et al.* 2010]. These monolayer GGO flakes have a more regular structure and larger continuous regions of intact basal plane, compared to GO produced using other conventional techniques like Hummer's method [Hummers and Offeman 1958]. Presence of functional groups like epoxy/hydroxyls, carbonyl, and carboxylate render the flakes hydrophilic.

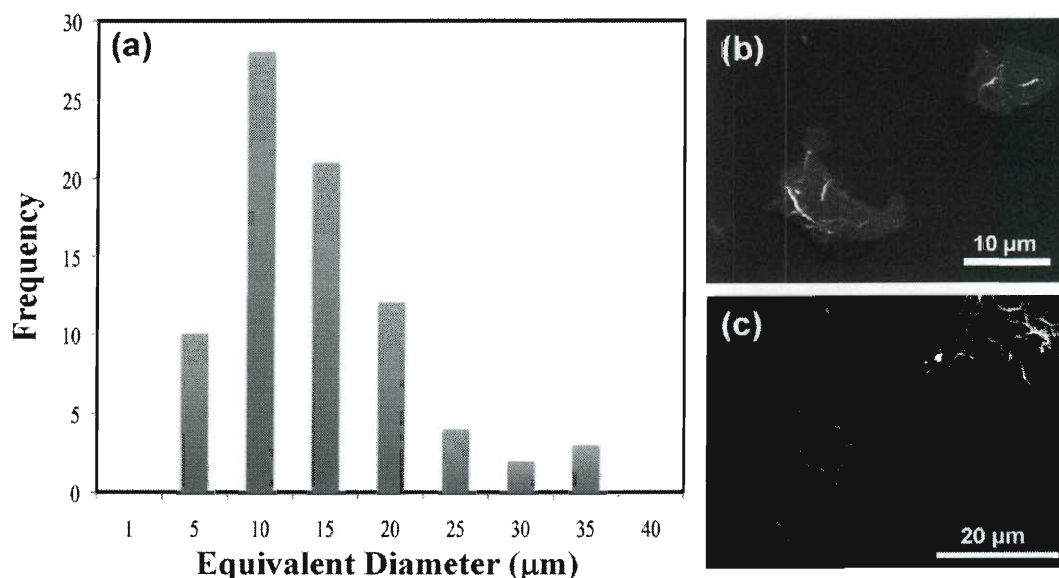


Figure 7.1 : (a) Size distribution of monolayer GGO flakes obtained through SEM and TEM imaging. (b,c) Representative SEM images of flakes deposited on silicon substrates by spin coating dilute aqueous GGO suspension.

The product was obtained as a concentrated aqueous suspension with known GGO concentration. Subsequent suspensions were prepared by evaporation or addition of desired amount of de-ionized (DI) water. The average size and polydispersity of GGO flakes was characterized using transmission electron microscopy (TEM) and scanning electron microscopy (SEM), as shown in Fig. 7.1(a). TEM samples were prepared on copper TEM grids as well as TEM grids covered with thin single-walled carbon nanotube (SWNT) membranes. Samples for SEM were prepared by spin coating a dilute GGO suspension on clean Silicon substrate; SEM images of typical GGO flakes are shown in Fig. 7.1(b-c).

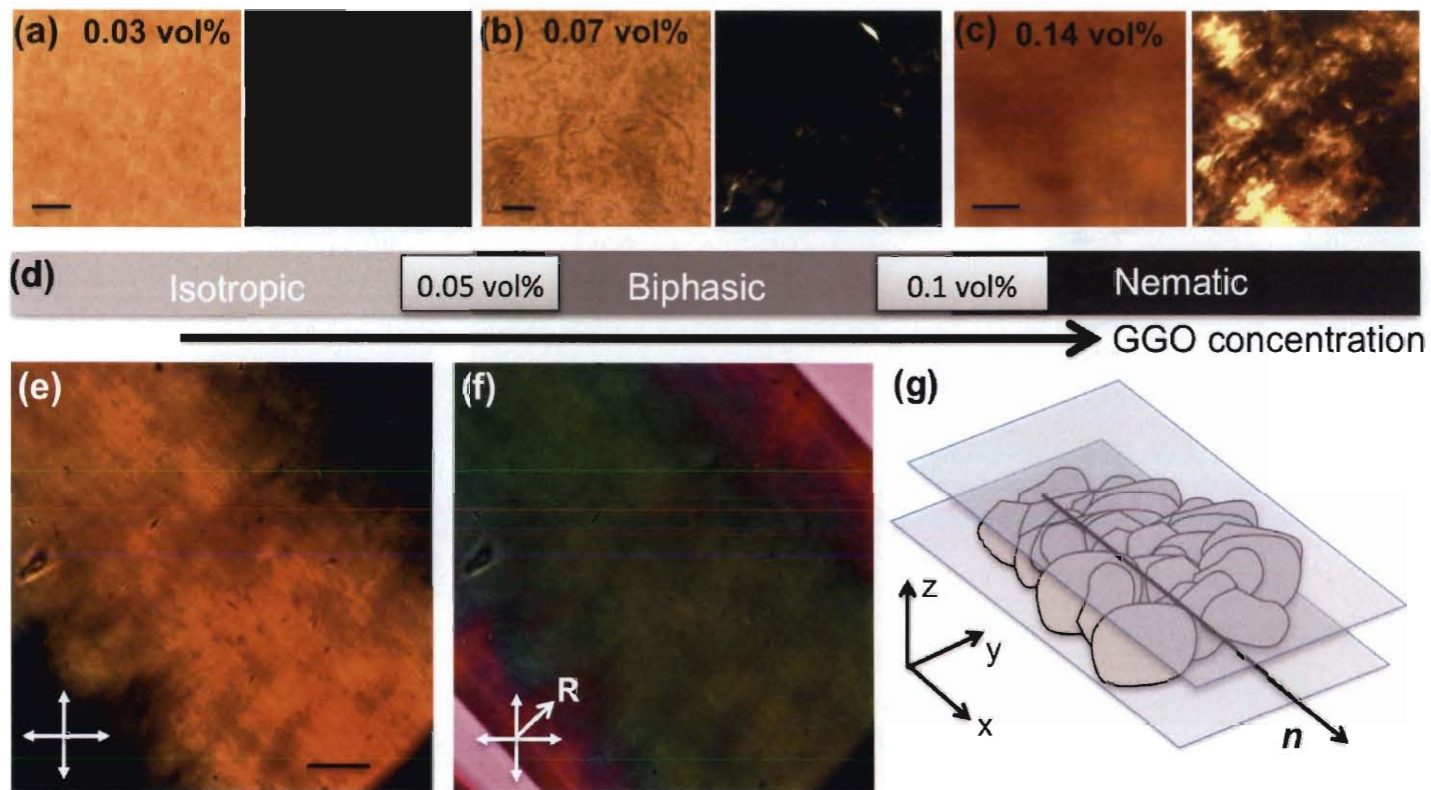


Figure 7.2 : (a-c) Optical micrographs obtained under transmission (left) and between crossed-polarizers (right) of GGO aqueous suspensions, demonstrating phase behavior vs. concentration: (a) isotropic (0.03 vol%), (b) biphasic (0.07 vol%) and (c) nematic (0.14 vol%). The scale bar in (a-c) is  $10 \mu\text{m}$ . (d) Phase behavior vs. concentration. (e,f) Polarizing microscopy images of GGO LC inside a  $100 \mu\text{m}$  capillary; uniform birefringence indicates uniform alignment of director over large length scales. The scale bar in (e) is  $20 \mu\text{m}$  and “R” in (f) marks the slow axis of the phase retardation plate. (g) Schematic showing the alignment of flakes.

The phase behavior of aqueous GGO suspension was investigated for concentration range 0.01-0.14 vol%. Drops from suspensions with different GGO concentration were squeezed between a cover slip and a glass slide whose edges were sealed with epoxy glue. These samples were examined using a transmission mode optical polarizing microscope (Olympus BX51) with 50x and 100x oil immersion objectives between crossed-polarizers. The dilute suspensions ( $< 0.05$  vol%; assuming density of GGO  $\sim 2000$  kg/m<sup>3</sup>) [Dikin *et al.* 2007] appeared dark and featureless under crossed-polarizers, as shown in Fig. 7.2(a). Lack of visible aggregates indicated a stable suspension. Suspensions with GGO concentration above  $\sim 0.05$  vol% displayed regions with weak birefringence, indicating onset of ordering and a biphasic system, Fig. 7.2(b). The fraction of ordered phase in the sample, as detected under crossed-polarizers, increased with GGO concentration. Above  $\sim 0.1$  vol%, the entire sample appeared birefringent at different stages of sample rotation under crossed-polarizers, indicating attainment of near single-phase liquid crystalline state, Fig. 7.2(c).

According to theoretical models, a colloidal system comprised of infinitely thin and monodisperse disk-like particles is expected to transition from isotropic to nematic at a volume fraction of  $\Phi_{\text{iso}} = 4 h/D$  [Bates and Frenkel 1999]. Because the average aspect ratio of our GGO flakes is  $D/h \sim 10^4$  (assuming monolayer GGO flakes have 1 nm effective thickness), the transition to ordered phase is expected to happen at 0.04 vol%, in good agreement with the experiments (Fig. 7.2(a-d)). Due to the

polydispersity in flake size, the ordered phase in our case begins as biphasic and approaches single-phase complete ordered state at higher concentrations.

The high concentration GGO suspensions had a gel-like consistency, leading to a smeared and non-uniform birefringent texture with current sample preparation method (Fig. 7.2(c)). Gelation has been observed previously in several other lyotropic discotic LC systems; most notably clay, whereby upon increasing the concentration, suspensions transition from an isotropic liquid to an isotropic gel to a birefringent gel [Gabriel *et al.* 1996, Mourchid *et al.* 1995; 1998]. By modifying the preparation procedure, uniformly aligned nematic domains of GGO were obtained, allowing further characterization and analysis of the GGO liquid crystalline state. Under this modified procedure, samples were prepared by dipping one end of a rectangular glass capillary tube (50  $\mu\text{m}$  thick and 0.5 mm wide inner dimensions, obtained from Vitrocom) in dilute isotropic GGO suspension ( $\sim 0.03$  vol%), causing spontaneous filling due to capillary action. Subsequent slow evaporation of water through the capillary ends led to concentration of GGO suspension. Once the sample starts showing birefringent texture, the tube ends were sealed with epoxy glue to prevent further drying.

Figure 7.2(e) shows an optical micrograph under crossed polarizers of a high concentration GGO suspension prepared using the improved procedure. Uniform brightness across the entire field of view indicates a well-aligned director ( $n$ ) over large

length scales (hundreds of microns or more). Moreover, it indicates that the normal of GGO flakes are oriented in the x-y plane of rectangular capillary, i.e., the flake plane is perpendicular to the wide top and bottom sides of capillary. Because the optical properties of GGO are isotropic in the flake plane, stacking parallel to the top and bottom sides of capillary will not produce any birefringence. The direction of in-plane orientation for GGO flakes was determined by inserting a “full wave retardation plate” ( $\lambda = 530$  nm) or “red plate” between the sample and analyzer, with its slow axis oriented at  $45^\circ$  to polarizer (i.e., along the capillary y-axis). For GGO, the axis along the basal plane represents slow axis while the normal to plane is the fast axis. Therefore, the appearance of bluish-green color (Fig. 7.2(f)), which in the case of GGO flakes (with negative birefringence) signifies addition of phase retardations of sample and red plate [Wahlstrom 1979], showing that the GGO flakes are also oriented along capillary y-axis (normal of flake points along capillary x-axis). Overall arrangement and orientation of GGO flakes and the nematic director in liquid crystal phase, as deduced from above analysis, is shown in Fig. 7.2(g).

Remarkably, uniform director orientation over  $\sim 1$  mm length scales was achieved without any surface treatment or pre-deposited alignment layer, which is typically required for small molecule LCs; this is an indication of high elasticity of GGO in LC phase. Indeed, according to density functional theory based models for nematic systems, the average Frank elastic constant ( $K$ ) of a nematogen can be expressed

as [Osipov and Hess 1993]:

$$K = \frac{1}{3}R_A Q^{\frac{2}{3}}(Q^{-2} + 2)S^2 \quad (7.1)$$

where  $R_A$  is a parameter determined by the direct correlation function of the nematic system,  $Q = D/h$  is the aspect ratio of nematogens, and  $S$  is the nematic scalar order parameter. For disk-shaped nematogens,  $Q \gg 1$  and the average elastic constant scales as  $K \propto Q^{\frac{2}{3}}$ . Previous experimental and computer simulation studies on various discotic nematics with average aspect ratio of  $Q \sim 5$  have reported average elastic constants on the order of 1 pN [Haven *et al.* 1981, Phuong *et al.* 2001, Tjiptomargo *et al.* 1992]. Because the elasticity coefficients of nematogens are mainly sensitive to the average molecular dimensions [Osipov and Hess 1993], the average elastic constant of GGO ( $Q \sim 10^4$ ) is expected to be  $K_{GGO} \sim 100$  pN, two orders of magnitude higher than most previously studied discotic nematics.

### 7.3 Optical Birefringence and Order Parameter

The highly uniform samples prepared in rectangular capillaries facilitated further characterization of liquid crystalline GGO and measurements of key properties like optical birefringence ( $\Delta n$ ) and order parameter ( $S$ ). The optical birefringence was measured with the aid of a Berek compensator. Measurements were performed at

several different locations, giving an average birefringence of  $\Delta n = -0.0017 \pm 0.0005$  for liquid crystalline GGO. In comparison, birefringence values of other discotic nematic systems from the literature are:  $-0.05$  for polyacrylates [FavreNicolin and Lub 1996],  $-0.02$  for DSCG (disodium cromoglycate),  $-0.01$  for violet-20 (chromonic LCs) [Nastishin *et al.* 2005].

The order parameter of GGO flakes in the nematic phase was estimated using optical absorption anisotropy, as described in Ref. [Nastishin *et al.* 2005]. Liquid crystalline GGO in a  $50 \mu\text{m}$  thick capillary was placed on microscope stage, between parallel polarizers, and illuminated with monochromatic green light. The transmittance through the sample was measured for director orientations of  $0^\circ$ ,  $45^\circ$ , and  $90^\circ$  with respect to the polarizers (referred to as  $t_0$ ,  $t_{45}$  and  $t_{90}$ , respectively). Corresponding absorption indices,  $k_0$ ,  $k_{45}$  and  $k_{90}$ , were obtained from the expression  $t_i = \exp(-4\pi k_i d/\lambda)$ , where  $i=0, 45, 90$  is index corresponding to director orientations of  $0^\circ$ ,  $45^\circ$ , and  $90^\circ$  respectively,  $\lambda = 550 \text{ nm}$  and  $d = 50 \mu\text{m}$ . For an ordered phase of disk-like molecules with the molecular planes oriented perpendicular to the director, if the shape of absorption spectrum is independent of molecular orientation and the birefringence is small (both conditions hold true for GGO), the scalar order parameter can be expressed as [Nastishin *et al.* 2005]:

$$S = \frac{1 - \Delta}{1 + \Delta/2} \quad (7.2)$$



where  $\Delta = k_0/k_{90}$  is the linear dichroic ratio. The above expression evaluated at several different locations on liquid crystalline GGO yielded an average order parameter of  $S = 0.43 \pm 0.15$ . In comparison, typical order parameter values measured in other small molecule liquid crystal systems include 0.9 for hexa-*n*-hexyloxy triphenylene [Chandrasekhar and Ranganath 1990], 0.6-0.85 for 2,3,7,8,12,13-hexa-*n*-decanoyloxytruxene (H10TX) and 2,3,6,7,10,11-hexa-*n*-pentyloxytriphenylene (H5T) [Perova and Vij 1995], 0.8 for gibbsite particles [van der Beek *et al.* 2008].

The optical absorption anisotropy measurement provides an independent estimate of the birefringence of the sample. The phase retardation of transmitted light traversing through an anisotropic sample is [Nastishin *et al.* 2005]:

$$\Delta\varphi = \cos^{-1} \left( \frac{4t_{45} - (t_0 + t_{90})}{2\sqrt{t_0 t_{90}}} \right) \quad (7.3)$$

The phase retardation is related to optical birefringence as  $\Delta n = \Delta\varphi\lambda/2\pi d$ . Calculations using this method yielded an optical birefringence of  $\Delta n = -0.0018 \pm 0.0009$ , in good agreement with the value obtained via Berek compensator measurements.

## 7.4 Anisotropic Particle Inclusions and LC Defects

Anisotropic colloidal inclusions are valuable probes for direct visualization of the stacking, orientation and alignment of GGO in the nematic phase. Two types of

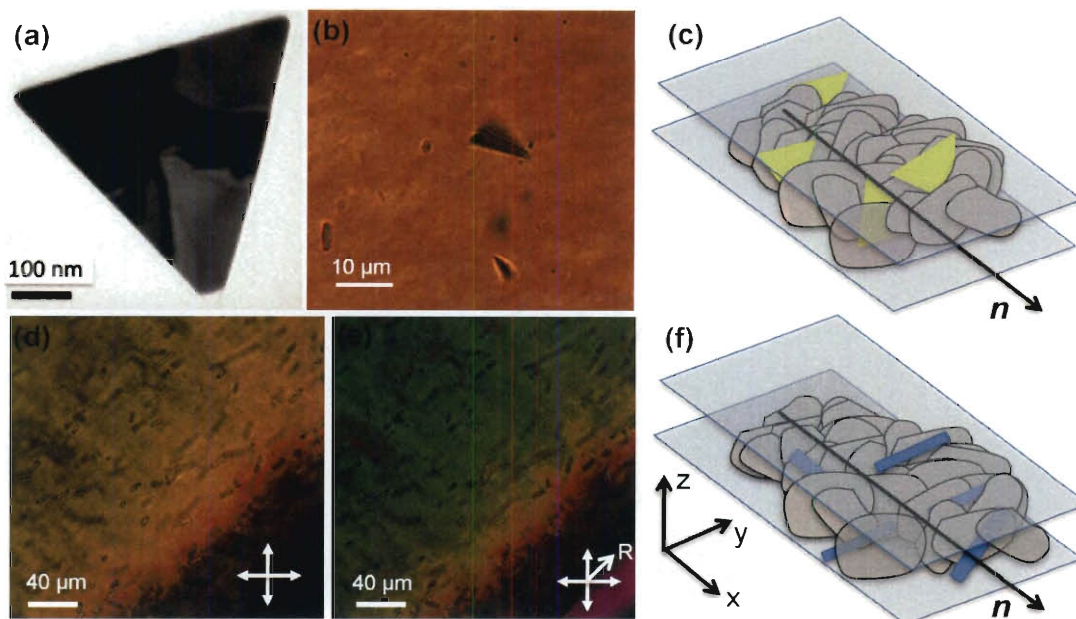


Figure 7.3 : Anisotropic colloidal particles and their spontaneous alignment in GGO nematic LC. (a) TEM image of an anisotropic gold triangular platelet. (b) Bright-field transmission-mode image showing triangular platelets with up to  $10\ \mu\text{m}$  side length and  $5\ \text{nm}$  thickness as they spontaneously align parallel to GGO flakes of the LC. (c) Schematic diagram of the GGO flake and gold platelet alignment. (d-f) Polarizing microscopy images showing spontaneous alignment of glass micro-rods in the GGO LC observed under crossed polarizers with (d) and without (e) an additional retardation plate. (f) Schematic showing the alignment of micro-rods in the LC.

particles were chosen for this purpose: Gold microtriangles, 5 nm in thickness and up to 10  $\mu\text{m}$  side length (Fig. 7.3(a)), prepared using a biosynthesis technique,[ref: Julian paper] and glass micro-rods, 3  $\mu\text{m}$  diameter and 10  $\mu\text{m}$  long (from Duke Scientific). Small size ( $< 3 \mu\text{m}$ ) in at least one dimension allows the particles to intercalate into the nematic phase while distorting only minimally the director field; larger size in other dimensions allows easy detection with optical microscopy. Remarkably, gold microtriangles spontaneously oriented inside the GGO nematic phase with their plane perpendicular to the  $n$  (and parallel to GGO flakes), shown in Fig. 7.3(b-c). This provides further evidence for the axial orientation of GGO flakes, deduced previously from crossed-polarized optical images. Anisotropic glass micro-rods, on the other hand, spontaneously aligned with their long axis perpendicular to the  $n$  and parallel to the GGO flakes, as shown in Fig. 7.3(d,e,f). The ability of GGO liquid crystal to disperse and align anisotropic colloidal particles is important from applications perspective. For example, the large scale ordering and alignment of anisotropic plasmonic nanoparticles, like gold, silver and palladium nanorods, by means of dispersion in a LC is a valuable route for development of optoelectronic devices and metamaterials [Liu *et al.* 2010].

Given the natural propensity of our GGO flakes to form large domains with uniform director field, the capillary drying method rarely produced defective structure. In order to induce defects, drops of dilute GGO suspension with circular cross-section

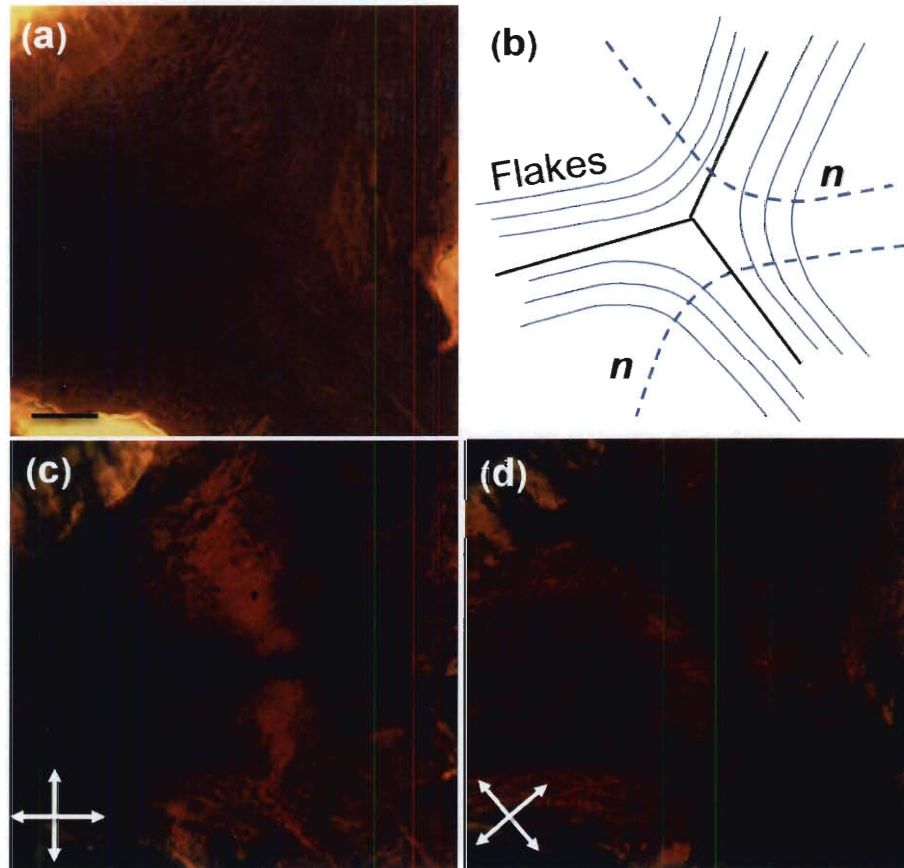


Figure 7.4 : A half-integer  $s = -1/2$  disclination in the director field of GGO LC observed when nematic phase is obtained by solvent evaporation under the confinement of a glass slide and cover slip. (a) Transmission-mode bright-field image. (b) Schematic of the arrangement of GGO flakes. (c,d) Polarizing microscopy images of the same region obtained (c) between vertical and horizontal crossed polarizers and (d) with crossed-polarizers at  $45^\circ$  and  $135^\circ$  with respect to horizontal side of the image. The scale bar is  $20 \mu\text{m}$  for all images.

were trapped between a glass slide and cover slip separated by  $60\ \mu\text{m}$  spacers and allowed to evaporate slowly to achieve a nematic phase. In such a setup, recession of the meniscus from all directions forces the creation of a defect at the center of drop. Interestingly, in most cases, the circular drops transformed into roughly Y-shaped structures as the drop radii became sufficiently small. The optical transmission image of an  $s = -1/2$  defect, observed at the center of such Y-shaped nematic structures, is shown in Fig. 7.4(a). The transformation of drop shape during drying and formation of observed defects can be understood in terms of the high elastic constant of GGO nematogens: the Y-shaped structure involves considerably lower bend compared to a circular shape of same area and a radial hedgehog defect at the center. The arrangement of GGO flakes and director field around the defect is shown schematically in Fig. 7.4(b). Figures 7.4(c - d) show the defect structure with crossed-polarizers in  $0^\circ$ - $90^\circ$  and at  $45^\circ$ - $135^\circ$  position, respectively; dark brushes, parallel to one of the polarizers, and characteristic of these defect patterns can be observed.

## 7.5 Colloidal Inclusions and Elastic Distortions

The strong orientational order and associated anisotropic elasticity in LCs gives rise to a host of intriguing fluid properties, which are interesting from fundamental scientific as well as application perspectives [Lavrentovich *et al.* 2010]. A common way of probing the elastic response of such a system, to gain insights into its vis-

coelastic properties at length scales typically inaccessible by bulk methods, is by inclusion of colloidal particles of varying sizes. For example, Poulin et al. [Poulin *et al.* 1999] demonstrated that colloidal spheres suspended in nematic solutions lead to dipolar and quadrupolar distortions in the surrounding director field. The drive to minimize the ensuing elastic stress results in spontaneous assembly of colloidal particles into anisotropic structures. Polygonal platelets have also been used to explore shape-dependent elasticity mediated interactions, alignment, and self-assembly in anisotropic fluids [Lapointe *et al.* 2004; 2009].

The elastic response of GGO liquid crystal was probed by inclusion of melamine resin colloidal microspheres, with diameters ranging from 2  $\mu\text{m}$  to 15  $\mu\text{m}$ . The microspheres were incorporated in the LC by mixing tiny quantities of aqueous microsphere suspensions in dilute GGO suspension, followed by capillary filling and solvent evaporation. The hydrophilic nature of melamine resin allowed easy incorporation into the aqueous GGO suspension without additional surfactants or stabilizing agents. The range of microsphere diameters explored in our experiments was restricted by optical detection (as a lower bound) and capillary size (as an upper bound). Interestingly, small diameter particles ( $< 3 \mu\text{m}$ ) did not produce any distinguishable distortions in the nematic director field, as shown by transmission and crossed-polarized images in Fig. 7.5(a). Larger diameter particles (4  $\mu\text{m}$ , 7  $\mu\text{m}$  and 15  $\mu\text{m}$ ) produced distinct quadrupolar distortions in the GGO nematic director field; the size of the distortions

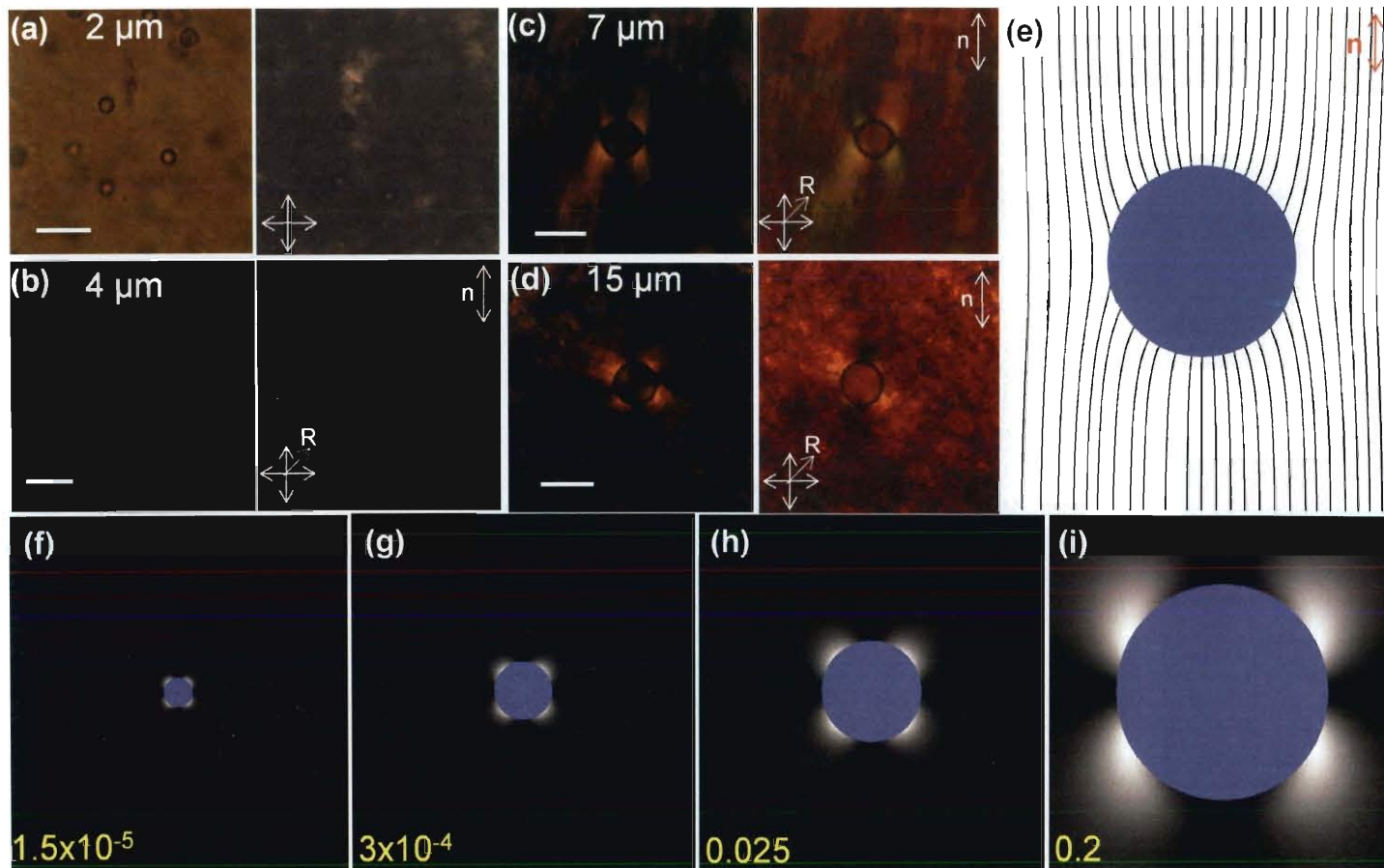


Figure 7.5 : Quadrupolar distortions in nematic director field around melamine resin microsphere inclusions, demonstrating “homeotropic” or “normal” surface anchoring of the director (i.e., GGO flakes are tangential to the particle surface). (a) Transmission-mode (left) and between crossed polarizers (right) images of GGO LC. (b-d) Images of sample between crossed-polarizers (left) and with a retardation plate (right). Scale bars are  $10\ \mu\text{m}$  (a),  $5\ \mu\text{m}$  (b),  $10\ \mu\text{m}$  (c),  $20\ \mu\text{m}$  (d). Particle sizes, and orientations of crossed polarizers and retardation plates marked on the images. Computer-simulated (e) director field and (f-i) polarizing microscopy textures for particle sizes 2, 4, 7, and  $15\ \mu\text{m}$ , respectively. The values shown in (f-i) in yellow color are the ratios of maximum transmitted and incident light intensities for the corresponding computer-simulated images.

grew with the size of particles, as shown by images between crossed-polarizers and inserted full retardation plate in Fig. 7.5(b - d). Optical analysis on the four lobes of each quadrupolar distortion using red plate revealed a “normal” or “homeotropic” surface anchoring for  $n$ , i.e., GGO flakes exhibit tangential alignment to the melamine resin particles. The orientation of GGO flakes around melamine resin particles is likely influenced by favorable acid-base interactions between the  $-\text{NH}_2$  and  $=\text{N}-$  groups on melamine resin and acidic hydrophilic functional groups on GGO flakes.

Because of anisotropic interactions at the interface, colloidal inclusions in nematic LCs can either induce various types of defects in the director field or barely perturb it, depending on the interplay of the competition of bulk elastic and surface anchoring energies [Lapointe *et al.* 2004; 2009, Lavrentovich *et al.* 2010, Liu *et al.* 2010, Poulin and Weitz 1998, Poulin *et al.* 1999, Smalyukh *et al.* 2006]. For example, a spherical colloidal inclusion with homeotropic boundary conditions induces a pattern of director equivalent to that around a point defect with charge  $+1$ , known as “radial hedgehog”. Therefore, another point or line defect of equal and opposite charge should accompany the distortions around the particle, in order to conserve the total topological charge in the sample with a uniform far-field alignment [Smalyukh *et al.* 2006]. Therefore, microparticles with a strong homeotropic anchoring produce a hyperbolic hedgehog or a half-integer “Saturn ring” disclination loop, both having topological charge of  $-1$ . On the other hand, nanoparticles of size only somewhat larger than that of the



LC molecules and microparticles with weak surface anchoring typically produce either weak or no elastic distortions of the LC director field [Liu *et al.* 2010]. In the case of melamine resin particles suspended in GGO LC, no accompanying topological defects are observed. The director distortions have quadrupolar symmetry, reminiscent of that formed around microparticles with weak homeotropic surface anchoring, suggesting that  $K/W > R$ , where  $R$  is the particle radius and  $W$  is the polar surface anchoring coefficient [Ruhwandl and Terentjev 1997a;b]. Equivalently, the nematic director at the LC-colloid interface deviates from the normal orientation (Fig. 7.5(e)), in order to minimize elastic distortions and reduce the elastic energy at the expense of surface anchoring energy cost. The director distortions become less pronounced as  $R$  decreases, being barely noticeable for the  $2 \mu\text{m}$  particles.

We simulated the expected nematic director structure surrounding the particles and corresponding polarizing microscopy textures. We use the *ansatz* for LC director structure proposed by Ruhwandl and Terentjev [Ruhwandl and Terentjev 1997a;a] (Fig. 7.5(e)) and the Jones matrix method [Yeh and Gu 1999] to simulate the polarizing microscopy textures. The simulations used experimentally estimated values of the elastic constant  $K = 10^{-10}$  N, optical anisotropy  $\Delta n = -0.0017$  and a polar anchoring coefficient of  $W = 10^{-5}$  J/m<sup>2</sup>, typical of lyotropic discotic systems [Subacius *et al.* 1995]. The LC sample, with a colloidal inclusion and director distortions around it, was split into a set of thin slabs with known orientation of the optical axis (= LC

director). In each pixel of a simulated polarizing microscopy texture (similar to those in Fig. 7.5(f-i)), propagation through the cell was obtained by successive multiplication of the Jones matrices corresponding to a polarizer, the thin nematic slabs, and the analyzer. The computer simulated textures thus obtained, correlated closely with the experimental results (Fig. 7.5). Interestingly, although the particle diameters and the lateral GGO flake sizes are comparable, the director structures around the colloidal inclusions still can be understood based on simple considerations developed for small-molecule LCs.

The melamine resin microspheres suspended in GGO LC are practically immobile and do not show any tendency to self-assemble into anisotropic structures, even at long time scales (several days), as has been reported in other nematic systems [Poulin and Weitz 1998]. This is unexpected for anisotropic nematic fluids, as the distortions induced by the particles and high elastic constant of GGO are expected to induce strong inter-particle forces and guide the formation of particle assemblies that minimize the cost to the nematic's free energy. The lack of particle motions and any noticeable interaction among the microspheres indicates a gel-like networked structure among the flakes at high GGO concentrations. Future studies are needed to decipher the nature of the forces responsible for the interlinked network formation.

## 7.6 Conclusions

We have shown that, with increasing concentration, giant (several micrometers) GGO flakes form well defined isotropic, biphasic and gel-like nematic LC phases. Preparation of the nematic phase by slow evaporation of solvent from the isotropic phase yields large domains with uniform director and minimal distortions and defects, indicating a high elastic constant of nematogens. Inclusion of melamine resin spherical colloidal particles causes the GGO flakes to align parallel to the particle's surface (i.e., homeotropic director anchoring) and well defined quadrupolar distortions in the surrounding nematic field. A similar, preferentially tangential alignment of GGO flakes to anisotropic gold microtriangles and glass micro-rods allowed direct visualization of the stacking and orientation of GGO flakes in the nematic ordered phase. The observed liquid crystalline behavior from this new class of extremely high aspect ratio ( $\sim 10^4$ ) disk like molecules should allow further fundamental studies in the unexplored regimes of discotic nematic LCs. The unique structure and superior electro-optical properties of GGO are poised to add a new dimension to currently existing applications of discotic nematics and potentially unravel new applications.

## Bibliography

- Annamalai R., West J. D., Luscher A., and Subramaniam V. V. (2005) Electrophoretic drawing of continuous fibers of single-walled carbon nanotubes. *Journal of Applied Physics* **98** [No. 11] 6.
- Armitage N. P., Gabriel J. C. P., and Gruner G. (2004) Quasi-langmuir-blodgett thin film deposition of carbon nanotubes. *Journal of Applied Physics* **95** [No. 6] 3228–3230.
- Arnold M., Green A., Hulvat J., Stupp S., and Hersam M. (2006) Sorting Carbon Nanotubes by Electronic Structure using Density Differentiation. *Nature nanotechnology* **1** [No. 1] 60–65.
- Aruna R. and Behari J. (1981) Dielectric Loss in Biogenic Steroids at Microwave Frequencies. *IEEE Transactions on Microwave Theory and Techniques* **29** [No. 11] 1209–1213.
- Atwater H. A. and Polman A. (2010) Plasmonics for improved photovoltaic devices. *Nature Materials* **9** [No. 3] 205–213.

- Bachilo S. M., Strano M. S., Kittrell C., Hauge R. H., Smalley R. E., and Weisman R. B. (2002) Structure-assigned optical spectra of single-walled carbon nanotubes. *Science* **298** [No. 5602] 2361–2366.
- Badaire S., Pichot V., Zakri C., Poulin P., Launois P., Vavro J., Guthy C., Chen M., and Fischer J. E. (2004) Correlation of properties with preferred orientation in coagulated and stretch-aligned single-wall carbon nanotubes. *Journal of Applied Physics* **96** [No. 12] 7509–7513.
- Badaire S., Zakri C., Maugey M., Derre A., Barisci J. N., Wallace G., and Poulin P. (2005) Liquid crystals of dna-stabilized carbon nanotubes. *Advanced Materials* **17** [No. 13] 1673–1676.
- Basu R. and Iannacchione G. S. (2009) Nematic anchoring on carbon nanotubes. *Applied Physics Letters* **95** [No. 17].
- Bates M. A. and Frenkel D. (1999) Nematic-isotropic transition in polydisperse systems of infinitely thin hard platelets. *Journal of Chemical Physics* **110** [No. 13] 6553–6559.
- Baughman R. H., Zakhidov A. A., and de Heer W. A. (2002) Carbon nanotubes—the route toward applications. *Science* **297** [No. 5582] 787–792.

- Bawden F. C., Pirie N. W., Bernal J. D., and Fankuchen I. (1936) Liquid crystalline substances from virusinfected plants. *Nature* **138** 1051–1052.
- Behabtu N., Green M. J., and Pasquali M. (2008) Carbon nanotube-based neat fibers. *Nano Today* **3** [No. 5-6] 24–34.
- Behabtu N., Lomeda J. R., Green M. J., Higginbotham A. L., Sinitiskii A., Kosynkin D. V., Tsentelovich D., Parra-Vasquez A. N. G., Schmidt J., Kesselman E., Cohen Y., Talmon Y., Tour J. M., and Pasquali M. (2010) Spontaneous high-concentration dispersions and liquid crystals of graphene. *Nature Nanotechnology* **5** [No. 6] 406–411.
- Berli C. L. A., Quemada D., and Parker A. (2002) Modelling the viscosity of depletion flocculated emulsions. *Colloids Surf., A* **203** [No. 1-3] 11–20.
- Bethune D., Klang C., De Vries M., Gorman G., Savoy R., Vazquez J., and Beyers R. (1993) Cobalt-Catalysed Growth of Carbon Nanotubes with Single-Atomic-Layer Walls. *Nature* **363** 605–607.
- Bisoyi H. K. and Kumar S. (2010) Discotic nematic liquid crystals: science and technology. *Chemical Society Reviews* **39** [No. 1] 264–285.
- Booker R., Green M., Fan H., Parra-Vasquez A., Behabtu N., Young C., Hauge R., Schmidt H., Smalley R., and Hwang W. (2008) High-shear treatment of single-

- walled carbon nanotube-superacid solutions as a pre-processing technique for the assembly of fibres and films. *Proceedings of the Institution of Mechanical Engineers, Part N: Journal of Nanoengineering and Nanosystems* **222** [No. 3] 101–109.
- Bradac Z., Kralj S., and Zumer S. (2002) Molecular dynamics study of the isotropic-nematic quench. *Physical Review E* **65** [No. 2].
- Bronikowski M. J., Willis P. A., Colbert D. T., Smith K. A., and Smalley R. E. (2001) Gas-phase production of carbon single-walled nanotubes from carbon monoxide via the hipco process: A parametric study. *Journal of Vacuum Science & Technology a-Vacuum Surfaces and Films* **19** [No. 4] 1800–1805.
- Brooks J. D. and Taylor G. H. (1965) Formation of graphitizing carbons from liquid phase. *Nature* **206** [No. 4985] 697–699.
- Brown A. B. D., Ferrero C., Narayanan T., and Rennie A. R. (1999) Phase separation and structure in a concentrated colloidal dispersion of uniform plates. *European Physical Journal B* **11** [No. 3] 481–489.
- Cates M. E. and Candau S. J. (1990) Statics and dynamics of worm-like surfactant micelles. *Journal of Physics-Condensed Matter* **2** [No. 33] 6869–6892.
- Chandran S. P., Chaudhary M., Pasricha R., Ahmad A., and Sastry M. (2006) Syn-

- thesis of gold nanotriangles and silver nanoparticles using aloe vera plant extract. *Biotechnology Progress* **22** [No. 2] 577–583.
- Chandrasekhar S. and Ranganath G. S. (1990) Discotic liquid-crystals. *Reports on Progress in Physics* **53** [No. 1] 57–84.
- Chandrasekhar S., Sadashiva B. K., and Suresh K. A. (1977) Liquid-crystals of disc-like molecules. *Pramana* **9** [No. 5] 471–480.
- Chen X. M., Hamlington B. D., and Shen A. Q. (2008) Isotropic-to-nematic phase transition in a liquid-crystal droplet. *Langmuir* **24** [No. 2] 541–546.
- Choi H., Shim M., Bangsaruntip S., and Dai H. (2002) Spontaneous Reduction of Metal Ions on the Sidewalls of Carbon Nanotubes. *Journal of American Chemical Society* **124** [No. 31] 9058–9059.
- Choi W. B., Chung D. S., Kang J. H., Kim H. Y., Jin Y. W., Han I. T., Lee Y. H., Jung J. E., Lee N. S., and Park G. S. (1999) Fully sealed, high-brightness carbon-nanotube field-emission display. *Applied physics letters* **75** 3129.
- Chopra K. L., Major S., and Pandya D. K. (1983) Transparent conductors– a status review. *Thin Solid Films* **102** [No. 1] 1–46.
- Cohen E. and Gutoff E. Modern coating and drying technology. In Cohen E., editor, *Choosing the Coating Method* pages 6–7. VCH Publishers New York (1992).



- Correa-Duarte M. A., Perez-Juste J., Sanchez-Iglesias A., Giersig M., and Liz-Marzan L. M. (2005) Aligning an nanorods by using carbon nanotubes as templates. *Angewandte Chemie-International Edition* **44** [No. 28] 4375–4378.
- Coyle D. J., Macosko C. W., and Scriven L. E. (1990) Reverse roll coating of non-newtonian liquids. *Journal of Rheology* **34** 615.
- Dai H., Franklin N., and Han J. (1998) Exploiting the properties of carbon nanotubes for nanolithography. *Applied Physics Letters* **73** 1508.
- Dan B., Irvin G. C., and Pasquali M. (2009) Continuous and scalable fabrication of transparent conducting carbon nanotube films. *ACS Nano* **3** [No. 4] 835–843.
- Dan B., Wingfield T., Evans J., Mirri F., Pint C., Pasquali M., and Smalyukh I. (2011, submitted) Spontaneous ordering of gold nanoparticles on highly aligned swnt macrostructures. *ACS Nano*.
- Daniel M. C. and Astruc D. (2004) Gold nanoparticles: Assembly, supramolecular chemistry, quantum-size-related properties, and applications toward biology, catalysis, and nanotechnology. *Chemical Reviews* **104** [No. 1] 293–346.
- Davis V., Ericson L., Parra-Vasquez A., Fan H., Wang Y., Prieto V., Longoria J., Ramesh S., Saini R., Kittrell C., and others . (2004) Phase behavior and rheology of SWNTs in superacids. *Macromolecules* **37** [No. 1] 154–160.

Davis V. A., Parra-Vasquez A. N. G., Green M. J., Rai P. K., Behabtu N., Prieto V., Booker R. D., Schmidt J., Kesselman E., Zhou W., Fan H., Adams W. W., Hauge R. H., Fischer J. E., Cohen Y., Talmon Y., Smalley R. E., and Pasquali M. (2009) True solutions of single-walled carbon nanotubes for assembly into macroscopic materials. *Nature Nanotechnology* **4** [No. 12] 830–834.

de Gennes P. and Prost J. *The physics of liquid crystals*. Oxford University Press, USA (1995).

Dikin D. A., Stankovich S., Zimney E. J., Piner R. D., Dommett G. H. B., Evmnenko G., Nguyen S. T., and Ruoff R. S. (2007) Preparation and characterization of graphene oxide paper. *Nature* **448** [No. 7152] 457–460.

Dinsmore A. D., Yodh A. G., and Pine D. J. (1996) Entropic control of particle motion using passive surface microstructures. *Nature* **383** [No. 6597] 239–242.

Doherty E., De S., Lyons P., Shmeliov A., Nirmalraj P., Scardaci V., Joimel J., Blau W., Boland J., and Coleman J. (2009) The Spatial Uniformity and Electromechanical Stability of Transparent, Conductive Films of Single Walled Nanotubes. *Carbon* **47** [No. 10] 2466–2473.

Dressel M. and Gruner G. *Electrodynamics of Solids*. Cambridge University Press New York (2002).

- Dresselhaus M., Dresselhaus G., Saito R., and Jorio A. (2005) Raman Spectroscopy of Carbon Nanotubes. *Physics Reports* **409** [No. 2] 47–99.
- Duggal R. and Pasquali M. (2006) Dynamics of individual single-walled carbon nanotubes in water by real-time visualization. *Physical Review Letters* **96** [No. 24].
- Dunmur D., Fukuda A., Luckhurst G., and Engineers I. o. E. *Physical properties of liquid crystals: nematics*. INSPEC (2000).
- Duque J. G., Parra-Vasquez A. N. G., Behabtu N., Green M. J., Higginbotham A. L., Price B. K., Leonard A. D., Schmidt H. K., Lounis B., Tour J. M., Doorn S. K., Cognet L., and Pasquali M. (2010) Diameter-dependent solubility of single-walled carbon nanotubes. *ACS Nano* **4** [No. 6] 3063–3072.
- Durr N. J., Larson T., Smith D. K., Korgel B. A., Sokolov K., and Ben-Yakar A. (2007) Two-photon luminescence imaging of cancer cells using molecularly targeted gold nanorods. *Nano Letters* **7** [No. 4] 941–945.
- Ebbesen T. W. and Ajayan P. M. (1992) Large-scale synthesis of carbon nanotubes. *Nature* **358** [No. 6383] 220–222.
- Eppenga R. and Frenkel D. (1984) Monte-carlo study of the isotropic and nematic phases of infinitely thin hard platelets. *Molecular Physics* **52** [No. 6] 1303–1334.

Ericson L. M., Fan H., Peng H. Q., Davis V. A., Zhou W., Sulpizio J., Wang Y. H., Booker R., Vavro J., Guthy C., Parra-Vasquez A. N. G., Kim M. J., Ramesh S., Saini R. K., Kittrell C., Lavin G., Schmidt H., Adams W. W., Billups W. E., Pasquali M., Hwang W. F., Hauge R. H., Fischer J. E., and Smalley R. E. (2004) Macroscopic, neat, single-walled carbon nanotube fibers. *Science* **305** [No. 5689] 1447–1450.

FavreNicolin C. D. and Lub J. (1996) Stable anisotropic films obtained by in-situ photopolymerization of discotic liquid crystalline acrylates. *Macromolecules* **29** [No. 19] 6143–6149.

Fonck E., Feigl G. G., Fasel J., Sage D., Unser M., Rufenacht D. A., and Stergiopoulos N. (2009) Effect of aging on elastin functionality in human cerebral arteries. *Stroke* **40** [No. 7] 2552–2556.

Fraser D. B. and Cook H. D. (1972) Highly conductive, transparent films of sputtered insno. *Journal of Electrochemical Society* **119** 1368.

Fu W. Q., Liu L., Jiang K. L., Li Q. Q., and Fan S. S. (2010) Super-aligned carbon nanotube films as aligning layers and transparent electrodes for liquid crystal displays. *Carbon* **48** [No. 7] 1876–1879.

Fuhrer M., Nygård J., Shih L., Forero M., Yoon Y., Mazzoni M., Choi H., Ihm J.,

- Louie S., Zettl A., and McEuen P. L. (2000) Crossed Nanotube Junctions. *Science* **288** [No. 5465] 494.
- Gabriel J. C. P. and Davidson P. (2000) New trends in colloidal liquid crystals based on mineral moieties. *Advanced Materials* **12** [No. 1] 9–20.
- Gabriel J. C. P., Sanchez C., and Davidson P. (1996) Observation of nematic liquid-crystal textures in aqueous gels of smectite clays. *Journal of Physical Chemistry* **100** [No. 26] 11139–11143.
- Geng H. Z., Kim K. K., So K. P., Lee Y. S., Chang Y., and Lee Y. H. (2007) Effect of acid treatment on carbon nanotube-based flexible transparent conducting films. *Journal of American Chemical Society* **129** [No. 25] 7758–7759.
- Girishkumar G., Vinodgopal K., and Kamat P. V. (2004) Carbon nanostructures in portable fuel cells: Single-walled carbon nanotube electrodes for methanol oxidation and oxygen reduction. *Journal of Physical Chemistry B* **108** [No. 52] 19960–19966.
- Gommans H. H., Alldredge J. W., Tashiro H., Park J., Magnuson J., and Rinzler A. G. (2000) Fibers of aligned single-walled carbon nanotubes: Polarized raman spectroscopy. *Journal of Applied Physics* **88** [No. 5] 2509–2514.
- Granqvist C. G. and Hultker A. (2002) Transparent and conducting ito films: New developments and applications. *Thin Solid Films* **411** [No. 1] 1–5.

- Green A. A. and Hersam M. C. (2008) Colored semitransparent conductive coatings consisting of monodisperse metallic single-walled carbon nanotubes. *Nano Letters* **8** [No. 5] 1417–1422.
- Green M. J., Parra-Vasquez A. N. G., Behabtu N., and Pasquali M. (2009) Modeling the phase behavior of polydisperse rigid rods with attractive interactions with applications to single-walled carbon nanotubes in superacids. *Journal of Chemical Physics* **131** [No. 8].
- Guise O. L., Ahner J. W., Jung M. C., Goughnour P. C., and Yates J. T. (2002) Reproducible electrochemical etching of tungsten probe tips. *Nano Letters* **2** [No. 3] 191–193.
- Gupta S., Zhang Q. L., Emrick T., Balazs A. C., and Russell T. P. (2006) Entropy-driven segregation of nanoparticles to cracks in multilayered composite polymer structures. *Nature Materials* **5** 229–233.
- Haacke G. (1976) New figure of merit for transparent conductors. *Journal of Applied Physics* **47** 4086.
- Hafner J. H., Cheung C. L., and Lieber C. M. (1999) Direct growth of single-walled carbon nanotube scanning probe microscopy tips. *J. Am. Chem. Soc* **121** [No. 41] 9750–9751.

- Han J. H., Paulus G. L. C., Maruyama R., Heller D. A., Kim W. J., Barone P. W., Lee C. Y., Choi J. H., Ham M. H., Song C., Fantini C., and Strano M. S. (2010) Exciton antennas and concentrators from core-shell and corrugated carbon nanotube filaments of homogeneous composition. *Nature Materials* **9** [No. 10] 833–839.
- Haroz E. H., Rice W. D., Lu B. Y., Ghosh S., Hauge R. H., Weisman R. B., Doorn S. K., and Kono J. (2010) Enrichment of armchair carbon nanotubes via density gradient ultracentrifugation: Raman spectroscopy evidence. *ACS Nano* **4** [No. 4] 1955–1962.
- Harutyunyan A. R., Chen G. G., Paronyan T. M., Pigos E. M., Kuznetsov O. A., Hewaparakrama K., Kim S. M., Zakharov D., Stach E. A., and Sumanasekera G. U. (2009) Preferential growth of single-walled carbon nanotubes with metallic conductivity. *Science* **326** [No. 5949] 116–120.
- Haven T., Armitage D., and Saupe A. (1981) Bend and splay elastic-constants and the rotational viscosity of nematic decylammonium chloride and ammonium-chloride water mixtures. *Journal of Chemical Physics* **75** [No. 1] 352–364.
- Hecht D., Hu L., and Gruner G. (2006) Conductivity scaling with bundle length and diameter in single-walled carbon nanotube networks. *Applied Physics Letters* **89** 133112.

- Henrich F., Krupke R., Kappes M. M., and Lohneysen H. V. (2005) Frequency dependence of the dielectrophoretic separation of single-walled carbon nanotubes. *Journal of Nanoscience and Nanotechnology* **5** [No. 7] 1166–1171.
- Hersam M. (2008) Progress Towards Monodisperse Single-Walled Carbon Nanotubes. *Nature Nanotechnology* **3** [No. 7] 387–394.
- Hobbie E. K. and Fry D. J. (2007) Rheology of concentrated carbon nanotube suspensions. *Journal of Chemical Physics* **126** 124907.
- Hu L., Hecht D. S., and Gruner G. (2004) Percolation in transparent and conducting carbon nanotube networks. *Nano Letters* **4** [No. 12] 25132517.
- Hu L. B., Hecht D. S., and Gruner G. (2010) Carbon nanotube thin films: Fabrication, properties, and applications. *Chemical Reviews* **110** [No. 10] 5790–5844.  
Times Cited: 1.
- Huang X. H., El-Sayed I. H., Qian W., and El-Sayed M. A. (2006) Cancer cell imaging and photothermal therapy in the near-infrared region by using gold nanorods. *Journal of the American Chemical Society* **128** [No. 6] 2115–2120.
- Huang X. H., El-Sayed I. H., Qian W., and El-Sayed M. A. (2007) Cancer cells assemble and align gold nanorods conjugated to antibodies to produce highly en-



- hanced, sharp, and polarized surface raman spectra: A potential cancer diagnostic marker. *Nano Letters* **7** 1591–1597.
- Huang Y., Duan X. F., Wei Q. Q., and Lieber C. M. (2001) Directed assembly of one-dimensional nanostructures into functional networks. *Science* **291** [No. 5504] 630–633.
- Hulman M. and Tajmar M. (2007) The dielectrophoretic attachment of nanotube fibres on tungsten needles. *Nanotechnology* **18** [No. 14] 5.
- Hummers W. S. and Offeman R. E. (1958) Preparation of graphite oxide. *Journal of the American Chemical Society* **80** [No. 6] 1339–1339. Times Cited: 741.
- Islam M. F., Rojas E., Bergey D. M., Johnson A. T., and Yodh A. G. (2003) High weight fraction surfactant solubilization of single-wall carbon nanotubes in water. *Nano Letters* **3** [No. 2] 269–273.
- Jana N. R., Gearheart L. A., Obare S. O., Johnson C. J., Edler K. J., Mann S., and Murphy C. J. (2002) Liquid crystalline assemblies of ordered gold nanorods. *Journal of Materials Chemistry* **12** [No. 10] 2909–2912.
- Kaempgen M., Duesberg G. S., and Roth S. (2005) Transparent carbon nanotube coatings. *Applied Surface Science* **252** [No. 2] 425–429.

- Keunings R. and Bousfield D. (1987) Analysis of surface-tension driven leveling in viscoelastic films. *Journal of Non-Newtonian Fluid Mechanics*.
- Kim K., Bae J., Park H., Kim S., Geng H., Park K., Shin H., Yoon S., Benayad A., Choi J., and others . (2008) Fermi Level Engineering of Single-Walled Carbon Nanotubes by AuCl<sub>3</sub> Doping. *Journal of the American Chemical Society* **130** [No. 38] 12757–12761.
- Kistler S. F. and Schweizer P. M. *Liquid Film Coating: Scientific Principles and Their Technological Implications*. Chapman & Hall (1997).
- Kong J., Cassell A. M., and Dai H. J. (1998) Chemical vapor deposition of methane for single-walled carbon nanotubes. *Chemical Physics Letters* **292** [No. 4-6] 567–574.
- Konishi H., Murata Y., Wongwiriyan W., Kishida M., Tomita K., Motoyoshi K., Honda S., Katayama M., Yoshimoto S., Kubo K., Hobara R., Matsuda I., Hasegawa S., Yoshimura M., Lee J. G., and Mori H. (2007) High-yield synthesis of conductive carbon nanotube tips for multiprobe scanning tunneling microscope. *Review of Scientific Instruments* **78** [No. 1] 6.
- Koziol K., Vilatela J., Moisala A., Motta M., Cunniff P., Sennett M., and Windle

- A. (2007) High-performance carbon nanotube fiber. *Science* **318** [No. 5858] 1892–1895.
- Krupke R., Hennrich F., Lohneysen H., and Kappes M. (2003) Separation of Metallic from Semiconducting Single-Walled Carbon Nanotubes. *Science* **301** [No. 5631] 344–347.
- Krupke R., Hennrich F., Kappes M. M., and Lohneysen H. V. (2004) Surface conductance induced dielectrophoresis of semiconducting single-walled carbon nanotubes. *Nano Letters* **4** [No. 8] 1395–1399.
- Lapointe C., Hultgren A., Silevitch D. M., Felton E. J., Reich D. H., and Leheny R. L. (2004) Elastic torque and the levitation of metal wires by a nematic liquid crystal. *Science* **303** [No. 5658] 652–655.
- Lapointe C. P., Mason T. G., and Smalyukh I. (2009) Shape-controlled colloidal interactions in nematic liquid crystals. *Science* **326** [No. 5956] 1083–1086.
- Lavrentovich O., Lazo I., and Pishnyak O. (2010) Nonlinear electrophoresis of dielectric and metal spheres in a nematic liquid crystal. *Nature* **467** [No. 7318] 947–950.
- Lee H. W., Kim S. H., Kwak Y. K., Lee E. S., and Han C. S. (2005) The effect of

- the shape of a tip's apex on the fabrication of an afm tip with an attached single carbon nanotube. *Sensors and Actuators a-Physical* **125** [No. 1] 41–49.
- Lewandowski E. P., Bernate J. A., Searson P. C., and Stebe K. J. (2008) Rotation and alignment of anisotropic particles on nonplanar interfaces. *Langmuir* **24** [No. 17] 9302–9307.
- Li Y. L., Kinloch I. A., and Windle A. H. (2004) Direct spinning of carbon nanotube fibers from chemical vapor deposition synthesis. *Science* **304** [No. 5668] 276–278.
- Liang W. J., Bockrath M., Bozovic D., Hafner J. H., Tinkham M., and Park H. (2001) Fabry-perot interference in a nanotube electron waveguide. *Nature* **411** [No. 6838] 665–669.
- Lide D. CRC Handbook of Chemistry and Physics, (Internet Version 2009) (2009).
- Lin Z., Cai J. J., Scriven L. E., and Davis H. T. (1994) Spherical-to-wormlike micelle transition in ctab solutions. *Journal of Physical Chemistry* **98** [No. 23] 5984–5993.
- Link S., Mohamed M. B., and El-Sayed M. A. (1999) Simulation of the optical absorption spectra of gold nanorods as a function of their aspect ratio and the effect of the medium dielectric constant. *Journal of Physical Chemistry B* **103** [No. 16] 3073–3077.

- Liu Q. K., Cui Y. X., Gardner D., Li X., He S. L., and Smalyukh I. (2010) Self-alignment of plasmonic gold nanorods in reconfigurable anisotropic fluids for tunable bulk metamaterial applications. *Nano Letters* **10** [No. 4] 1347–1353.
- Liu S. H., Tok J. B. H., Locklin J., and Bao Z. N. (2006) Assembly and alignment of metallic nanorods on surfaces with patterned wettability. *Small* **2** [No. 12] 1448–1453.
- Liu T. and Kumar S. (2003) Effect of orientation on the modulus of swnt films and fibers. *Nano Letters* **3** 647–650.
- Lopez F., Samseth J., Mortensen K., Rosenqvist E., and Rouch J. (1996) Micro- and macrostructural studies of sodium deoxycholate micellar complexes in aqueous solutions. *Langmuir* **12** [No. 26] 6188–6196.
- Lutz T. and Donovan K. J. (2005) Macroscopic scale separation of metallic and semiconducting nanotubes by dielectrophoresis. *Carbon* **43** [No. 12] 2508–2513.
- Ma J., Tang J., Zhang H., Shinya N., and Qin L. C. (2009) Ultrathin carbon nanotube fibrils of high electrochemical capacitance. *ACS Nano* **3** [No. 11] 3679–3683.
- Ma W., Song L., Yang R., Zhang T., Zhao Y., Sun L., Ren Y., Liu D., Liu L., and Shen J. (2007) Directly synthesized strong, highly conducting, transparent single-walled carbon nanotube films. *Nano Letters* **7** [No. 8] 2307–2311.

- Maeda A., Matsumoto S., Kishida H., Takenobu T., Iwasa Y., Shiraishi M., Ata M., and Okamoto H. (2005) Large optical nonlinearity of semiconducting single-walled carbon nanotubes under resonant excitations. *Physical Review Letters* **94** [No. 4] 47404.
- Mankowic A. (1965) Dimensional analysis applied to detergency. *Journal of American Oil Chemical Society* **42** [No. 7] 629–633.
- Marcano D. C., Kosynkin D. V., Berlin J. M., Sinitskii A., Sun Z. Z., Slesarev A., Alemany L. B., Lu W., and Tour J. M. (2010) Improved synthesis of graphene oxide. *ACS Nano* **4** [No. 8] 4806–4814.
- Mayer C. W. (1911) Coating-machine. *US Patent number: 1043021*.
- Meitl M. A., Zhou Y. X., Gaur A., Jeon S., Usrey M. L., Strano M. S., and Rogers J. A. (2004) Solution casting and transfer printing single-walled carbon nanotube films. *Nano Letters* **4** [No. 9] 1643–1649.
- Mendes M. J., Schmidt H. K., and Pasquali M. (2008) Brownian dynamics simulations of single-wall carbon nanotube separation by type using dielectrophoresis. *Journal of Physical Chemistry B* **112** [No. 25] 7467–7477.
- Messer B., Song J. H., and Yang P. D. (2000) Microchannel networks for nanowire patterning. *Journal of the American Chemical Society* **122** [No. 41] 10232–10233.

- Mintmire J. and White C. (1998) Universal Density of States for Carbon Nanotubes. *Physical Review Letters* **81** [No. 12] 2506–2509.
- Moore V. C., Strano M. S., Haroz E. H., Hauge R. H., Smalley R. E., Schmidt J., and Talmon Y. (2003) Individually suspended single-walled carbon nanotubes in various surfactants. *Nano Letters* **3** [No. 10] 1379–1382.
- Morfa A. J., Rowlen K. L., Reilly T. H., Romero M. J., and van de Lagemaat J. (2008) Plasmon-enhanced solar energy conversion in organic bulk heterojunction photovoltaics. *Applied Physics Letters* **92** [No. 1].
- Moulton S. E., Maugey M., Poulin P., and Wallace G. G. (2007) Liquid crystal behavior of single-walled carbon nanotubes dispersed in biological hyaluronic acid solutions. *Journal of the American Chemical Society* **129** [No. 30] 9452–9457.
- Mourad M. C. D., Devid E. J., van Schooneveld M. M., Vonk C., and Lekkerkerker H. N. W. (2008) Formation of nematic liquid crystals of sterically stabilized layered double hydroxide platelets. *Journal of Physical Chemistry B* **112** [No. 33] 10142–10152.
- Mourchid A., Delville A., Lambard J., Lecolier E., and Levitz P. (1995) Phase-diagram of colloidal dispersions of anisotropic charged-particles - equilibrium prop-

- erties, structure, and rheology of laponite suspensions. *Langmuir* **11** [No. 6] 1942–1950.
- Mourchid A., Lecolier E., Van Damme H., and Levitz P. (1998) On viscoelastic, birefringent, and swelling properties of laponite clay suspensions: Revisited phase diagram. *Langmuir* **14** [No. 17] 4718–4723.
- Murphy C. J., San T. K., Gole A. M., Orendorff C. J., Gao J. X., Gou L., Hunyadi S. E., and Li T. (2005) Anisotropic metal nanoparticles: Synthesis, assembly, and optical applications. *Journal of Physical Chemistry B* **109** [No. 29] 13857–13870.
- Murphy C. L. and Orendorff C. J. (2005) Alignment of gold nanorods in polymer composites and on polymer surfaces. *Advanced Materials* **17** [No. 18] 2173–2177.
- Nastishin Y. A., Liu H., Schneider T., Nazarenko V., Vasyuta R., Shiyanovskii S. V., and Lavrentovich O. D. (2005) Optical characterization of the nematic lyotropic chromonic liquid crystals: Light absorption, birefringence, and scalar order parameter. *Physical Review E* **72** [No. 4] 041711.
- Nikoobakht B. and El-Sayed M. A. (2003) Surface-enhanced raman scattering studies on aggregated gold nanorods. *Journal of Physical Chemistry A* **107** [No. 18] 3372–3378.



- Nikoobakht B., Wang Z. L., and El-Sayed M. A. (2000) Self-assembly of gold nanorods. *Journal of Physical Chemistry B* **104** [No. 36] 8635–8640.
- O’Connell M. J., Boul P., Ericson L. M., Huffman C., Wang Y., Haroz E., Kuper C., Tour J., Ausman K. D., and Smalley R. E. (2001) Reversible water-solubilization of single-walled carbon nanotubes by polymer wrapping. *Chemical Physics Letters* **342** [No. 3-4] 265–271.
- O’Connell M. J., Bachilo S. M., Huffman C. B., Moore V. C., Strano M. S., Haroz E. H., Rialon K. L., Boul P. J., Noon W. H., Kittrell C., Ma J. P., Hauge R. H., Weisman R. B., and Smalley R. E. (2002) Band gap fluorescence from individual single-walled carbon nanotubes. *Science* **297** [No. 5581] 593–596.
- Odom T. W., Huang J. L., Kim P., and Lieber C. M. (1998) Atomic structure and electronic properties of single-walled carbon nanotubes. *Nature* **391** [No. 6662] 62–64.
- Onsager L. (1949) The Effects of Shape on the Interaction of Colloidal Particles. *Annals of the New York Academy of Sciences* **51** [No. Molecular Interaction] 627–659.
- Orendorff C. J., Gearheart L., Jana N. R., and Murphy C. J. (2006) Aspect ratio

- dependence on surface enhanced raman scattering using silver and gold nanorod substrates. *Physical Chemistry Chemical Physics* **8** [No. 1] 165–170.
- Osipov M. A. and Hess S. (1993) The elastic-constants of nematic and nematic discotic liquid-crystals with perfect local orientational order. *Molecular Physics* **78** [No. 5] 1191–1201.
- Parekh B. B., Fanchini G., Eda G., and Chhowalla M. (2007) Improved conductivity of transparent single-wall carbon nanotube thin films via stable postdeposition functionalization. *Applied Physics Letters* **90** [No. 12] 121913.
- Park J. K., Kim J. E., and Han C. S. (2005) Use of dielectrophoresis in a high-yield fabrication of a carbon nanotube tip. *Japanese Journal of Applied Physics Part 1- Regular Papers Brief Communications and Review Papers* **44** [No. 5A] 3235–3239.
- Park K. A., Lee S. M., Lee S. H., and Lee Y. H. (2007) Anchoring a liquid crystal molecule on a single-walled carbon nanotube. *Journal of Physical Chemistry C* **111** 1620–1624.
- Parra-Vasquez A., Behabtu N., Green M., Pint C., Young C., Schmidt J., Kesselman E., Goyal A., Ajayan P., Cohen Y., Talmon Y., Hauge R., and Pasquali M. (2010) Spontaneous Dissolution of Ultralong Single-and Multiwalled Carbon Nanotubes. *ACS Nano* pages 145–249.

- Parra-Vasquez A. N. G., Stepanek I., Davis V. A., Moore V. C., Haroz E. H., Shaver J., Hauge R. H., Smalley R. E., and Pasquali M. (2007) Simple length determination of single-walled carbon nanotubes by viscosity measurements in dilute suspensions. *Macromolecules* **40** [No. 11] 4043–4047.
- Pasquali M. and Scriven L. E. (2002) Free surface flows of polymer solutions with models based on the conformation tensor. *Journal of Non-Newtonian Fluid Mechanics* **108** [No. 1-3] 363–409.
- Peigney A., Laurent C., Flahaut E., Bacsa R. R., and Rousset A. (2001) Specific surface area of carbon nanotubes and bundles of carbon nanotubes. *Carbon* **39** [No. 4] 507–514.
- Perova T. S. and Vij J. K. (1995) The influence of surface-structure on the discotic liquid-crystalline alignment - an infrared-spectroscopy study. *Advanced Materials* **7** [No. 11] 919–922.
- Petit C. A. P. and Carbeck J. D. (2003) Combing of molecules in microchannels (commic): A method for micropatterning and orienting stretched molecules of dna on a surface. *Nano Letters* **3** [No. 8] 1141–1146.
- Phuong N. H., Germano G., and Schmid F. (2001) Elastic constants from direct cor-

- relation functions in nematic liquid crystals: A computer simulation study. *Journal of Chemical Physics* **115** [No. 15] 7227–7234.
- Pint C. L., Xu Y. Q., Pasquali M., and Hauge R. H. (2008) Formation of highly dense aligned ribbons and transparent films of single-walled carbon nanotubes directly from carpets. *ACS Nano* **2** [No. 9] 1871–1878.
- Pint C. L., Xu Y. Q., Morosan E., and Hauge R. H. (2009) Alignment dependence of one-dimensional electronic hopping transport observed in films of highly aligned, ultralong single-walled carbon nanotubes. *Applied Physics Letters* **94** [No. 18].
- Pint C. L., Xu Y. Q., Moghazy S., Cherukuri T., Alvarez N. T., Haroz E. H., Mahzooni S., Doorn S. K., Kono J., Pasquali M., and Hauge R. H. (2010) Dry contact transfer printing of aligned carbon nanotube patterns and characterization of their optical properties for diameter distribution and alignment. *ACS Nano* **4** [No. 2] 1131–1145.
- Planeix J. M., Coustel N., Coq B., Brotons V., Kumbhar P. S., Dutartre R., Geneste P., Bernier P., and Ajayan P. M. (1994) Application of carbon nanotubes as supports in heterogenous catalysis. *Journal of the American Chemical Society* **116** [No. 17] 7935–7936.

- Poulin P. and Weitz D. (1998) Inverted and multiple nematic emulsions. *Physical Review E* **57** [No. 1] 626–637.
- Poulin P., Frances N., and Mondain-Monval O. (1999) Suspension of spherical particles in nematic solutions of disks and rods. *Physical Review E* **59** [No. 4] 4384–4387.
- Raghavan S. R., Fritz G., and Kaler E. W. (2002) Wormlike micelles formed by synergistic self-assembly in mixtures of anionic and cationic surfactants. *Langmuir* **18** [No. 10] 3797–3803.
- Rai P. K., Parra-Vasquez A. N. G., Chattopadhyay J., Pinnick R. A., Liang F., Sadana A. K., Hauge R. H., Billups W. E., and Pasquali M. (2007) Dispersions of functionalized single-walled carbon nanotubes in strong acids: Solubility and rheology. *Journal of Nanoscience and Nanotechnology* **7** [No. 10] 3378–3385.
- Redon C., Brochard-Wyart F., and Rondelez F. (1991) Dynamics of dewetting. *Physical Review Letters* **66** [No. 6] 715–718.
- Rowley L. A., Irvin G. C., Anderson C. C., and D. M. (2006a) Coating compositions containing single-wall carbon nanotubes. *US Patent Application Number: 20060188723*.
- Rowley L. A., Spath T. M., and Irvin G. C. (2006b) Roll to roll high transparency,

- high conductivity swcnt films used in flexible electronics. *Abstract American Chemical Society* **232** [No. 130-PRES].
- Ruhwandl R. W. and Terentjev E. M. (1997a) Long-range forces and aggregation of colloid particles in a nematic liquid crystal. *Physical Review E* **55** [No. 3] 2958–2961.
- Ruhwandl R. W. and Terentjev E. M. (1997b) Monte carlo simulation of topological defects in the nematic liquid crystal matrix around a spherical colloid particle. *Physical Review E* **56** [No. 5] 5561–5565.
- Russell J. M., Oh S. J., LaRue I., Zhou O., and Samulski E. T. (2006) Alignment of nematic liquid crystals using carbon nanotube films. *Thin Solid Films* **509** [No. 1-2] 53–57.
- Saito R., Fujita M., Dresselhaus G., and Dresselhaus M. (2009) Electronic Structure of Chiral Graphene Tubules. *Applied Physics Letters* **60** [No. 18] 2204–2206.
- Salalha W. and Zussman E. (2005) Investigation of fluidic assembly of nanowires using a droplet inside microchannels. *Physics of Fluids* **17** [No. 6].
- Serp P., Corrias M., and Kalck P. (2003) Carbon nanotubes and nanofibers in catalysis. *Applied Catalysis A: General* **253** [No. 2] 337–358.

- Shaffer M. S. P., Fan X., and Windle A. H. (1998) Dispersion and packing of carbon nanotubes. *Carbon* **36** [No. 11] 1603–1612.
- Shalaev V. M. (2007) Optical negative-index metamaterials. *Nature Photonics* **1** [No. 1] 41–48.
- Shalaev V. M., Cai W. S., Chettiar U. K., Yuan H. K., Sarychev A. K., Drachev V. P., and Kildishev A. V. (2005) Negative index of refraction in optical metamaterials. *Optics Letters* **30** [No. 24] 3356–3358.
- Sharma R., Lee C. Y., Choi J. H., Chen K., and Strano M. S. (2007) Nanometer positioning, parallel alignment, and placement of single anisotropic nanoparticles using hydrodynamic forces in cylindrical droplets. *Nano Letters* **7** [No. 9] 2693–2700.
- Shenhar R., Norsten T. B., and Rotello V. M. (2005) Polymer-mediated nanoparticle assembly: Structural control and applications. *Advanced Materials* **17** [No. 6] 657–669.
- Shimoda H., Oh S. J., Geng H. Z., Walker R. J., Zhang X. B., McNeil L. E., and Zhou O. (2002) Self-assembly of carbon nanotubes. *Advanced Materials* **14** [No. 12] 899–901.

- Sihvola A. (2000) Mixing rules with complex dielectric coefficients. *Subsurface Sensing Technologies and Applications* **1** [No. 4] 393–415.
- Smalyukh I., Kachynski A. V., Kuzmin A. N., and Prasad P. N. (2006) Laser trapping in anisotropic fluids and polarization-controlled particle dynamics. *Proceedings of the National Academy of Sciences of the United States of America* **103** [No. 48] 18048–18053.
- Song W. H., Kinloch I. A., and Windle A. H. (2003) Nematic liquid crystallinity of multiwall carbon nanotubes. *Science* **302** [No. 5649] 1363–1363.
- Sonin A. S. (1998) Inorganic lyotropic liquid crystals. *Journal of Materials Chemistry* **8** [No. 12] 2557–2574.
- Spath T. M., Irvin G. C. J., Majumdar D., Cok R. S., and Anderson C. C. (2006) Touchscreen with conductive layer comprising carbon nanotubes. *US Patent Application Number: 20060274048*.
- Spotnitz M. E., Ryan D., and Stone H. A. (2004) Dip coating for the alignment of carbon nanotubes on curved surfaces. *Journal of Materials Chemistry* **14** [No. 8] 1299–1302.
- Sreekumar T. V., Liu T., Kumar S., Ericson L. M., Hauge R. H., and Smalley R. E.



- (2003) Single-wall carbon nanotube films. *Chemistry of Materials* **15** [No. 1] 175–178.
- Subacius D., Pergamenschchik V. M., and Lavrentovich O. D. (1995) Measurement of polar anchoring coefficient for nematic cell with high pretilt angle. *Applied Physics Letters* **67** [No. 2] 214–216.
- Sun Z., Nicolosi V., Rickard D., Bergin S. D., Aherne D., and Coleman J. N. (2008) Quantitative evaluation of surfactant-stabilized single-walled carbon nanotubes: dispersion quality and its correlation with zeta potential. *The Journal of Physical Chemistry C* **112** [No. 29] 10692–10699.
- Tang J., Gao B., Geng H. Z., Velev O. D., Qin L. C., and Zhou O. (2003) Assembly of id nanostructures into sub-micrometer diameter fibrils with controlled and variable length by dielectrophoresis. *Advanced Materials* **15** [No. 16] 1352–1355.
- Tang J., Yang G., Zhang Q., Parhat A., Maynor B., Liu J., Qin L. C., and Zhou O. (2005) Rapid and reproducible fabrication of carbon nanotube afm probes by dielectrophoresis. *Nano Letters* **5** [No. 1] 11–14.
- Tans S. J., Devoret M. H., Dai H. J., Thess A., Smalley R. E., Geerligs L. J., and Dekker C. (1997) Individual single-wall carbon nanotubes as quantum wires. *Nature* **386** [No. 6624] 474–477.

- Tatsuura S., Furuki M., Sato Y., Iwasa I., Tian M., and Mitsu H. (2003) Semiconductor carbon nanotubes as ultrafast switching materials for optical telecommunications. *Advanced Materials* **15** [No. 6] 534.
- Thess A., Lee R., Nikolaev P., Dai H. J., Petit P., Robert J., Xu C. H., Lee Y. H., Kim S. G., Rinzler A. G., Colbert D. T., Scuseria G. E., Tomanek D., Fischer J. E., and Smalley R. E. (1996) Crystalline ropes of metallic carbon nanotubes. *Science* **273** [No. 5274] 483–487.
- Tjiptomargo B., Evans G. T., Allen M. P., and Frenkel D. (1992) Elastic-constants of hard and soft nematic liquid-crystals. *Journal of Physical Chemistry* **96** [No. 10] 3942–3948.
- van der Beek D. and Lekkerkerker H. N. W. (2003) Nematic ordering vs. gelation in suspensions of charged platelets. *Europhysics Letters* **61** [No. 5] 702–707.
- van der Beek D., Davidson P., Wensink H. H., Vroege G. J., and Lekkerkerker H. N. W. (2008) Influence of a magnetic field on the nematic phase of hard colloidal platelets. *Physical Review E* **77** [No. 3] 031708–031716.
- van der Kooij F. M. and Lekkerkerker H. N. W. (1998) Formation of nematic liquid crystals in suspensions of hard colloidal platelets. *Journal of Physical Chemistry B* **102** [No. 40] 7829–7832.

- van der Kooij F. M., Kassapidou K., and Lekkerkerker H. N. W. (2000) Liquid crystal phase transitions in suspensions of polydisperse plate-like particles. *Nature* **406** [No. 6798] 868–871.
- van der Schoot P., Popa-Nita V., and Kralj S. (2008) Alignment of carbon nanotubes in nematic liquid crystals. *Journal of Physical Chemistry B* **112** [No. 15] 4512–4518.
- van der Zande B. M. I., Koper G. J. M., and Lekkerkerker H. N. W. (1999) Alignment of rod-shaped gold particles by electric fields. *Journal of Physical Chemistry B* **103** [No. 28] 5754–5760.
- Vavro J., Llaguno M. C., Fischer J. E., Ramesh S., Saini R. K., Ericson L. M., Davis V. A., Hauge R. H., Pasquali M., and Smalley R. E. (2003) Thermoelectric power of p-doped single-wall carbon nanotubes and the role of phonon drag. *Physical Review Letters* **90** [No. 6] 65503.
- Vigolo B., Penicaud A., Coulon C., Sauder C., Pailler R., Journet C., Bernier P., and Poulin P. (2000) Macroscopic fibers and ribbons of oriented carbon nanotubes. *Science* **290** [No. 5495] 1331–1334.
- Vigolo B., Coulon C., Maugey M., Zakri C., and Poulin P. (2005) An experimental approach to the percolation of sticky nanotubes. *Science* **309** [No. 5736] 920–923.

- Vroege G. J. and Lekkerkerker H. N. W. (1992) Phase-transitions in lyotropic colloidal and polymer liquid-crystals. *Reports on Progress in Physics* **55** [No. 8] 1241–1309.
- Wahlstrom E. *Optical crystallography*. John Wiley & Sons Inc. 5th edition (1979).
- Wang H., Zhou W., Ho D. L., Winey K. I., Fischer J. E., Glinka C. J., and Hobbie E. K. (2004) Dispersing single-walled carbon nanotubes with surfactants: A small angle neutron scattering study. *Nano Letters* **4** [No. 9] 1789–1793.
- Wang Y., Ericson L. M., Kittrell C., Kim M. J., Shan H., Fan H., Ripley S., Ramesh S., Hauge R. H., Adams W. W., Pasquali M., and Smalley R. E. (2005) Revealing the substructure of single-walled carbon nanotube fibers. *Chemistry of Materials* **17** [No. 25] 6361–6368.
- Wei H. Y., Craig A., Huey B. D., Papadimitrakopoulos F., and Marcus H. L. (2008a) Electric field and tip geometry effects on dielectrophoretic growth of carbon nanotube nanofibrils on scanning probes. *Nanotechnology* **19** [No. 45] 8.
- Wei H. Y., Kim S. N., Zhao M. H., Ju S. Y., Huey B. D., Marcus H. L., and Papadimitrakopoulos F. (2008b) Control of length and spatial functionality of single-wall carbon nanotube afm nanoprobe. *Chemistry of Materials* **20** [No. 8] 2793–2801.

- Wensink H. H. and Vroege G. J. (2003) Isotropic-nematic phase behavior of length-polydisperse hard rods. *Journal of Chemical Physics* **119** [No. 13] 6868–6882.
- Westphalen M., Kreibig U., Rostalski J., Luth H., and Meissner D. (2000) Metal cluster enhanced organic solar cells. *Solar Energy Materials and Solar Cells* **61** [No. 1] 97–105.
- Wong S. S., Woolley A. T., Odom T. W., Huang J. L., Kim P., Vezenov D. V., and Lieber C. M. (1998) Single-walled carbon nanotube probes for high-resolution nanostructure imaging. *Applied Physics Letters* **73** 3465.
- Wu Z., Chen Z., Du X., Logan J. M., Sippel J., Nikolou M., Kamaras K., Reynolds J. R., Tanner D. B., Hebard A. F., and Rinzler A. (2004) Transparent, conductive carbon nanotube films. *Science* **305** [No. 5688] 1273–1276.
- Xu Y. Q., Flor E., Kim M. J., Hamadani B., Schmidt H., Smalley R. E., and Hauge R. H. (2006) Vertical array growth of small diameter single-walled carbon nanotubes. *Journal of the American Chemical Society* **128** [No. 20] 6560–6561.
- Yakobson B. I. and Avouris P. *Mechanical Properties of Carbon Nanotubes* volume 80 of *Topics in Applied Physics*. Springer-Verlag Berlin Berlin (2001).
- Yeh P. and Gu C. *Optics of Liquid Crystal Displays*. John Wiley & Sons, Inc. 1st edition (1999).

- Yodh A. G., Lin K. H., Crocker J. C., Dinsmore A. D., Verma R., and Kaplan P. D. (2001) Entropically driven self-assembly and interaction in suspension. *Philosophical Transactions of the Royal Society of London Series a-Mathematical Physical and Engineering Sciences* **359** [No. 1789] 2629–2629.
- Yu M. F., Dyer M. J., Skidmore G. D., Rohrs H. W., Lu X. K., Ausman K. D., Von Ehr J. R., and Ruoff R. S. (1999) Three-dimensional manipulation of carbon nanotubes under a scanning electron microscope. *Nanotechnology* **10** 244–252.
- Yu X., Rajamani R., Stelson K. A., and Cui T. (2006) Carbon nanotube based transparent conductive thin films. *Journal of Nanoscience & Nanotechnology* **6** [No. 7] 1939–1944.
- Yu X., Rajamani R., Stelson K. A., and Cui T. (2008) Fabrication of carbon nanotube based transparent conductive thin films using layer-by-layer technology. *Surface and Coatings Technology* **202** [No. 10] 2002–2007.
- Zhang M., Fang S. L., Zakhidov A. A., Lee S. B., Aliev A. E., Williams C. D., Atkinson K. R., and Baughman R. H. (2005) Strong, transparent, multifunctional, carbon nanotube sheets. *Science* **309** [No. 5738] 1215–1219.
- Zhao J., Han J., and Lu J. (2002) Work Functions of Pristine and Alkali-Metal

- Intercalated Carbon Nanotubes and Bundles. *Physical Review B* **65** [No. 19] 193401.
- Zhou W., Islam M. F., Wang H., Ho D. L., Yodh A. G., Winey K. I., and Fischer J. E. (2004a) Small angle neutron scattering from single-wall carbon nanotube suspensions: evidence for isolated rigid rods and rod networks. *Chemical Physics Letters* **384** [No. 1-3] 185–189.
- Zhou W., Vavro J., Guthy C., Winey K. I., Fischer J. E., Ericson L. M., Ramesh S., Saini R., Davis V. A., Kittrell C., Pasquali M., Hauge R. H., and Smalley R. E. (2004b) Single-wall carbon nanotube fibers extruded from super-acid suspensions: Preferred orientation, electrical, and thermal transport. *Journal Applied Physics* **95** [No. 2] 649–655.
- Zhou W., Fischer J. E., Heiney P. A., Fan H., Davis V. A., Pasquali M., and Smalley R. E. (2005) Single-walled carbon nanotubes in superacid: X-ray and calorimetric evidence for partly ordered H<sub>2</sub>SO<sub>4</sub>. *Physical Reviews B* **72** [No. 4] 45440.
- Zhou Y., Hu L., and Gruner G. (2006) A method of printing carbon nanotube thin films. *Applied Physics Letters* **88** 123109.
- Zocher H. (1925) On independent structure formation in brine. *Zeitschrift Fur Anorganische Und Allgemeine Chemie* **147** [No. 1/3] 91–U15.